UNIVERSITÄT PADERBORN

Quantenchemische Rechnungen und Synthesen stickstoffreicher Kohlenstoffnitride

Dissertation

Zur Erlangung des akademischen Grades
Doktor der Naturwissenschaften (Dr. rer. nat)
dem Department Chemie der Fakultät für Naturwissenschaften

vorgelegt von

Karlo Julius Robert Nolkemper

am 25. August 2025

1. Gutachter: Prof. Dr. Thomas D. Kühne
2. Gutachter: Jun. Prof. Dr. Lopez Salas

Eidesstattliche Erklärung

Hiermit versichere ich, dass ich die vorliegende Arbeit selbstständig verfasst und keine anderen als die angegebenen Quellen und Hilfsmittel benutzt habe. Alle Ausführungen, die fremden Quellen wörtlich oder sinngemäß entnommen wurden, sind kenntlich gemacht. Die Arbeit war in gleicher oder ähnlicher Form noch nicht Bestandteil einer Studien- oder Prüfungsleistung.

Paderborn, den 25. August 2025 Karlo Nolkemper

Nutzung von Künstlicher Intelligenz

In dieser wissenschaftlichen Arbeit wurden Künstliche Intelligenz (KI)-Technologien zur Unterstützung verschiedener Aspekte der Forschung eingesetzt. Diese wurde zur Übersetzung, Vokabelfindung, Satz- und Fehlerkorrektur verwendet. Es wird ausdrücklich darauf hingewiesen, dass die endgültige Verantwortung für die inhaltliche Richtigkeit, die kritische Reflexion und die Interpretation der Ergebnisse beim Autor dieser Arbeit liegt.

Danksagung

Zuerst einmal gilt mein besonderer Dank Thomas Kühne, für die Möglichkeit, in den letzten vier Jahren in seinem Arbeitskreis zu forschen, und die Geduld und Hilfe, die mir dabei zuteil geworden ist. Ich habe an vielen interessanten Themen arbeiten können, eine Menge dazugelernt und viele interessante Leute kennengelernt. Dabei herrschte immer eine entspannte Arbeitsatmosphäre, und es gab den passenden Freiraum, um eigene Forschungsschwerpunkte setzen zu können.
Als Weiteres möchte ich mich bei Nieves Lopez Salas bedanken, deren Arbeitskreis mich quasi adoptiert hat, als mein alter AK sich an der Uni PB aufgelöst hat, und deren Labor ich benutzen konnte. Auch von ihr habe ich eine Menge gelernt.
Mein Dank gilt auch Markus Antonietti, dessen beeindruckendes Wissen und mitreißende Art, über Chemie zu reden, mich stets fasziniert.
Hossam Elgabarty danke ich für all die interessanten Gespräche, die Unterstützung und Sporteinheiten unterschiedlichster Art.
Britta Fremerey und allen (ehemaligen) Mitgliedern des AK Kühne, des AK Lopez Salas und auch des AK Brehm, mit denen ich bei all den Mensabesuchen, Kaffeepausen und nicht zuletzt auch bei der Arbeit viel Spaß haben konnte. Unterhaltsame Kollegen, mit denen man sich gut versteht, machen den Arbeitsalltag ungemein angenehmer.
Zu guter Letzt gilt mein Dank auch meiner Familie und meinen Freunden, für die Unterstützung, Urlaube und all den Spaß abseits der Uni, sowie dafür, dass ich in der ganzen Zeit keine wirklichen Sorgen haben brauchte.

Acronyms and Abbreviations

DFT Density Functional Theory, Dichtefunctionaltheorie

DDEC Density-derived Electrostatic and Chemical method

NAC Net Atomic Charge

DFTB Density Functional Tight Binding

NICS Nucleus Independant Chemical Shift

PHI Poly(Heptazine Imides)

ABT Azo-Bridged Triazine

CN Carbon Nitride

Zusammenfassung

Diese Dissertation befasst sich mit theoretischen und experimentellen Untersuchungen zu Kohlenstoffnitriden, einer umfangreichen und vielseitigen Materialklasse basierend auf den beiden Elementen Kohlenstoff und Stickstoff. Aufgrund ihrer katalytischen Eigenschaften, vergleichsweise einfachen Synthesewegen und des Verzichts auf seltene oder toxische Metalle gelten sie als vielversprechend für nachhaltige Anwendungen wie Photokatalyse, Energiespeicherung, Gasadsorption und CO_2-Reduktion.

Fokus dieser Arbeit bilden Materialien mit extrem hohem Stickstoffanteil, insbesondere CN_2. Durch eine systematische, mehrstufige Strukturuche wurden unter Verwendung quantenchemischer Methoden mehrere thermodynamisch stabile polymorphe CN_2-Strukturen identifiziert und hinsichtlich ihrer elektronischen Eigenschaften und thermischen Stabilität analysiert. Dabei ließen sich einige Strukturen aufzeigen, welche sowohl dynamisch als auch kinetisch stabil sowie vielversprechende elektronische Eigenschaften für, zum Beispiel, photokatalytische Anwendungen mitbringen. Eine dieser Strukturen wurde anschließend erfolgreich synthetisiert und mithilfe verschiedenster analytischer Methoden charakterisiert und analysiert. Dabei konnten zwei Synthesewege mit unterschiedlichen Vor- und Nachteilen etabliert werden. Das synthetisierte azo-verbrückte Triazol (ABT) zeigt photokatalytische Aktivität, bietet eine elektrochemische Kapazität, und besitzt zudem das Potential durch gezielte strukturelle Modifikation die katalytische Aktivität zu steigern.

In den folgenden theoretischen Teilprojekten wurden spezifische Fragestellungen zu CN-Materialien in Kooperation mit experimentellen Arbeitsgruppen untersucht. Darunter ist zum einen das Adsorptionsverhalten von H^+ und NH_4^+ in Na- und H-poly(heptazinimide) (PHI) Systemen, welches, wie gezeigt werden konnte, durch lichtinduzierte Aufladung maßgeblich beeinflusst wird. Des Weiteren wurde der Einfluss von terminalen Gruppen auf die Elektronenstruktur und Adsorptionsenergie in donor-akzeptor-ähnlichen PHI-Systemen, im Hinblick auf die Adsorptionsenergie von O_2 und letztlich die photokatalytische Aktivität zur H_2O_2 Produktion untersucht. Außerdem wurde das Benetzungsverhalten sowie die spezifische Interaktion mit Wasser von C_1N_1 (Sub)Nanoporen modelliert und analysiert. In allen Fällen konnte die theoretische Modellierung experimentelle Befunde bestätigen, differenzieren und durch mechanistische Einblicke wesentlich erweitern. Die Ergebnisse dieser Arbeit tragen dazu bei, das Struktur-Eigenschafts-Verhältnis stickstoffreicher Kohlenstoffnitride besser zu verstehen und liefern neue Impulse für deren gezielte Weiterentwicklung und Anwendung.

Abstract

This dissertation deals with theoretical and experimental investigations of carbon nitrides, a broad and versatile class of materials based on carbon and nitrogen. Due to their catalytic properties, comparatively simple synthesis routes, and the avoidance of rare or toxic metals, they are considered promising for sustainable applications such as photocatalysis, energy storage, gas adsorption, and CO_2 reduction.
The focus of this work is on materials with an extremely high nitrogen content, particularly CN_2. Through a systematic, multi-step structure search using quantum chemical methods, several thermodynamically stable polymorphic CN_2 structures were identified and analyzed with regard to their electronic properties and thermal stability. Some of these structures were found to be both dynamically and kinetically stable and to exhibit promising electronic properties, for example, for photocatalytic applications. One of these structures was subsequently synthesized and characterized using various analytical methods. Two synthesis routes with different advantages and disadvantages were established. The synthesized azo-bridged triazole (ABT) shows photocatalytic activity and provides electrochemical capacity, and also possesses the potential to enhance its catalytic activity through targeted structural modifications.
In the following theoretical subprojects, specific research questions regarding CN materials were investigated in collaboration with experimental research groups. These include the adsorption behavior of H^+ and NH_4^+ in Na- and H-PHI systems, which, as shown, is significantly influenced by photocharging. Furthermore, the influence of terminal groups on the electronic structure and adsorption energy in donor-acceptor-like PHI systems was studied, specifically with regard to the adsorption energy of O_2 and ultimately the photocatalytic activity for H_2O_2 production. In addition, the wettability and specific interaction of water of C_1N_1 (sub)nanopores was studied. In all cases, theoretical modeling was able to confirm, differentiate, and substantially deepen experimental findings through mechanistic insights. The results of this work contribute to a better understanding of the structure–property relationships of nitrogen-rich carbon nitrides and provide new impulses for their targeted development and application.

Contents

1. Introduction

The research presented in this thesis highlights the various facets and application possibilities of carbon nitrides, a class of materials defined, just as the name suggests, by carbon and nitrogen. It is an emerging class of materials with a wide variety of appearances which have proved to be remarkable in terms of catalytic applications. But its roots go back a long way. As early as 1834, Justus Liebig discovered what he describes as exhibiting a weak ammonia smell, which strongly irritates the eyes when heated with dry chloric gas and with a bitter almond-like taste [1]. He named this finding "melon", and later it was shown to be an early carbon nitride. Surely, those were different times of research, and I can assure that for this thesis, no chemicals have been analyzed via the sense of taste, which would have been troublesome when conducting mostly computational studies anyway.
Despite the early discovery, their time was only to come with the new millennium, after Cohen predicted that a carbon nitride material would have a higher compression resistance than diamond [2], and later with Liu suggesting C_3N_4 for further research [3]. This C_3N_4, being closely related to Liebig's melon, led to increased exploration of carbon nitridic materials, their properties, possible structures, and use cases, and culminates in the discovery of their photocatalytic capabilities and potential to facilitate the water splitting reaction to produce oxygen and hydrogen [4]. It is shown in Figure 1.1 below, together with two other intensely studied carbon nitrides. The material's bandgap of 2.7 eV is well suited for water splitting reactions, but there are disadvantages as well. It suffers from quick charge-hole recombination, poor usage of the natural solar irradiation spectra, lowering the overall quantum efficiency, and a low surface area. Templating approaches or exfoliating techniques have been developed to enlarge the surface area to overcome these issues [5]. Alternatively, altering the structure or stoichiometry to tune the bandgap and expand the lifetimes of the excited states is an option. This expanded the knowledge

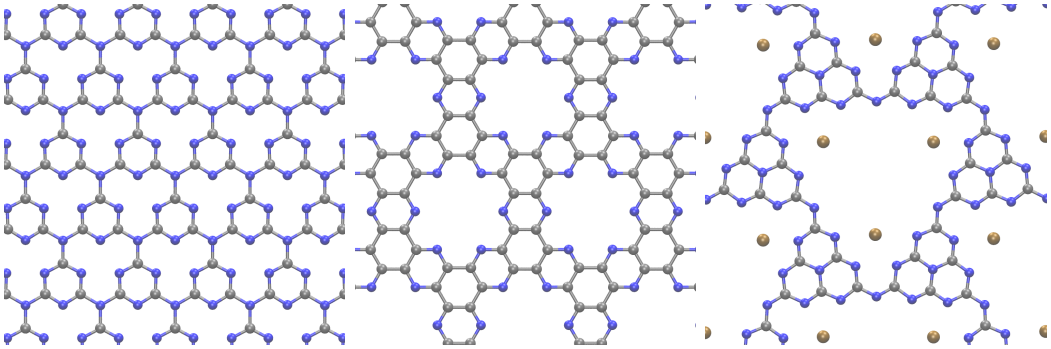

Figure 1.1.: (from left to right) s-triazine (a g-C_3N_4), two dimensional C_2N and Na-PHI for comparison. Gray spheres depicts carbon, blue ones nitrogen, and ochre colored sodium.

and broadness of known carbon nitrides, and stoichiometries such as C_2N [6], C_1N_1 [7], other C_3N_4 materials like metal doped poly(heptazine imide) [8], C_3N_5 [9, 10] or CN_2 [11, 12] have garnered interest and been investigated experimentally and computationally.

Figure 1.1 depicts three representative two-dimensional carbon nitride materials which are thoroughly investigated. While g-C_3N_4 consists of triazine units linked in a layered structure, often used as a benchmark photocatalyst, its performance is limited by poor conductivity and rapid charge-hole recombination. Closely related is tri-s-triazine, which is also a g-C_3N_4 material, but built from heptazine units, which are also the main building block for PHI materials. C_2N exhibits a highly ordered pore network with abundant nitrogen atoms, increasing its basicity and adsorption capacity. Its higher electronic conductivity and defined pores make it promising for gas capture and catalysis [13, 14]. Na-PHI, in contrast, is built from heptazine units and incorporates sodium ions into its framework, and shows enhanced crystallinity, hydrophilicity, and ion exchange properties. These structural differences lead to distinct electronic and surface properties, allowing fine-tuning of band gaps, charge carrier lifetimes, and catalytic activity [15].

With further attention and research being conducted, many interesting applications and properties have arisen, and they cover areas such as metal-free catalysis [16], physisorption for selective gas purification [14], CO_2 activation and reduction [17], energy storage [5], and photocatalytic usage for different purposes, such as photodegradation of organic pollutants, catalysing organic reactions, water-splitting or

hydrogen(peroxide) production [4, 18, 19].

In general, carbon nitride materials are promising for several reasons. First, their catalytic activity is not based on toxic or rare earth metals, which are typically scarce and expensive, but both elements are earth-abundant and inexpensive. Secondly, they are highly active throughout many possible applications, as already described above, and highly functionalizable with respect to specific use cases. Finally, synthesis can be straightforward and easily upscaled, although this is not always the case.

Although very promising materials have been developed, still existing disadvantages keep the need for further optimization and innovation high, and with this work, I plan to expand the scope of usable carbon nitrides and deepen the understanding of those. Specifically, this thesis reaches the realm of CN_2. Stable materials with this high nitrogen content have only gained minor attention, although the high proportion of nitrogen offers superior surface basicity in the form of electron donor ability, also suggesting a high hydrophilicity [20]. Multiple theoretical papers highlight the electronic properties of this material and its applicability as sensing material, to capture toxic gases [21], for degradation of waste [22] or as photocatalyst [23], making it a highly promising material for further research.

The thesis is organized as follows. The next chapter will give a brief introduction to the necessary and underlying theoretical concepts, which are useful for grasping the rest of the work. This includes the fundamentals of quantum chemistry, density functional theory and charge partitioning schemes to assign net atomic charges to atoms within molecules or solids.

Thereafter, a structure search for thermodynamically and kinetically stable CN_2 crystal structures is presented. The work has been published in The Journal of Physics C together with M. Antonietti, T.D. Kühne and S. A. Ghasemi. It explores potential stable structures via a high-throughput search and several sieving steps with increasing accuracy. This yielded thermodynamically low-lying structures, which were further refined via molecular dynamic simulations and finally examined regarding their electronic properties. The resulting structures presented are very promising candidates for different applications in the fields of carbon capture, photocatalysis, or energy storage.

Following this work, triazines connected via azo-groups, presented in chapter one,

are studied in more detail regarding adsorption properties, charge distribution, and are synthesized. Analytic measurements covering a broad range of methods were applied to validate the synthesis and structure of the products. Two synthetic routes could be verified, including a solution-based reaction in the beaker and a solid-state reaction in the oven with elevated temperatures assisted by molten salts. This work is currently in preparation to be submitted and published.

The next three chapters deal with different phenomena related to carbon nitrides, with a strong focus on computational studies of the published papers.

In the first case, the behavior of proton and ammonium adsorbed on two different PHI materials was investigated and compared. We explain the experimental observations made and observe mechanistic differences caused by the charges of sodium ions within Na-PHI compared to H-PHI.

Second, the influence of terminating groups on further advanced PHI, which shares potassium and sodium ions, labeled KNa-PHI, is studied. Amine and triazole units are used to model the terminating groups of a flake of PHI units. The donor-acceptor nature of the latter alters the electronic structure and increases the adsorption energy released when interacting with O_2. This rate determining step in the H_2O_2 production from O_2 and H_2O is thus accelerated and the overall yield of the reaction increased.

In the third project, the wettability of nitrogen doped carbon electrodes is studied, as it has a significant influence on their capability in aqueous media. An amorphous C_1N_1 model, which contains a wide variety of structural motifs and aromatic systems, was created. Water adsorption properties as well as their shifts within nucleo-magnetic resonance spectra are examined and alongside the experimental studies used to explain the unintuitive adsorption characteristics.

The final chapter provides the conclusions of this thesis.

2. Theoretical Framework

This chapter provides an introduction to the underlying theoretical concepts employed in this thesis, which are essential for understanding the rest of the work. It mainly explains the fundamentals of quantum chemistry and DFT. Insights into charge partitioning schemes, which were used broadly in this thesis, are described as well. This chapter is loosely based on the fantastic introduction by Klaus Capelles to DFT [24], but also found inspiration in other works [25, 26, 27].

2.1. Schrödinger equation

Before starting with DFT, an introduction to the fundamentals of quantum mechanical systems, such as the Schrödinger equation and the Born-Oppenheimer concept [28, 29] is useful.

To describe non-relativistic, chemical systems, the wavefunction Ψ offers a complete description of a given system, including all information that are potentially accessible, according to the Copenhagen interpretation of quantum mechanics. It is the ultimate goal to solve the wavefunction, by using Schrödingers equation, which in its time-independent, non-relativistic form reads as

$$\hat{H}(r)\Psi(r) = E\Psi(r). \tag{2.1}$$

E resembling the energy of a given system, and $\hat{H}$ denotes the Hamiltonian operator. The Hamilton operator can be divided into five terms, describing the kinetic and potential energies of the nuclei and electrons.

$$\hat{H} = \hat{T}_e + \hat{T}_N + \hat{V}_{Ne} + \hat{V}_{ee} + \hat{V}_{NN} \tag{2.2}$$

Beginning with the kinetic energy of the electrons $\hat{T}_e$ and the nuclei $\hat{T}_N$, followed by the Coulomb interaction between the electron-nuclei $\hat{V}_{Ne}$, the electron-electron $\hat{V}_{ee}$ and the nuclei-nuclei $\hat{V}_{NN}$, respectively.

The kinetic energy operators describe the sum of each particle's motion in all spatial directions, as expressed with the Laplacian ∇_i^2, $\hbar$ denotes reduced Planck's constant and m the mass of the particle.

$$\hat{T} = -\sum_i \frac{\hbar^2}{2m_i}\nabla_i^2 \tag{2.3}$$

The potential energy operator sums over all pairwise interactions between charges, whether repulsive or attractive, in relation to their distance. The equation below illustrates this for all nuclei k with charge Q_k and position R_k, and electrons i with charge q and position r_i.

$$\hat{V}_{Ne} = \sum_{ik} \frac{Q_k q}{|r_i - R_k|} \tag{2.4}$$

With k and l denoting the M_N nuclei of the system, while i and j run over the electrons N_{el}, the whole Hamiltonian can now be expressed as

$$\hat{H} = -\frac{\hbar^2}{2m_e}\sum_{i=1}^{N_{el}}\nabla_i^2 - \frac{\hbar^2}{2}\sum_{k=1}^{M_N}\frac{\nabla_k^2}{m_k} - \sum_{i=1}^{N_{el}}\sum_{k=1}^{M_N}\frac{Q_k q_i}{r_{ik}} + \sum_{i<j}^{N_{el}}\frac{q_i q_j}{r_{ij}} + \sum_{k<l}^{M_N}\frac{Q_k Q_l}{R_{kl}}. \tag{2.5}$$

In Planck units q, m_i and $\hbar$ are equal to one and can be omitted. However, this equation can be even further simplified by taking the mass of nuclei and electrons into account. In a carbon-12 atom, for example, the mass of the nuclei exceeds that of an electron by 20 000 times. Due to inertia, its movement therefore is much slower, which is why we can consider the nuclei static, and the electrons moving in a fixed field. This is called the Born-Oppenheimer approximation. With this approximation, the kinetic energy of the nuclei becomes zero and their potential energy a constant, we can condense the Hamiltonian operator to the so-called electronic Hamiltonian

$$\hat{H}_{el} = \hat{T}_e + \hat{V}_{Ne} + \hat{V}_{ee}. \tag{2.6}$$

In order to calculate the total energy E_{tot} of the system one has to sum over the resulting E_{el} and the constant of the nuclear repulsion energy E_N.

$$E_{tot} = E_{el} + E_N \tag{2.7}$$

$\hat{V}_{Ne}$ shown in 2.4 is, in contrast to the other terms of $\hat{H}_{el}$ non-universal, as it depends on the specific system that is studied. Its expectation value $\nu(r)$ is therefore labeled as the external potential and plays an important role. In order to calculate the

observables, the system is specified via $\nu(r)$, which enters the Schrödinger equation. Solving this equation yields the many-body wavefunction Ψ.

$$\nu(r) \rightarrow H_{el} \xrightarrow{SE} \Psi(r_1, r_2, ..., r_N) \xrightarrow{\langle\Psi|\hat{O}|\Psi\rangle} \langle O\rangle \tag{2.8}$$

While Ψ itself is not an observable, its square

$$|\Psi(\overrightarrow{x}_1, \overrightarrow{x}_2, ..., \overrightarrow{x}_N)|^2 d\overrightarrow{x}_1 d\overrightarrow{x}_2 ... d\overrightarrow{x}_N \tag{2.9}$$

represents the probability that electrons 1 to N are found in the spatial elements $d\overrightarrow{x}_1 d\overrightarrow{x}_2 ... d\overrightarrow{x}_N$ at the same time. For any normalized wavefunction, the integral over all points of the probability equals one.

To calculate any observable, expectation values of the corresponding operators are evaluated with this wave function. The electron density $\rho(r)$ can be expressed as the local expectation value of the density operator,

$$\rho(r) = N \int d^3r_2 \int d^3r_3 ... \int d^3r_N \Psi^*(r, r_2, ..., r_N)\Psi(r, r_2, ..., r_N), \tag{2.10}$$

with Ψ^* as the complex conjugate. Unlike an expectation value, $\rho(r)$ is a function of position, obtained by integrating over the coordinates of all electrons except one. The electron density plays a central role in DFT and will be the subject of the next chapter.

2.2. Density functional theory

DFT is a broadly used computational method to approach ab initio calculations with. Relying on the electron density rather than the wavefunction significantly reduces the computational complexity and enables the practical use of quantum chemical calculations for molecules. This is due to the dependency of the wavefunction on 3N variables, while $\rho(r)$ for large systems only depends on 3 spatial variables, dramatically decreasing the degree of complexity. The way and why we can use the electron density instead of the wavefunctions is introduced below.

2.2.1. Hohenberg-Kohn theorem

The foundation of DFT lies in the two Hohenberg-Kohn theorems, originally formulated and proven by Hohenberg and Kohn in 1964 [30], but later reformulated by

Levy and Lieb [31, 32]. The proofs and derivations of the equations described below can be found there. The first Hohenberg-Kohn theorem states that the external potential $\nu(r)$ is a unique functional of the electron density $\rho(r)$, except for a trivial constant. This, in turn, determines the ground-state wavefunction as a unique functional of the ground-state density.

$$\Psi_0(r_1, r_2, ..., r_N) = \Psi[(\rho_0(r)] \tag{2.11}$$

Modifying Equation 2.8 we can express

$$\rho(r) \rightarrow \nu(r) \rightarrow H_{el} \xrightarrow{SE} \Psi(r_1, r_2, ..., r_N) \rightarrow \rho(r). \tag{2.12}$$

Consequently, the ground-state expectation value for any observable $\hat{O}$ is then also a functional of the ground-state electron density $\rho_0(r)$

$$O_0 = O[\rho_0] = \langle \Psi[\rho_0] | \hat{O} | \Psi[\rho_0] \rangle . \tag{2.13}$$

The second Hohenberg-Kohn theorem is analogous to the variational principle for wavefunctions, since the functional only yields the minimum energy if $\rho_0(r)$ is the exact ground-state density

$$E_\nu[\rho_0(r)] \leq E_\nu[\rho'(r)], \tag{2.14}$$

with $\rho'(r)$ being any density. Therefore, when using a trial wave function to obtain an expectation value, one will never obtain an energy lower than the ground-state energy (again, Ψ' describes any wavefunction that is not the ground-state wavefunction Ψ_0; E_ν describing the energy in the external potential $\nu(r)$):

$$E_{\nu,0} = E_\nu[\Psi_0] = \langle \Psi_0 | \hat{H} | \Psi_0 \rangle \leq \langle \Psi' | \hat{H} | \Psi' \rangle = E_\nu[\Psi'] \tag{2.15}$$

Ultimately, calculating the ground-state energy becomes a minimization problem. Practically, we don't know how to do this. First, minimization of $E_\nu[\rho]$ is not a straightforward problem to solve, and, in addition, the expectation values for $\hat{T}_e$: $T[\rho]$, and for $\hat{V}_{ee}$: $U[\rho]$, need to be approximated, as they are unknown.

2.2.2. Kohn-Sham approach

The most common practical approach to solve DFT was implemented by Kohn and Sham based on their paper from 1965 [33]. The main idea is to separate the

terms that are known from those that are unknown and to subsume all of them into a correction term called E_{XC}. This approach is formally correct up to the point where E_{XC} is approximated. The kinetic energy can be exactly calculated for non-interacting electrons, but not for a fully interacting many-body system, and therefore is simplified by dividing it into a non-interacting part, $T_s[\rho]$, and a correction term $T_c[\rho]$ that accounts for the missing information.

$$T_c[\rho] = T[\rho] - T_s[\rho] \tag{2.16}$$

The electron-electron interactions are the second term that can be simplified, by treating them as classical Coulomb repulsion, and labeling them as the Hartree energy U_H. However, real electrons are not classical particles, they obey the Pauli principle and are correlated in space and spin. Moreover, this Hartree term includes a self-interaction error, as each electron mistakenly interacts with its own electron density, captured in ρ. Therefore, a correction term is needed to account for exchange, correlation, and self-interaction cancellation.

$$U_c[\rho] = U[\rho] - U_H[\rho] \tag{2.17}$$

Equation 2.6 can now be reformulated as

$$E[\rho] = T[\rho] + U[\rho] + V[\rho] = T_s[\rho] + U_H[\rho] + V[\rho] + E_{XC}[\rho] \tag{2.18}$$

with E_{XC} including the correction terms mentioned above. In this manner, the largest part of the energy is now exactly calculated, and only the relatively small correction term has to be approximated.

To make the problem computationally accessible, an auxiliary system of non-interacting electrons is introduced. This system is constructed such that it reproduces a density $\rho_s(r)$ that is exactly equal to the ground-state electron density $\rho(r)$ of the fully interacting many-body system. The corresponding single-particle states are called Kohn–Sham orbitals, denoted by $\phi_i(r)$.

$$\rho(r) \equiv \rho_s(r) = \sum_{i=1}^{N} f_i |\phi_i(r)|^2 \tag{2.19}$$

f_i denotes the occupation number of orbital i, ranging from 0 (empty) to 2 (fully occupied). The effective Kohn-Sham potential $\nu_s(r)$ consists of $\nu(r)$, the external

potential, the Hartree potential $\nu_H(r)$ and $\nu_{xc}(r)$, the exchange-correlation potential derived from E_{xc} with respect to the density.

$$\nu_s(r) = \nu(r) + \nu_H(r) + \nu_{xc}(r), \tag{2.20}$$

This potential is used to solve the Schrödinger equation of the auxiliary system, which then yields the Kohn-Sham orbitals.

$$\left[\frac{-\hbar^2\nabla^2}{2m} + \nu_s(r)\right]\phi_i(r) = \epsilon_i\phi_i(r) \tag{2.21}$$

The non-interacting kinetic energy can then be expressed as:

$$T_s[\rho] = -\frac{\hbar^2}{2m}\sum_i^N \int d^3r\phi_i^*(r)\nabla^2\phi_i(r) \tag{2.22}$$

As a result, the ground-state density $\rho(r)$ of the interacting many-body system can ultimately be obtained by solving a non-interacting single-particle problem. Starting with an initial guess for $\rho(r)$, the $\nu_s(r)$ is calculated and used to solve Eq. 2.21. The retrieved ϕ_i is then fed to Eq. 2.19 and a new density is obtained. This process is repeated until it converges, and is referred to as the self-consistency cycle.

2.2.3. Approximations to E_{xc}

A variety of approximations have been developed to evaluate the exchange-correlation energy E_{xc}, with increasing accuracy generally accompanied by higher computational effort. These functionals are commonly categorized based on their accuracy and computational cost into local density approximation (LDA), generalized gradient approximation (GGA), meta-GGA, and hybrid functionals. In the LDA, the exchange–correlation energy density at each point r is approximated by that of a uniform electron gas with density equal to the local density $\rho(r)$. This approach has proven to be accurate for metals but generally inadequate for molecules due to their strongly inhomogeneous electron densities.

$$E_{xc}[\rho] \approx E_{xc}^{LDA}[\rho] = \int d^3r e_{xc}^{hom}(\rho(r)) \tag{2.23}$$

LDA functionals typically underestimate the correlation energy while overestimating the exchange energy, resulting in a partial cancellation of errors [24]. However, chemical systems such as molecules are spatially inhomogeneous because their electron

density varies significantly across space in molecular systems. A more accurate and general approach to the exchange-correlation energy is given by GGA functionals, as shown in Equation 2.24, which include a gradient correction.

$$E_{xc}^{GGA}[\rho] = \int d^3r f(\rho(r), \nabla\rho(r)) \tag{2.24}$$

Although GGA functionals capture covalent bonds much better than LDA, they still fail to describe weak van der Waals interactions, and chemical accuracy is not yet achieved. Representative examples are PBE [34] or BLYP [35, 36], although there are also functionals with long-range dispersion correction, which cover these shortcomings. A typical example, used throughout this thesis, is B97-3c [37].
Even higher precision can be obtained from meta-GGA functionals. Like GGAs, meta-GGA functionals incorporate gradient corrections, but also depend on the Kohn–Sham kinetic energy density $\tau(r)$, providing an additional descriptor to better capture subtle variations in electron localization.

$$E_{xc}^{meta-GGA}[\rho] = \int d^3r f(\rho(r), \nabla\rho(r), \tau(r)) \tag{2.25}$$

This additional degree of freedom can be used to further improve the accuracy of the results. A common example is the SCAN functional [38]. Further improvements can be achieved by hybrid-GGA functionals, which combine GGA exchange with a fraction of exact exchange from Hartree–Fock theory, to improve the treatment of systems with strong self-interaction errors and better capture the delocalization behavior of electrons. Double-hybrid functionals extend this concept by additionally including an explicit perturbative correlation term, typically from second-order Møller–Plesset theory. This term captures long-range dynamic correlation and dispersion effects that semilocal functionals cannot describe, thereby further improving accuracy. Double-hybrid functionals represent the highest rung on Jacob's ladder of DFT, a metaphor for the climb toward chemical accuracy.

2.3. Charge Partitioning for net atomic charges

Throughout this thesis, net atomic charges will be used to summarize information and display it in an easily accessible way, while being intuitively accessible and well transferable to experimental concepts. There are a plethora of different approaches used to partition the electron density and assign charges to atoms, and here, I want to display three ways of doing so. In general, the NAC (q_i) is equal to the nuclear charge of an atom (z_i), which is determined by the number of electrons an atom normally possesses, subtracted by the number of electrons assigned to the atom (N_i)

$$q_i = Z_i - N_i \tag{2.26}$$

Crucial is, however, how these electrons are assigned to an atom. Before looking at more advanced methods, a short look at two fundamental methods is appropriate: the Mulliken and Hirshfeld population analysis. Both are used to represent different approaches to assigning the electrons to the nuclei: Mulliken as representative of those methods based on basis sets; and Hirshfeld for those separating the electron density based on real space [39].

2.3.1. Mulliken population analysis

Mulliken's idea, published in 1955 [40], is based on the linear combination of atomic orbitals (LCAO). The molecular orbital is constructed from the LCAO as

$$\psi_i = \sum_{r_k} c_{ir_k} \phi_{ir_k}. \tag{2.27}$$

With ψ denoting the molecular orbital i, multiplied by a coefficient c gained from the calculations, it is summed over the basis functions ϕ, which are constructed from the basis set and used to represent the atomic orbitals. Subsequently, the electrons are distributed into

$$N(i) = N(i) \sum_{r_k} ci_{r_k}^2 + 2N(i) \sum_{l>k} ci_{r_k} ci_{s_l} S_{r_k s_l} \tag{2.28}$$

the *net atomic population*, characterized by the first term in 2.28, and the *overlap population*, equaling the second term, as they were labeled by Mulliken [40]. The *gross atomic population* or formal charges [41] is then calculated according to the

following Equation 2.29, by summing over all the orbitals assigned to a nuclei, and equally dividing the overlap population between the atoms.

$$N(i;r_k) = N(i)c_{ir_k}(c_{ir_k} + \sum_{l \neq k} c_{is_l} S_{r_k s_l}) \tag{2.29}$$

Now, the net atomic charge can be calculated as described in Equation 2.26. From today's perspective, this method is a comparatively simple and a fast approach, requiring only few computational resources, but it has severe drawbacks. First and foremost, there is the dependency on the basis sets to construct the molecular orbitals, which are used to decide which electrons are assigned to which nucleus. Depending on which basis set is used, and there are a plethora of them, the resulting NACs can also vary for identical molecules. Secondly, splitting the electrons of the overlap population 50/50 does not reflect the different attraction of the electron to certain nuclei, and can lead to unphysical, negative values of the gross atomic population [40]. There are more modern approaches designed to overcome these issues, such as performing a symmetric orthogonalization on basis sets, as presented by Löwdin [42], or the natural population analysis [43], which uses localized orbitals and generally yields good results in accordance with the chemical intuition, but is troublesome to be applied to periodic systems [44, 45].

2.3.2. Hirshfeld population analysis

Hirshfeld population analysis uses a "stockholder model", named after a metaphor Hirshfeld uses in his paper [46], where the actual electrons assigned to each atom in a molecule are based on the share the promolecular atoms have on each point of space. In his publication [46] he starts by introducing this promolecular density, which is the sum of ground-state atomic densities ρ_i^{at}

$$\rho^{pro}(r) = \sum_i \rho_i^{at}(r) \tag{2.30}$$

and then constructs sharing functions $w_i(r)$, which determine the amount of electron density an atom contributes to the promolecular density at any point of space r.

$$w_i(r) = \frac{\rho_i^{at}(r)}{\rho^{pro}(r)} \tag{2.31}$$

Because of Equation 2.30, the sum of all sharing functions equals one. This weighting function can now be used to assign the electron density to the bonded atoms

$\rho^{bonded-at}$, by multiplying it with the molecular density, which can be retrieved through DFT calculations.

$$\rho_i^{bonded-at}(r) = w_i(r)\rho^{mol}(r) \tag{2.32}$$

Principally, this is enough, as one can now integrate over $\rho^{bonded-at}$

$$N_i = \int \rho_i^{bonded-at}(r)dr \tag{2.33}$$

to calculate the assigned charge and compute the NAC via Equation 2.26. Practically, a more indirect way via calculating the atomic deformation density is taken, to avoid integration issues [46]. Although this approach is independent of the basis set used, it generally underestimates charges, especially for ionic compounds [47, 48, 49]. Newer approaches, such as iterative Hirshfeld, improve this but have other issues, like the bifurcation problem [45, 48].

2.3.3. Density-derived electrostatic and chemical method

In the following, I will give an introduction to the newest DDEC6 approach, published by Manz and Limas, which overcomes the previous problems and is more chemically intuitive and robust by combining electron localization with weighted reference ions and spherical averaging [45]. Its key element is the careful iterative adjustment of the weighting factor $w_i(\vec{r})$, which is used to calculate the integrated atomic electron density to retrieve charges, as shown in Equation 2.32 and 2.33. For this, a total of seven steps are applied and will be presented below.

1) Calculating reference ion charges q_A^{ref} from neutral atom reference densities using stockholder partitioning mixed with localized charge partitioning.

$$q_i^{ref} = (1-\lambda)q_i^{stock} + \lambda q_i^{loc} \tag{2.34}$$

With $\lambda = \frac{2}{3}$ being the phenomenological optimum. This is to avoid issues arising from solely using localized atomic charges, which do not model the electrostatic potential very well but, for example, well reproduce charge transfer trends, and stockholder atomic charges, which do not reproduce localized information about the atomic charges. Unlike in the Mulliken approach, however, the localized approach

here is real-space defined, avoiding any basis set dependency. A detailed summation and evaluation of this method can be found in chapter 3.2 of [45].

2)The second step reiterates the reference ion charges by using q_i^{ref} from step one as an input value and refining it.

3) In this step, the reference ion density is conditioned so that it is closer to that of the material under investigation. Additionally, there are two constraints introduced to ensure that the specific electron density of an atom decreases monotonically with increasing distance, and to ensure that the integration over the electrons of the reference ion yields the correct value. Then, the conditioned density is calculated as shown below.

$$\rho_r^{cond}(r_i) = Y_i^{avg}(r_i) + \sqrt{Y_i^{avg}(r_i)} \left(\Phi_i + \frac{d\Gamma_i(r_i)}{dr_i} + \frac{2\Gamma_i(r_i)}{r_i} \right) \tag{2.35}$$

With Γ_i and Φ_i being Lagrange multipliers and used to enforce the constraints mentioned. Y^{avg} is a scaling factor to modify the reference density and better match it with the calculated values.

$$Y_i^{avg}(r_i) = \rho_i^{ref} \left\langle \frac{\rho(\vec{r})}{\rho^{ref.}(\vec{r})} \right\rangle_{r_i} \tag{2.36}$$

With $\rho^{ref}(\vec{r}) = \sum_i \rho_i^{ref}(r_i, q_i^{ref.})$ and $\langle\rangle_{r_i}$ is used to describe spherical averaging. Finally, $\rho^{cond}(\vec{r})$ is obtained by summing over all $\rho_i^{cond}(r_i)$.

$$\rho^{cond}(\vec{r}) = \sum_i \rho_i^{cond}(r_i) \tag{2.37}$$

This new density is used for the additional calculation of some further values, then they are stored and used for the next steps. Additional details on this process and DDEC6 in general can be found in the literature [45].

4) Here, the foundations for the succeeding steps are prepared by building the initial weighted/ sharing function from the conditioned reference density calculated before.

$$w_i(r_i) = \rho_i^{cond}(r_i) \tag{2.38}$$

This is then used to compute the spherical average.

$$\rho_i^{avg}(r_i) = \left\langle \frac{w_i(r_i)\rho(\vec{r})}{W(\vec{r})} \right\rangle \tag{2.39}$$

$$W(\vec{r}) = \sum_i w_i(r_i) \tag{2.40}$$

Finally,the weighted spherical average $\rho_i^{w-avg}(r_i)$ is calculated.

$$\rho_i^{w-avg}(r_i) = \frac{\left\langle \left(1 - \frac{w_i(r_i)}{W(\vec{r})}\right) \rho_i(\vec{r_i}) \right\rangle_{r_i} + \frac{\rho_i^{avg}(r_i)}{5} \left\langle \frac{w_i(r_i)}{W(\vec{r})} \right\rangle_{r_i}}{1 - \frac{4}{5} \left\langle \frac{w_i(r_i)}{W(\vec{r})} \right\rangle_{r_i}} \tag{2.41}$$

5-7) In the following steps, the computations done for step 4 will be iteratively repeated to optimize the weighting factor and the reference density, and this is the core of this method. There are also additional constraints introduced, mainly to decrease the atomic tails, which describe the electron density assigned to a certain atom overlapping with the density assigned to another atom. After enough iterations to fulfill the ending conditions, with N_i,

$$N_i = \oint \rho_i(\vec{r}) d^3\vec{r_i} \tag{2.42}$$

the charges, based on Equation 2.26, are printed.

This rather complex procedure avoids many issues with the previously mentioned approaches to the NACs. It is applicable to a wide variety of systems with different elements and stoichiometries and delivers results that are comparable between atoms in different environments. Furthermore, they agree well with trends derived from electronegativity. The sole disadvantage is the relatively complex approach and the associated higher computational effort necessary [45]. However, all charge analyses presented in this thesis rely on this method, and therefore, its core functionalities should be mentioned here.

3. Kinetically stable and highly ordered two-dimensional CN_2 crystal structures

The present work focuses on the identification of stable structures with CN_2 stoichiometry. A systematic, multistep, and comprehensive structure search was performed, the workflow of which is visualized in the flowchart in Figure 3.1. This study is a joint publication together with M. Antonietti, T.D. Kühne, and S.A. Ghasemi, published in the Journal of Physical Chemistry C under the title *Kinetically stable and highly ordered two-dimensional CN_2 crystal structures* [50]. Starting from the extensive dataset of candidate structures obtained via initial DFTB calculations, my contribution primarily involved the refinement and analysis of these structures using successive steps of increasingly accurate DFT methods. I was able to identify thermodynamically low-energy structures, eliminate duplicates, and discard systems in which gaseous products, mainly N_2, had formed. In addition to structural filtering, the relevant properties of the remaining systems were calculated.

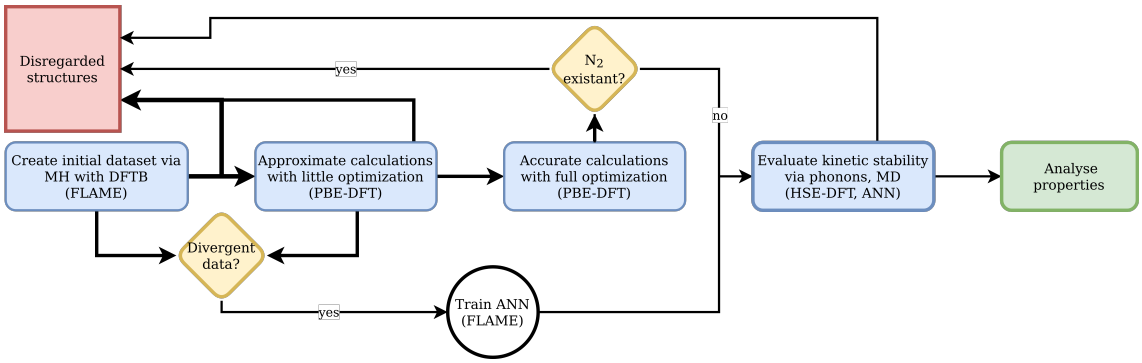

Figure 3.1.: Workflow of multiple-step sieving process, unfavorable structures are sorted out before proceeding with more accurate methods.

3.1. Introduction

To minimize the ecological impact of a continuously growing human population and to preserve a vivid planet, it is necessary to shift the bustling economies towards a more sustainable and less polluting direction of growth through the development of advanced technologies and materials. Researchers are acting to broaden the promising avenue of solar energy harnessing, whether via its direct conversion into electricity or the transformation and storage of it as chemical energy, e.g. by photocatalytic water splitting. Materials discovery for photocatalysis applications is at the center of attention as an essential element for the advancement of sustainable energy technologies. Carbon nitrides (CNs) have shown to be promising and cost-effective materials whose syntheses are straightforward and merely rely on inexpensive resources and precursors accessible throughout the planet. In 2009, Antonietti and coworkers synthesized a polymeric CN compound through the condensation of cyanamide and proposed its usability as a metal-free photocatalyst [51]. Since then, the search for catalytically efficient and industrially scalable CN composites has been a vibrant research stream within advanced materials discovery.

Highly-ordered stoichiometric CNs in graphitic form (g-C_3N_4) have been synthesized [52, 53, 54, 55]. Bulk g-C_3N_4 exhibits a high rate of photoinduced electron-hole recombination and insufficient specific surface area for industrial applications. Possible remedies include synthesizing stoichiometries other than C_3N_4, transforming bulk graphitic CN into other morphologies such as nanocomposites [56], and introducing adequate dopants [57]. In fact, the C/N ratio not only has an impact on structural features of CN, thereby affecting electronic properties and photocatalytic activity, but can be decisive in other developments, such as host-dopant interaction or formation of nanosheets or nanotubes.

CNs with other stoichiometries have also been synthesized, such as C_7N_1 [58], C_3N [59], C_2N [60], C_1N_1 [61], near-C_3N_5 [62, 63], C_3N_6 [20], and C_3N_7 [20]. The molecular structures and consequently physicochemical properties of the various synthesizable CNs depend on the choice of precursors and synthesis strategy. High nitrogen-content CNs are particularly interesting for photocatalysis applications due to the abundance of active sites for redox reactions. CNs are usually synthesized through the pyrolysis of precursors with high nitrogen content at high temperatures.

However, the condensation reaction of nitrogen-rich precursors at moderate temperatures is also realizable through external pressure treatments [64]. A very high nitrogen content of CN_4 composition has been obtained from high-pressure treatment of a single molecular precursor, namely cyanuric triazide; however, the crystalline samples recovered at ambient conditions had decomposed and ended up as amorphous compounds [65]. It may be difficult to stabilize crystalline CNs with such high nitrogen content at ambient conditions. However, techniques for pressure-induced polymerization at room temperature have been successfully applied in the synthesis of CN compositions with a lower nitrogen content [64] than that of Ref. [65] and resulted in stable compounds at ambient conditions after decompression. Nitrogen-rich CNs with stoichiometries close to C_3N_5 have been investigated both experimentally [62, 63, 66, 67, 68] and theoretically [69]. Significantly different values of band gap have been reported for C_3N_5 in both experimental and theoretical studies that could be due to differences in the structure or exact stoichiometry of the compounds. Even though the same precursor, namely 3-amino-1,2,4-triazole, was used in Refs. [62], [66], and [68], dissimilar electronic properties, such as band gaps, were reported due to the differing details of their preparation. To the best of our knowledge, C_3N_6 and C_3N_7 are the CNs with the largest value of nitrogen content synthesized thus far [20]. However, the synthesis of them through a mere pyrolysis strategy without templating has not been reported yet. These materials have shown to be highly stable after annealing for two hours at 250°C. When synthesizing nitrogen-rich CNs, the use of a suitable synthesis strategy and avoidance of very high temperatures are important for retaining a high content of nitrogen in the product, as illustrated in the supporting information of Ref. [20].

Accurately unveiling the chemical structures of polymeric CNs is challenging. In the case of C_3N_4, two major polymorphs consisting of s-triazine [70] and s-heptazine [51] units have been proposed based on the synthesis precursors and spectral signatures. Hydrogen atoms usually remain in CN samples, due to incomplete decomposition of the cyanamide or other precursors containing it. However, the content of residual hydrogen can be controlled by annealing and applying pressure [71]. Furthermore, hydrogen [72] or oxygen [73] can passivate pyridinic and pyrrolic nitrogens, and the impact of hydrogen content on the photocatalytic performance of CN compounds is not negligible. The thermodynamic stability of crystalline g-

C_3N_4 has been characterized at the level of density functional theory [74, 75]. The structural characteristics of CNs other than C_3N_4 have been investigated to a lesser extent. CN_2 has been investigated as a superhard material using theoretical methods. However, the polymorphs are only thermodynamically favorable under large hydrostatic pressures above 45 GPa [76]. A structure other than graphitic layers and with a large band gap, has been theoretically considered for this composition. It is called penta-CN_2 [77], and its structure imitates that of the Cairo tiling-like carbon allotrope penta-graphene [78]. Mortazavi and coworkers predicted a highly porous polymorph of CN_2 based on the triazine moiety and theoretically investigated its physicochemical properties [79]. Another CN_2 structure has recently been introduced that, likewise to penta-CN_2, may have interesting potential applications as a high-energy-density material [80]. Herein, we present three interesting polymorphs identified from a systematic theoretical study of thermodynamically stable structures of CN_2 by means of a crystal structure prediction method.

3.2. Computational Methods

3.2.1. Structure Search Procedure

In this study, we employed a variety of computational methods. The structure search was based on the minima hopping (MH) method [81, 82] as implemented in the FLAME code [83]. The MH method is comprised of successive short molecular dynamics (MD) trajectories, each followed by a local geometry optimization. CN polymorphs can be composed of various structural motifs due to the intricate nature of the chemical bonding among carbon and nitrogen atoms. Consequently, CNs typically have a very complex potential energy surface (PES). Hence, a large number of force calculations are required to perform a thorough structural search of CN PESs. It is thus essential to exploit an efficient method of obtaining total energies and forces on atoms, both in the short MD runs and in the local geometry optimizations. We employed the MH method coupled with the self-consistent-charge density functional tight-binding [84] (SCC-DFTB), as implemented in the DFTB+ package [85, 86]. The search consisted of MH runs of eight supercell sizes, ranging from five to twelve formula units. For each supercell size, we executed 1500 independent

MH runs with different starting points. To explore various parts of the potential energy surface efficiently and to attain a set of putatively low-lying energy structures, it is of great importance to start MH runs with diverse and distinct atomic arrangements. Initial configurations were generated by randomly removing atoms from a planar configuration of the graphite lattice to create voids and through substitution of carbon atoms with nitrogens to realize the target stoichiometry. In total, more than one million structures were visited within each MH run. However, not all are necessarily distinct. Dissimilarity checks, based on structural fingerprints [87], were considered only within each individual MH run, rather than across all runs. Nevertheless, it is expected that a large portion of the structures are distinct, since we initiated MH runs with a diversified set of structures that had passed dissimilarity checks. All structural searches were performed for bulk conformations with 3D periodic boundary conditions.

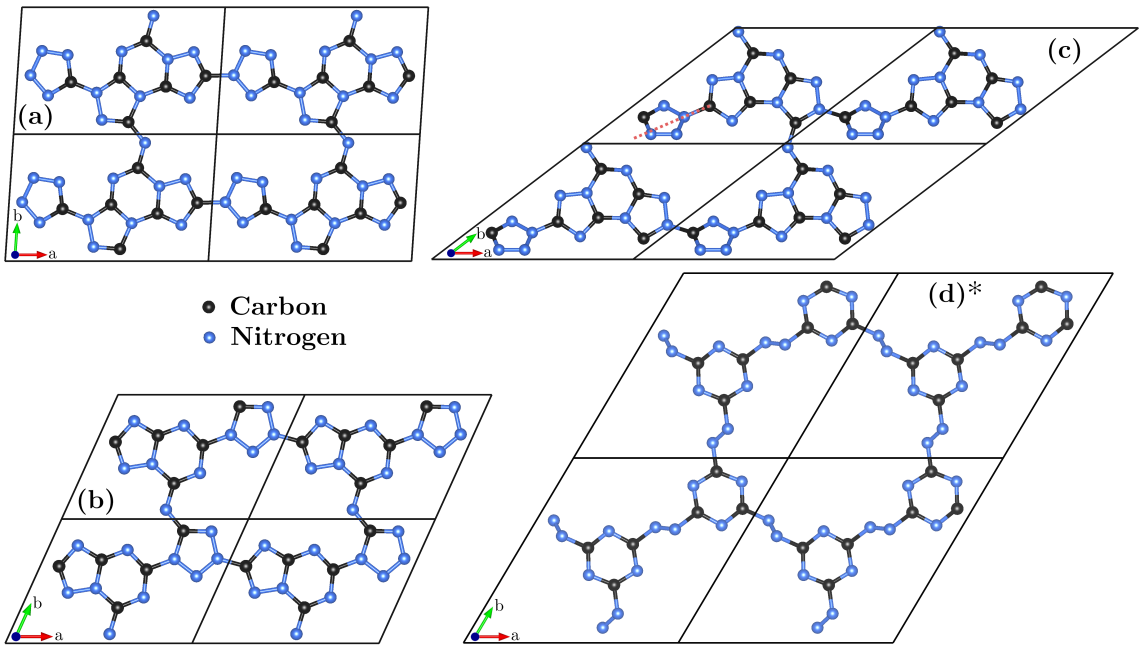

Figure 3.2.: Top view of (a) S1, (b) S2, (c) S3, and (d)* azo-bridged-triazine as obtained by DFT calculations from a variable cell shape optimization of their primitive cell. All four structures are 3D where only one layer of each is illustrated in this figure. S3 has a closed hole as S1 and S2 have but due to the strong acute angle of the unit cell, it is depicted such that the hole does not lie at the center. A different view of the S3 structure is shown in Supplementary Material.

3.2.2. Density Functional Theory Calculations

In the next step, the energetically most promising candidates, whose DFTB energies were within 0.2 eV/atom of the lowest energy for each supercell size, were refined at the DFT level. Our DFT calculations were carried out using the Vienna Ab initio Simulation Package (VASP) [88, 89] and FHI-AIMS [90] software packages, where the former exploits the projector augmented-wave method [91] and the latter is an all-electron electronic structure code. Kohn-Sham orbitals are expanded in terms of plane waves in VASP and in terms of numeric atom-centered orbitals in FHI-AIMS. We used the tier-2 basis set for both C and N elements in our FHI-AIMS calculations. The Perdew-Burke-Ernzerhof [92] (PBE) exchange-correlation (XC) functional was employed to compute total energies and forces within geometry optimization calculations. It is known that conventional XC functionals generally underestimate bandgaps, hence we used the Heyd-Scuseria-Ernzerhof (HSE06) screened hybrid XC functional to attain more accurate bandgap values and band edge positions [93]. A plane wave cutoff energy of 500 eV was adopted in all VASP calculations. Also, the Brillouin zone was sampled with a sufficiently dense mesh to guarantee a k-point density of 0.024 $Å^{-1}$ for each structure. All geometry relaxations were carried out with a convergence criterion of 0.01 eV/Å applied to the maximum force norm on an atom, with the exception of relaxed structures for our phonon calculations, in which a tighter tolerance of 0.002 eV/Å was employed. These values of cutoff energy, convergence criterion for geometry optimizations, and k-point mesh guarantee that the total energies are converged to within 1 meV/atom. Van der Waals interactions by means of London dispersion forces are necessary for an accurate treatment of CN layered structures. They are considered through London dispersion forces, whose coefficients are calculated by means of the Tkatchenko-Scheffler method with iterative Hirshfeld partitioning [94].

3.2.3. Dynamical and Thermal Stabilities

Dynamical and kinetic stabilities of the predicted structures were also investigated. The former was carried out at the DFT level using the frozen phonon approach, as implemented in the Phonopy package [95]. The atomic displacement distance of the finite difference method was set to 0.01 Å. Examining the kinetic stability of a

multitude of structures using MD simulations at the level of DFT is cumbersome and imparsimonious [96]. Machine learning interatomic potentials (MLIPs) [97, 98, 99, 100] have shown to be an efficient alternative approach, while being sufficiently accurate in reproducing PESs [101, 102, 103, 104, 105]. The reliability of the MLIPs exceedingly depends on the diversity of reference training data points. Fortunately, a large number of configurations with a substantial diversity were generated during the MH runs, i.e. along an enormous number of short MD trajectories, as well as local geometry relaxations. MLIPs are typically trained to reference DFT calculations, since the ab initio calculation of a large number of configurations with methods at a higher level of theory is very demanding [106, 107]. We performed diversity checks of the configurations before DFT calculations, because the presence of similar structures in the reference data set does not improve the quality of the MLIP, whereas it intensifies expensive DFT calculations. Also, we generated some configurations by compressing and expanding one thousand local minima. In total, we had 74370 reference training data points [108], from which 90% were used for the training process and the rest for the validation. The root mean square error of the validation data set was 35 meV/atom and 1.6 eV/Å for the total energies and forces, respectively. Even though these values are not very small, they suffice for chemical accuracy and are not unusual for such an intricate binary system, whose both elements can form single, double, and triple bonds. The isothermal-isobaric MD simulations were performed with the Large-scale Atomic/Molecular Massively Parallel Simulator (LAMMPS) software package [109]. Temperature and pressure were adjusted with the Nose-Hoover thermostat and barostat, respectively [110, 111]. Energies, forces, and stress tensors based on the MLIP were supplied by FLAME through the interface with LAMMPS. In addition, to all low-lying energy structures, some slightly higher energy polymorphs, but with distinct and peculiar structural motifs were also examined within our MD simulations. For each structure we created a supercell of roughly 1000 atoms , with which we performed a 20-ps equilibration to 600°C. Typically, CN_2 is synthesized in temperatures below 400°C [20]. We carried out the MD runs at an elevated temperature of 600°C because experimental time scales are inaccessible in computer simulations, whereas raising temperature can boost rare events and thus uncover thermal instabilities of the structures. Following the equilibration, each MD simulation was run for 1 ns,

unless the structure turned out to be kinetically unstable. The primary microscopic mechanism for disruption of a CN structure, i.e. the formation of N_2 molecules, which in practice is an irreversible process, was also verified by our comprehensive MD simulations. For this reason, we monitored the MD trajectories and whenever multiple N_2 molecules formed, the structure was labeled unstable and the molecular dynamics simulation was halted. Out of the 220 structures examined in these tests, only a handful of them turned out to be both dynamically and kinetically stable. To investigate further the microscopic mechanisms and their corresponding activation energies that are in relation to the thermal stability of our structures, we carried out two transition state searches for one structure each classified as stable and unstable. The results are demonstrated in the supporting information.

3.2.4. Other Computational Details

The symmetry points of the first Brillouin zone for our phonon calculations, as well as our electronic band structure calculations, were obtained using the Sumo package [112]. The crystal structures have been drawn using the Visualization for Electronic and Structural Analysis (VESTA) program [113]. Preliminary relaxation of the structures in the screening step after our MH search runs, the phonon calculations, and the generation of the DFT reference values for the MLIP training were all performed with VASP, and the rest of the DFT calculations were carried out with FHI-AIMS. It should be noted that the total energies, enthalpy values, and electronic band structures presented in this paper were also obtained with the FHI-AIMS code. The geometries as relaxed with the two codes are virtually identical.

3.3. Results

The crystal structure runs discovered many energetically low-lying structures. However, many of them exhibited imaginary modes in the phonon calculations or turned out to be unstable within molecular dynamics simulations. Only three CN_2 polymorphs passed the dynamical stability test and did not liberate any N_2 molecules during the MD simulations. Figure 3.2 shows all three lowest-energy structures, labeled S1, S2, and S3, as well as a structure based on the polymorph given in

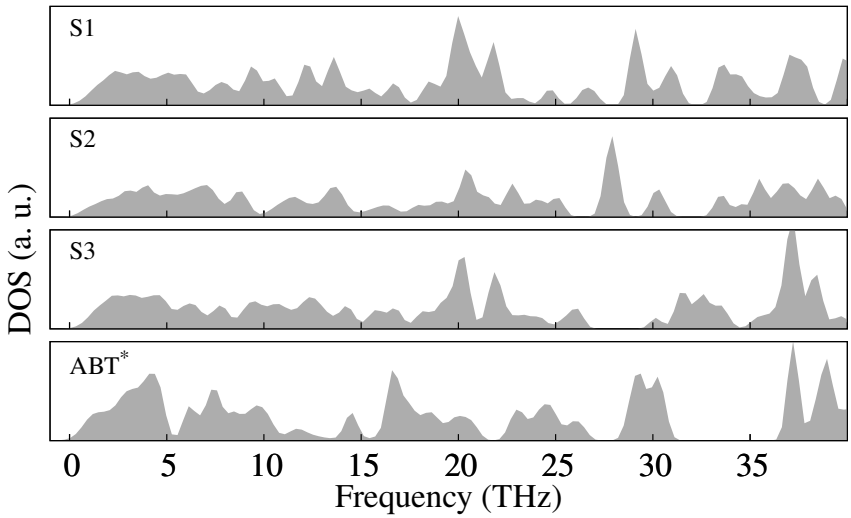

Figure 3.3.: Phonon DOS of the four polymorphs depicted in Figure 3.2. All curves were smoothed for clarity using Gaussian filters.

Ref. [79]. The asterisk on Figure 3.2d* is to emphasize that this structure is not obtained within our structure search. S1 and S2, shown in Figure 3.2a and Figure 3.2b, respectively, are energetically degenerate in the PBE approach at the level of accuracy of the parameters considered herein.

S3 has structural motifs identical to those of S1, but they differ in arrangement, which results in an energy difference of 19 meV/atom. The nitrogens in all three structures are considerably locked up in the moieties; only one nitrogen atom in the lattice is available to bridge the building blocks. This could be one vital reason for the stability of the polymorphs found in our search. The tetrazole is the common moiety in all three structures. Moreover, S1 and S3 have a moiety based on bis-triazolo-triazine, and S2 contains $[1,2,4]$triazolo$[1,5-a][1,3,5]$triazine units. As described in Sec. 3.2, the maximum time scale used to determine the thermal stability of the structures was 1 ns. However, S1 was run for an extended time of 10 ns to further confirm its robustness. The geometry of S1 and S2 is a planar structure, whereas S3 is quasi-planar due the twist of the lone tetrazole unit around the axis represented by the dotted line in Figure 3.2c.

A prominent structure was recently proposed for CN_2 based on the triazine moiety [79], and its monolayer was later investigated as a gas sensor [114]. It was conceived to be a fully flat configuration in which triazine units were bridged by azo linkages, leading to a highly porous atomic lattice. Herein, we refer to the structure

as azo-bridged-triazine (ABT). Using the structure coordinates given in the supporting information of Ref. [79], relaxing as a bulk material, and following up with phonon calculations, we obtained markedly large imaginary phonon modes, despite the report of a fully positive phonon dispersion in the referenced paper. On this basis, we relaxed a supercell of 2×2 unit cells in which atoms had been randomly disturbed with a small amplitude of 0.01 Å. The structure turned out to be unstable, while the basic units remained intact, and the planar framework buckled through the out-of-plane displacement of azo linkages. The discrepancy between our phonon dispersion and theirs may stem from their phonon analysis being based on an MLIP, whereas ours was obtained at the DFT level. The change in the structure resulted in a lowering of energy by 42 meV/atom. In this paper, we refer to the buckled ABT as ABT*, emphasizing the minor difference. Worth noting is that ABT* is dynamically stable and does not show any imaginary modes. In addition, the MD trajectories indicate kinetic stability of ABT*, as was previously asserted for ABT in Ref. [79] as well. Nonetheless, ABT and ABT* have considerably higher total energies than S1, S2, and S3. Figure 3.3 illustrates the phonon DOS of S1, S2, S3, and ABT*, respectively.

It is worth mentioning that the structural motifs of S1, S2, and S3 differ from those speculated in the experimental study (as depicted in Figure 2 of Ref. [20]) of Vinu and coworkers. However, our calculations and their prediction both suggest the dominance of pentagonal units within the moieties of the CN_2 composition. This is in contrast to the polymorph shown in Figure 3.2d*, which features no pentagonal, but hexagonal units based on triazine.

Table 3.1 lists energetic, structural, and electronic properties of S1-S3 and ABT*, as well as available structures in the literature. S1, S2, and S3 all have significantly lower density than the polymorphs given in Refs. [77] and [76], respectively. This is not surprising, since the majority of these structures have been proposed as high-pressure phases of CN_2 and some may even be dynamically unstable at ambient conditions. Nevertheless, the contrast in densities of the structures presented in this paper as compared to the high-pressure phases is remarkably interesting for applications requiring pores in the structure. As higher porosity can facilitate the flux of reactants to active sites, enhancement of the efficiency of storage systems and the catalytic activity of photocatalysis systems with the material is expected. As a

Table 3.1.: The number of atoms in the primitive cells (N_{pc}), the total energies with respect to the energetically lowest candidate, the mass densities, and the bandgaps of the structures proposed in this study, as well as conformations whose coordinates are readily available in the literature. The structural labels of allotropes from other studies are based on their crystallographic space groups, except for ABT, which is the acronym of its building blocks.

Structure	Ref.	N_{pc}	E [eV/atom]	Density [g/cm^3]	Bandgap [eV]
S1	This work	18	0	1.99	2.8
S2	This work	15	0.000	2.00	2.4
S3	This work	18	0.019	1.93	2.6
ABT*	[79]	18	0.179	1.17	2.8
$P\bar{4}2_1m$	[77, 76]	6	0.220	2.86	–
$I\bar{4}2d$	[76]	12	0.377	3.72	–
$P\bar{3}m1$	[76]	6	0.447	2.90	–
$Cmc2_1$	[76]	6	0.514	3.67	–
$I\bar{4}m2$	[76]	3	0.537	3.68	–

result of relatively sizable pores in the lattices, S1, S2, and S3 have large volumes of 11.16, 11.08, and 11.48 Å^3/atom, respectively. It is worth noting that these structures have an even larger volume per atom than the well-known, void-containing, heptazine-based g-C_3N_4, whose volume with AB stacking is 10.27 Å^3/atom.

Moreover, our enthalpy versus pressure inspection indicates that despite being low-density, S1, S2, and S3 are thermodynamically more stable than known high-pressure phases up to a moderate external pressure of about 10 GPa. Figure 3.4 illustrates enthalpy difference as a function of pressure for S1, S2, and S3, as well as the most competitive known high-pressure phase, namely the so-called penta-CN_2, which is listed as $P\bar{4}2_1m$ in Table 3.1.

Tetrazole is the basic unit of the precursor used in Ref. [20] to synthesize the nitrogen-rich C_3N_7 and C_3N_6 compounds. We envision that experiments with a mixture of precursors consisting of tetrazole and triazolo-triazine basic units can result in structures similar to those presented in this study. Because the strong triple

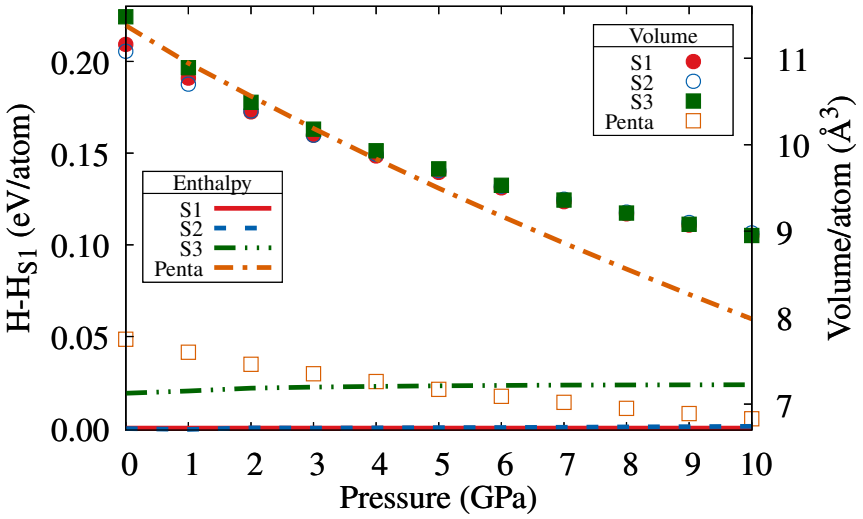

Figure 3.4.: The lines are calculated enthalpy difference of S2, S3, and penta-CN_2 with respect to S1 as a function of pressure. S1 corresponds to the horizontal solid line at zero. The points with scaling shown on the right axis illustrate the volume of the aforementioned structures.

bond in an N_2 molecule makes it highly stable, it is expected that N_2 molecules are irreversibly formed along the synthesis pathway of high temperature synthesis strategies. Other nitrogen-rich precursors may also be usable for the synthesis of our structures. However, a large chemical potential of nitrogen molecules, μ_{N_2}, is required to achieve such a large concentration of nitrogen within the CN framework. In several studies, the thermodynamic stability of CN compounds have been theoretically investigated based on Gibbs free energy analyses [115, 75, 77]. Chemical potentials of nitrogen molecules may be crucial if synthesizing CN_2 compounds composed of pentagon-based nitrogen-rich moieties when the precursors are hexagon-based units.

It should be pointed out that within the phonon calculations, whose phonon DOS are shown in Figure 3.3, S2 exhibits very small imaginary frequencies. They may be due to noise in interatomic forces, or because of limitations of the ground state-based perturbation method, i.e. the frozen phonon approach. In such circumstances, anharmonic effects must be taken into account to precisely determine the dynamical stability of the structure. Based on our MD simulation of S2 at an elevated temperature of 600°C for 1 ns, we consider S2 to be stable. Phonon calculations of ABT* also result in small imaginary frequencies, which are larger than those of S2.

However, the same arguments apply, and we consider it to be a dynamically stable polymorph.

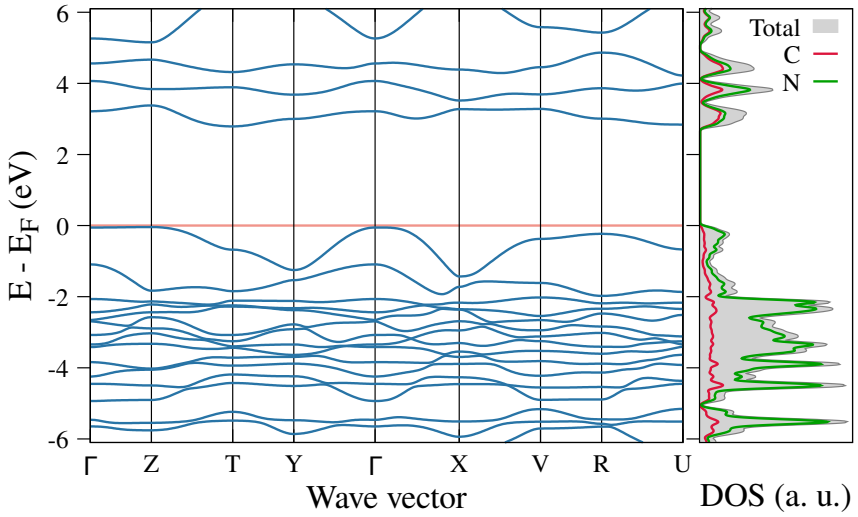

Figure 3.5.: Calculated electronic band structures and DOS of bulk S1. The occupied states near the VBM are dominated by electrons of the nitrogen atoms.

Figure 3.5 shows the electronic band structure and density of states (DOS) of S1. The valence band is maximum at the Γ point, while it exhibits a rather flat profile from the Γ to Z point in the reciprocal space. The flat band may be associated with the p_z orbitals of N atoms that result in an enhanced electronic DOS at the valence band maximum (VBM). Apart from the aforementioned path, the valence bands exhibit a dispersive profile. The predominance of nitrogen electrons at the VBM occurs in other CN stoichiometries as well, and it has been investigated theoretically and experimentally [116, 117]. Electrons of both C and N atoms contribute to the conduction band minimum (CBM). Figure 3.6 depicts the electronic band structure and DOS of S2. In contrast to S1, the valence bands of S2 do not show any flat patterns. Furthermore, bands associated with N atoms are dominant at the CBM as well, which is atypical in the case of g-C_3N_4. The electronic band structure and DOS of S3 are illustrated in Figure 3.7. Since S1 and S3 share the same basic units and differ only in the network connecting the moieties, it is not surprising that their electronic bands and DOS are nearly identical. The only difference is that the flat band from the Γ to Z point in reciprocal space is not flat but has a slight inclination in S3. S1 and S3 have a bandgap of 2.8 and 2.6 eV, respectively, comparable to

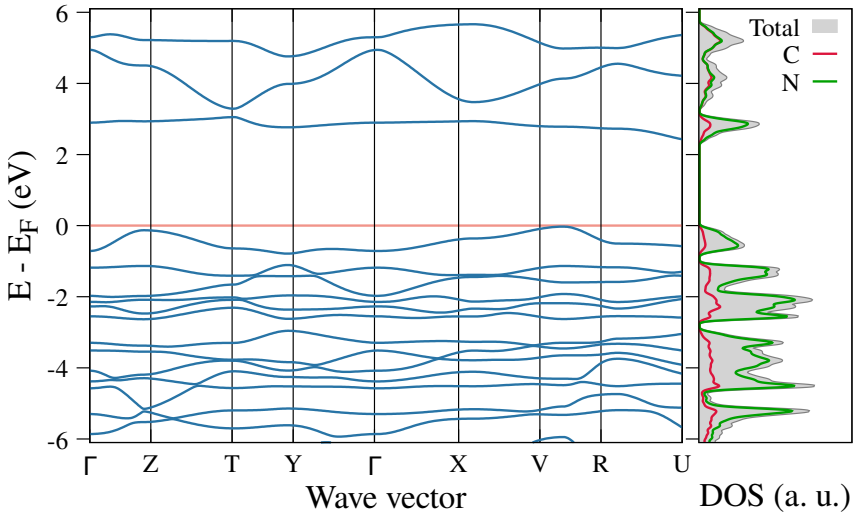

Figure 3.6.: Calculated electronic band structures and DOS of bulk S2. The occupied states near the VBM, as well as the unoccupied states near the CBM are dominated by electrons of the nitrogen atoms.

that of g-C_3N_4 with 2.7 eV [51]. S2 seems to be a more attractive candidate for photocatalysis due to the lower bandgap of 2.4 eV, by which it can absorb a greater extent of sunlight. Nevertheless, compositions with a smaller bandgap and higher photocatalytic activity can be achieved by introducing defects into the system, e.g. by short-time heat treatment, as is done in the case of g-C_3N_4 [118]. Indeed, it is known that the fast recombination rate of photogenerated charge carriers in CN compounds is a limiting factor in their photocatalytic performance [119].

Despite the predominance of strong covalent bonding networks in CNs, there is a small degree of charge transfer, even in pristine g-C_3N_4 [120]. Therefore, a basic AA stacking is energetically unfavorable, and the layers must be aligned to minimize the repulsive forces between charged particles and to impose a maximal distance between π-electrons of adjacent layers. Since single layers of S1, S2, and S3 have low-symmetry configurations, the stacking of their monolayers in the bulk phase is intricate and does not retain the renowned and trivial stacking styles of AA, AB, or ABC. This makes an assessment of the band alignments of their bulk systems a challenging task. For this reason, we gauge the band edges of S1, S2, and S3 monolayers and compare them with a single layer of the well-studied heptazine-based g-C_3N_4. In the case of S1, we perform exclusively a minima hopping run for ten stacked layers of S1 based on our MLIP potential. The resulting lowest

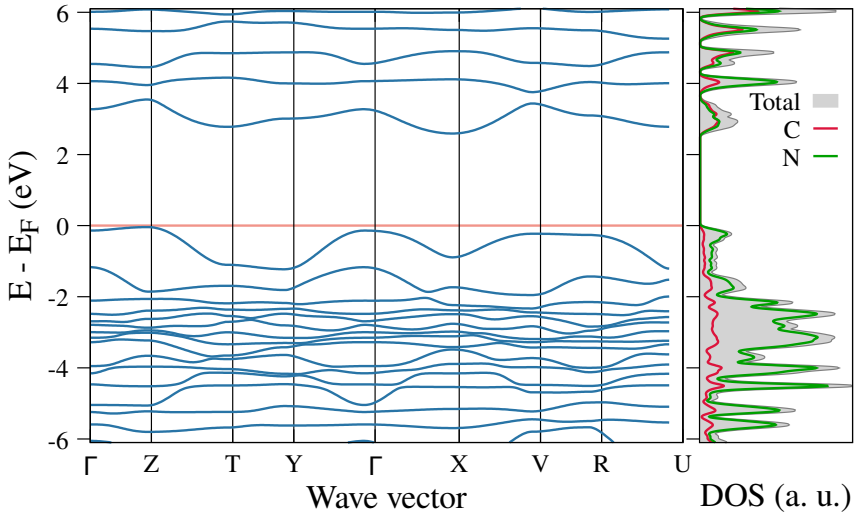

Figure 3.7.: Calculated electronic band structures and DOS of bulk S3. The occupied states near the VBM are dominated by electrons of the nitrogen atoms.

energy structure has been used to elaborate on the band gap and band edges of the bulk S1 versus the vacuum level. As expected, the ten-layer slab has a lower band gap than that of the monolayer and the value is virtually identical to that of bulk S1. The structure of the ten-layer system is available in Ref. [108] In fact, our analysis is based on two sufficiently distant monolayers, one of which is inverted. This is done to vanish the dipole moment of a monolayer, which makes the task of band alignment to the vacuum level convenient. We performed a convergence test to examine the impact of the vacuum on the two sides of the two-layer system as well as the distance between the two layers on the band gap and edges. The results of the convergence test are illustrated in the supporting material, Figure *S*4. The bandgap values of a single monolayer and two distant monolayers have been checked, and they are identical. Figure 3.8 shows VBM and CBM energy levels as aligned to vacuum and compares them with those of the heptazine-based g-C_3N_4 monolayer. Single layers indeed have larger bandgaps than their bulk counterparts. This behavior is known to be valid for a large class of materials, and it is associated with the stronger quantum confinement of charge carriers in ultrathin slabs and 2D materials as compared to extended systems in all three dimensions. This point has been experimentally investigated for g-C_3N_4, and the result was that porous nanosheets had both a larger bandgap and higher specific surface area [121]. It has

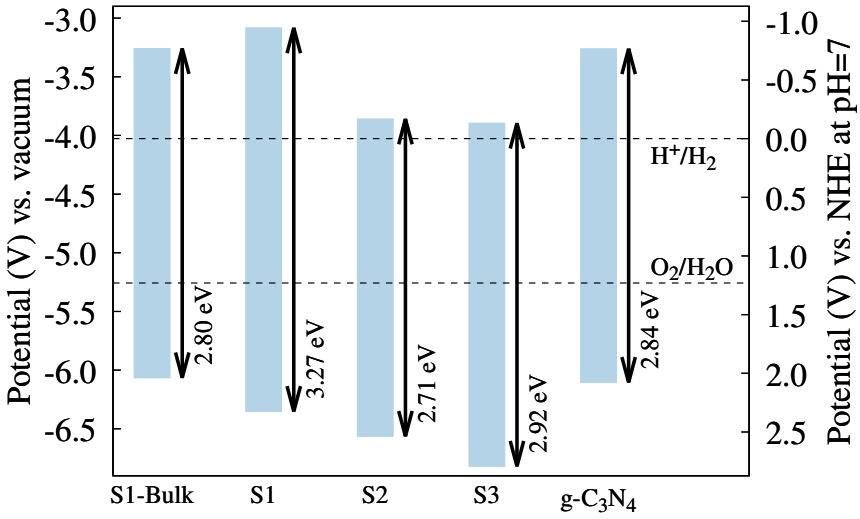

Figure 3.8.: Band edge positions of S1, S2, S3, and heptazine-based g-C_3N_4 monolayers with reference to the vacuum level (left axis) and the water redox potentials H^+/H_2 and O_2/H_2O at pH=7 (right axis). All results shown in this figure are calculated for a monolayer, namely 2D conformations, except S1-Bulk. The band gaps are slightly larger than the 3D counterparts whose values are listed in Table I.

also been confirmed by DFT calculations in various theoretical studies. As shown in Figure 3.8, the band edges of all three structures lie at suitable positions with regard to H^+ reduction, water oxidation, or both. Although the bandgap narrows in the case of bulk systems, S1 is expected to retain its compelling features for photocatalytic water splitting, while S2 and S3 may also remain interesting if the transformation of their energy levels is essentially associated to the valence bands. Nonetheless, further investigation on this point is required for a solid conclusion. Generally, the electronic characteristics of the presented structures are not much different from those of the well-known g-C_3N_4. Therefore, they are expected to demonstrate reasonable photocatalytic performance, although probably at a higher rate due to the abundance of nitrogen sites.

3.4. Conclusion

We performed a systematic inspection of possible crystalline structures of CN_2 to predict thermodynamically and thermally stable polymorphs. Owing to the intricate nature of C-C, N-N, and C-N bonds, the energy landscape of CN systems is enormously complex. For this reason, we employed a variety of computational techniques, ranging from MLIP to DFTB and DFT, to tackle challenges therein. The crystal structure prediction was based on DFTB, and it was comprised of numerous independent runs with diversified starting points. In the second step, we refined the list of possibly stable configurations at the level of DFT, followed by MD simulations based on an MLIP to assess the thermal stability of the predicted structures. Ultimately, three polymorphs were found to both have low energy and be kinetically stable. These structures are formed by in total three nitrogen-rich moieties, of which tetrazole has already been successfully used as a precursor to synthesize a CN_2 compound. The other two moieties are somewhat larger, and they might form during a synthesis process through the condensation of smaller molecules, or via the thermal decomposition of molecules similar in size and stoichiometry. We envisage that with the use of appropriate precursors and synthetic strategies, our theoretically predicted polymorphs can be experimentally realized. Interestingly, up to a modest value of external pressure, they have a lower enthalpy than proposed structures for a high-pressure regime in the literature. Our DFT calculations at the level of a hybrid exchange-correlation functional indicate that the proposed structures are not only much more thermodynamically stable than their counterparts in the literature, but also applicable in photocatalytic water splitting due to the suitability of their bandgaps and band edges for H^+ reduction or water oxidation.

4. Towards CN_2: Novel Carbon Nitride Materials with Ultra-high Nitrogen Content

This research project follows the previous structure prediction and has the goal of synthesizing a carbon nitride with CN_2 stoichiometry. As evaluated above, azo-bridged triazine has promising potential, and it arouses the chemists' mind by its pure symmetry and simplicity, as it consists only of triazine units linked by an azo group. The theoretical calculations and the synthesis work for this project were carried out by me. The XRD, XPS, SEM, TGA, and electrochemical measurements, as well as the photocatalytic experiments, were performed with significant contributions from the co-authors.

4.1. Introduction

Carbon nitride materials have garnered significant interest due to their diverse chemical properties and promising applications in areas such as (photo)catalysis[4, 122, 123], energy storage [124, 125], sensing [126, 127], and gas separation or storage [128, 129, 130]. These materials cover a wide range of stoichiometries, including but not limited to C_2N [13], C_1N_1 [129], C_3N_4 [122, 128], and C_3N_5 [131, 132], each providing unique structural motifs and electronic properties that critically affect their reactivity and functional performance. Several promising strategies have been formulated to enhance their catalytic activity, with metal doping [133, 134] serving as a successful example. Increasing the nitrogen content can augment surface basicity and significantly alter the electronic structure and adsorption characteristics, thereby increasing the catalytic potential of these materials. Although certain highly

nitrogen-rich carbon nitrides, reaching levels as high as C_3N_7[135], have been synthesized and characterized experimentally, the development of C_3N_6 (CN_2) materials remains in its nascent stages, as the incorporation of higher nitrogen concentrations while maintaining structural integrity is a significant challenge. Recent studies have suggested nitrogen-rich carbon nitrides with CN_2 stoichiometry, featuring azo-linkers connecting triazine units, as promising candidates for photocatalytic applications. Several theoretical studies have explored the physicochemical characteristics of this framework, forecasting potential applications in gas storage [136], chemical sensing [21], pollutant degradation [22], and analyses of mechanical, thermal, electronic, and optical properties [10, 23, 50]. These studies underscore the importance of high nitrogen content in enhancing functional performance, but also highlight the synthetic challenges and limited experimental realization of such phases. A suitable experimental example of these challenges is a recent paper by Yu et al. [137], which purportedly synthesizes azo-bridged triazines, yet fails to provide credible evidence, thereby underlining the difficulty of such synthesis.

In this work, we introduce the synthesis of this novel CN_2 material, with azo-linked triazines, employing two complementary strategies: a solution-based organic synthesis path and a high-temperature, solvent-free thermal condensation. Both methodologies are designed to maximize nitrogen incorporation while fostering the formation of stable crystalline structures. The resultant materials are characterized with several spectroscopical methods to authenticate their structural and compositional attributes. Their photocatalytic performance is evaluated by the production of hydrogen peroxide (H_2O_2) in water under visible-light irradiation, a reaction of increasing interest due to its significance in green chemistry and industrial applications. By synthesizing and investigating these CN_2 materials, this study aims to advance the understanding of nitrogen-rich carbon nitrides and their potential.

4.2. Experimental

Following the principles of green chemistry, every chemist should strive to design reactions in a way that waste and energy consumption, as well as the use of hazardous or nonrenewable substances, are avoided as much as possible. This usually includes

a compromise between the principles. Here, the synthesis is kept very simple and the sole reaction is a nucleophilic aromatic substitution of chlorine in tri-chloro-triazine through hydrazine, or the subsequent hydrazine-triazine adduct, as shown in Fig. 4.1. This step is repeated multiple times to gain crosslinked two-dimensional layers. As a one-pot approach with low temperatures, it has relatively little chemical waste and low energy usage, although the reactants are hazardous, which resembles our compromise. We explored two pathways for this reaction. Initially, a wet synthesis was explored and developed, but to reduce the amount of chemicals used and wasted, such as solvents, and to simplify the reaction, a molten salt-assisted oven synthesis was developed, inspired by many successful examples of carbons and carbon nitrides [138, 139, 140].

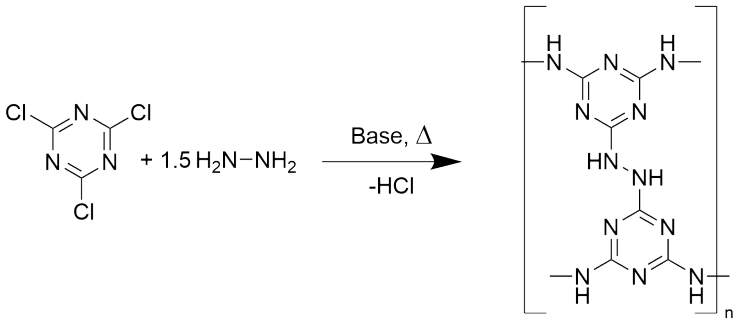

Figure 4.1.: Reaction follows S_NAr mechanism and proceeds under various conditions.

4.2.1. Synthesis of Materials

4.2.1.1. Wet Synthesis

ACN-75: 1 M hydrazin [26 mL, 26 mmol], stabilized in THF, together with an excess of diisopropylethylamine (DIPEA) [10 mL, 7.43 g, 57.5 mmol] was added to 75 mL of acetonitrile. The clear solution was degassed with N_2 and heated up to 75 °C. Tri-chloro-triazine (TCT) [2.4433 g, 13.2 mmol], suspended in 25 mL degassed acetonitrile, was added dropwise to the solution, forming an initially yellow, but fading to white solid. Upon further addition of TCT, the color of the solution shifts to rose and finally to orange. The dispersion was stirred for 48 h at 75 °C. The precipitate was washed with acetonitrile, water, and ethanol. After drying at 120 °C and 40 mbar, 1.8355 g product were retrieved, which is equal to 14.9 mmol

and 112.9 % yield, if fully condensed to H-ABT, which is more than the initial amount of TCT. We therefore conclude that a larger number of not-fully condensed molecules exist that incorporate more terminal groups, such as chlorine, oxygen, or amines. Additionally, solvent molecules show very strong adsorption and do not fully gas out during drying.

4.2.1.2. Oven Synthesis

Solvent-free synthesis in the oven allows higher temperatures and the use of structure-directing salt melts, in this case a salt mixture consisting of KCl and LiCl in a 40/60 mol% ratio, with a melting point of 352 °C. Salt melts of KCl / ZnCl and KCl / KH_2PO_4 have been studied, as well as different temperatures, but did not yield the desired carbon nitride material. Tri-chloro-triazine [1.5406 g, 8.36 mmol] was well mixed with KCl [8.17 g] and LiCl [6.83 g] in a crucible. Then an excess of hydrazine hydrate [80% hydrazine, 10 mL] was added dropwise. An exothermic reaction occurred immediately, forming a slightly yellow solid. Hydrazine is proposed to be used as a reaction partner as well as a base to adsorb the HCl that forms during the reaction. The mixture was placed in an oven with nitrogen atmosphere and slowly heated to 360 °C, where it was kept for 2 h. Afterwards, it was washed with slightly acidic water to remove remnants of the salt mixture. After drying at 120 °C and 40 mbar, 0.8635 g of product were obtained, corresponding to 83.9 % yield.

4.3. Results and Discussion

4.3.1. Computational

Detailed analysis regarding the charges in the material, adsorption properties, and layer stacking is performed computationally not only for ABT but also for the hydrogenated state of the material, H-ABT, where the bridging nitrogen atoms carry an additional hydrogen. All DFT simulations have been conducted using CP2K [141, 142] in Version 2023.1, via Gaussian plane wave approach [143] with periodic boundary conditions and a cutoff of 500 Ry. Orbitals were described via double-

zeta basis set for short ranges, longer – van der Waals interaction were taken into account via damped atom-pairwise dispersion correction [144]. As an exchange and correlation functional, Becke based B97-3c was used [37]. To calculate net atomic charges, the DDEC6 method was used, as implemented in Chargemol [145, 146]. Images have been created using VMD [147].

The structure and stacking of the 2D layers were studied without restrictions in cell shape or size, but limited to four layers in a cell. The resulting stacking does not follow a recognizable pattern, such as AA or AB, and consists of individual 2D layers slightly shifting compared to the upper and lower layers, as can be seen in Figures S1 and S2. The resulting interlayer distance is 3.1 Å.

The pyridinic nitrogen in triazine carries a charge of slightly less than half an elemental charge for ABT, and slightly more for H-ABT, as shown in Table 4.1. The same increase of electron allocation can be observed for the bridging nitrogen atoms, and it is explained mostly by the additional electron donation of the attached hydrogen atoms and, to a minor extent, by the carbon atoms. This has a tremendous influence on the adsorption energies and orientation of adsorbed molecules.

Table 4.1.: Comparison of the charges in ABT and H-ABT, in units of elemental charge [e], the deviations are below 0.01 e.

Structure	$N_{arom.}$	$N_{bridg.}$	$C_{arom.}$	H
ABT	-0.42	-0.06	+0.49	-
H-ABT	-0.58	-0.23	+0.53	+0.28

In Table 4.2, the adsorption energies of gas-phase water, carbon dioxide, and nitrogen are shown. Adsorption is the first step in any catalytic process, and determines whether a reaction occurs or not. We observe a relatively strong adsorption for all of these gases, which allows the materials to interact as a catalyst, transfer electrons, or store gas. As described above, the differences in charges observed lead to an overall increase in coulombic interactions and thus to better adsorption energies for H-ABT. Furthermore, if hydrogen bonds are involved, as in the case of water, a different orientation of the molecule can be observed, which is depicted in Figure S3. In the literature, even higher adsorption energies were observed by introducing metal atoms into the system [21, 23].

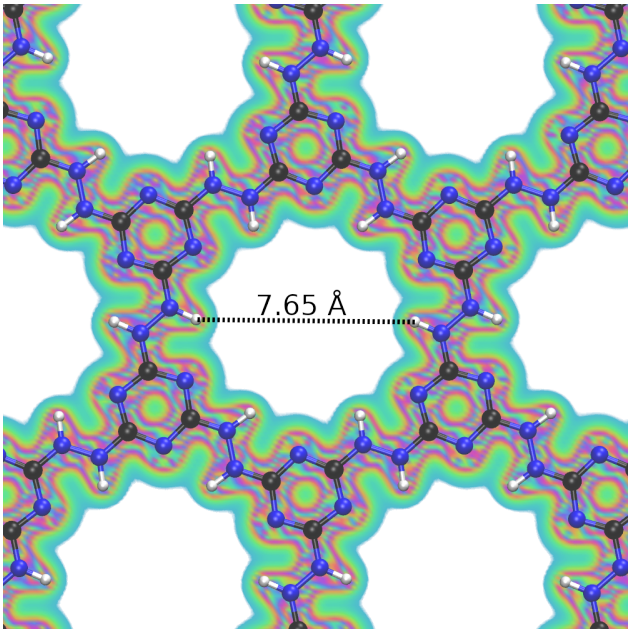

Figure 4.2.: $|\Psi|^2$ visualized for H-ABT, with a pore diameter of 7.65 Å between hydrogen atoms (9.35 Å between nitrogen atoms in ABT) with blue indicating the least and red the highest probability.

Table 4.2.: Adsorption energies of various gases, given in $\frac{kJ}{mol}$.

Structure	H_2O	CO_2	N_2
ABT	-31.1	-25.0	-17.9
H-ABT	-39.8	-36.0	-25.1

The density of states (DOS) diagram in Figure 4.3 presents the electronic state contributions from three atom groups in ABT. N_{azo} exhibits the highest orbital density near the band gap. As it also serves as the preferential adsorption site, photoexcited states may directly excite adsorbed molecules without requiring electron transport.

4.3.2. Experimental

This section is divided into two parts. In the first part, we discuss the results of various analytical techniques to explore the nature and structure of our synthesized product, and afterwards, potential applications are explored. In principle, the chemical differences between the synthesis of samples are rather low, therefore IR, UV-VIS, elemental analysis and XRD analysis differ only in detail. However, these

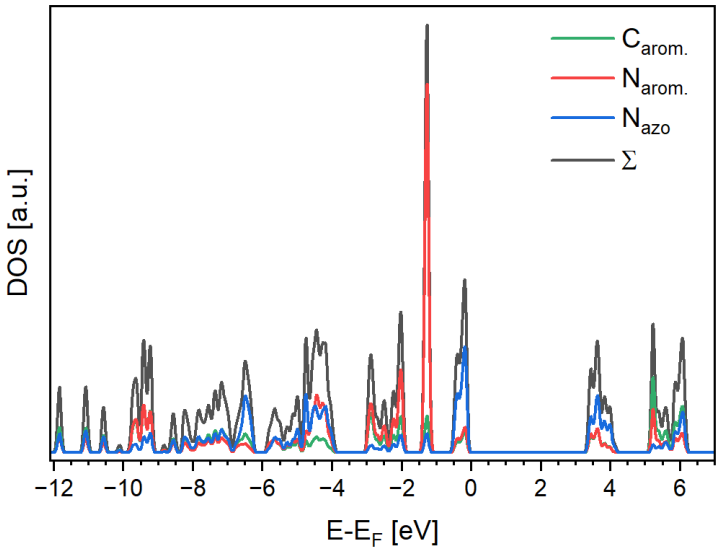

Figure 4.3.: Density of states plot for ABT. Near the band gap, the dominant contributions originate from the bridging azo-nitrogen atoms.

details lead to the conclusion that the wet synthesis at 75 °C yielded a small condensed system with many terminal groups and the oven synthesis at 360 °C a larger, more amorphous material. Furthermore, we observed that during either photocatalysis or treatment with a basic solution, the oven-synthesized material SM-360-yellow turns violet, and to study and explain this phenomenon, we include this material as SM-360-violet. All three are depicted in Figure 4.4.

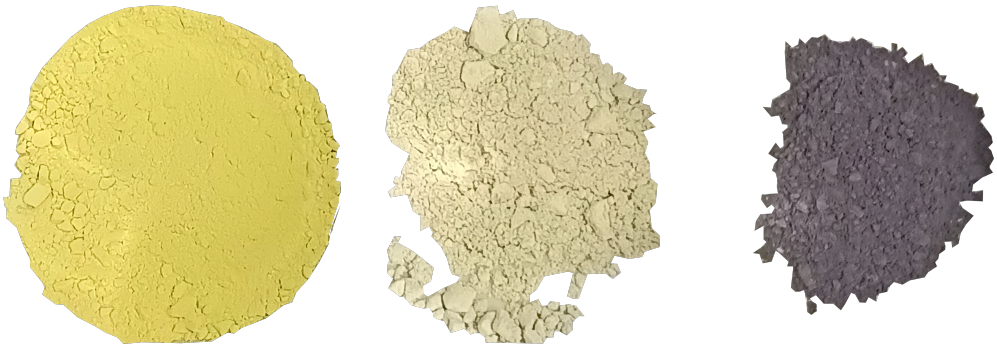

(a) ACN-75. (b) SM-360-yellow. (c) SM-360-violet.

Figure 4.4.: Pictures of the materials to visualize differences in color.

Combustion elemental analysis measurements are summarized in Table 4.3. The presented yield follows the constraint discussed in the Synthesis of Materials section. The C/N ratios are close to 0.5, and the materials possess a considerable amount of hydrogen, which could be from terminal amines, adsorbed gases, or hydrogenated

Table 4.3.: Elemental analysis results of the prepared samples are reported in weight percentages (averaged from two measurements). The yield is calculated from the molar amounts, the C/N ratio is derived from atomic ratios, and all other values are given as weight percentages

Sample	Yield	C/N	Carbon	Nitrogen	Hydrogen	Total
ACN-75	112.9*	0.56	28.1	58.7	5.2	92.0
SM-360-yellow	83.9	0.54	26.4	56.7	3.3	86.4
SM-360-violet	-	0.55	27.0	57.4	3.1	87.5

Salt mix (SM) consist of KCl and LiCl mixture in 2:3 ratio

* calculated for fully condensed material, but terminal groups, especially chlorine, and strong adsorbed solvent molecules can distort the result

azo-bridges, as in H-ABT. Especially for ACN-75, the higher hydrogen content coincides with a larger amount of terminal groups and smaller crystallites compared to the other two materials. The total sum of percentages is lower than 100 % and indicates the presence of other elements such as oxygen or chlorine.

Figure 4.5 presents the IR data. Despite the differences in color and UV-VIS spectra, the IR signals of SM-360-yellow and -violet are virtually identical, verifying that no significant chemical change occurred during photosynthesis and basic treatment. ACN-75 is also well comparable to these two for major parts of the spectra, but differs in minor peaks. A second difference can be observed in the overall appearance: ACN-75 has narrow, sharp peaks, and the SM-structures have rather broad peaks. This can be associated with larger molecular units in the first case and larger condensed, cross-linked networks in the latter. In the high-frequency region, peaks around 3000 cm^{-1} arise due to -NH, -NH_2, and -OH stretching modes from terminal groups. Carbonyl groups can be found at 1740 cm^{-1}, which indicates that ACN-75 has some tautomerizing hydroxyl groups, potentially introduced by H_2O added to the reaction together with hydrazine. Dominant for triazine-based carbon nitride structures are signals around 1560 cm^{-1} and 1420 cm^{-1}, caused by N-C=N bending and N=N asymmetrich stretching, potentially overlapping with stretches and bending of C-N, causing the shoulder and peaks around 1250 cm^{-1}, while peaks at 1080 cm^{-1} are assigned to -N-N- stretching vibrations [148, 131, 149]. Typically

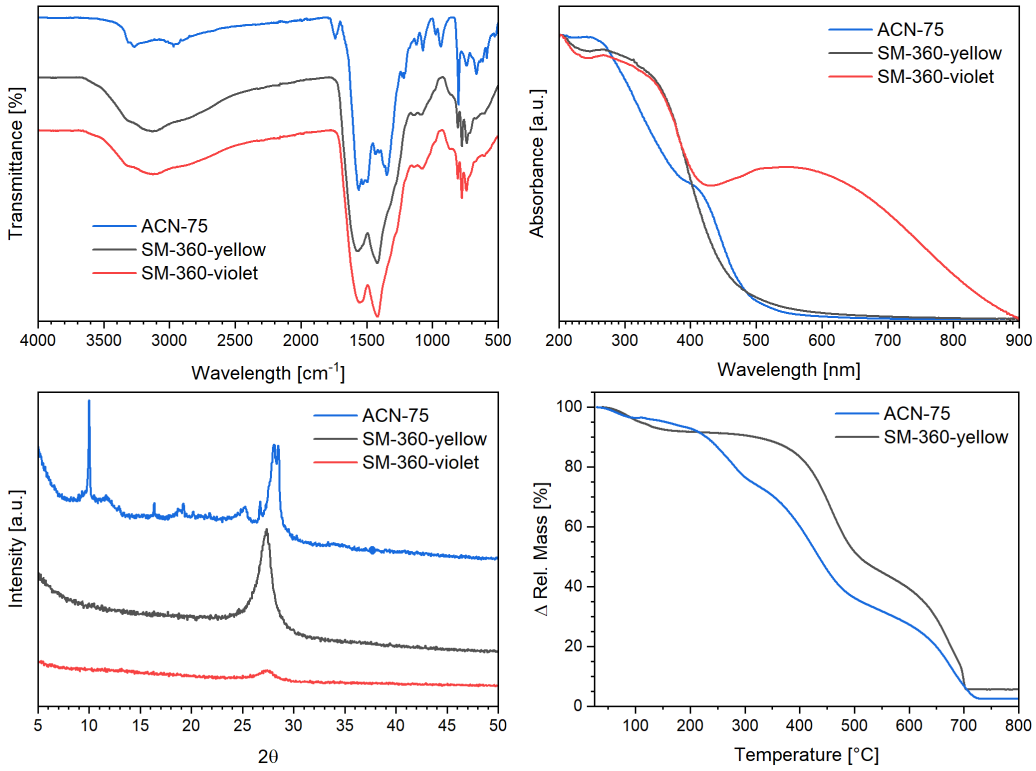

Figure 4.5.: Comparative analytical characterization of ACN-75, SM-360-yellow, and SM-360-violet samples, including FTIR spectra (top left), UV-Vis absorption (top right), XRD (bottom left) and TGA (bottom right).

for triazines is the ring stretching peak around 810, here very visible for ACN-75 at 803 cm^{-1}, while it is split into two peaks at 810 cm^{-1} und 775 cm^{-1} for the salt melt samples, which indicates chemical differences in triazines, e.g. by attached chlorine or oxygen heteroatoms, and is occasionally observed for carbon nitride materials [150]. Peaks at 740 cm^{-1}, found for all structures, are assigned to NH wagging and hint to terminal groups and H-ABT. Overall, the IR spectra agree well with the expectations for azo-bridged triazine.

UV-VIS measurements are shown in Figure 4.5. Ideally, photocatalytically active materials should exhibit strong absorption in the short-wavelength region of the visible spectrum, as this part of the sunlight is both the most intense at the Earth's surface and energetic enough to drive many reactions. All measured materials exhibit strong absorbance in the UV region, with a significant decrease as the wavelength increases into the visible region, with steep absorption edges around 450 nm. This absorption is assigned to $\pi \rightarrow \pi^*$ transitions found in extended aromatic systems. While ACN-75 has a shoulder, SM-360-violet displays a broadened and extended

absorption profile into the visible region, with significant absorbance persisting up to approximately 800 nm. Both can be attributed to $n \rightarrow \pi^*$ excitations, for the transition of lone-pair electrons from sp^2-hybridized nitrogen. This correlates with structural distortion, since this transition is forbidden for perfect symmetric systems [151, 152]. This extended absorption suggests an enhanced light-harvesting capability in the visible range, which may be advantageous for certain photocatalytic applications under solar irradiation.

Figure 4.5 shows the XRD pattern of the three samples. Salt-melt directed structures show a significant broad diffraction peak at 27.4° which is observed for many two-dimensional carbon nitrides and typically corresponds to the interlayer distance of 3.25 Å [4]. The decrease in intensity observed for SM-360-violet compared to SM-360-yellow may be attributed to structural characteristics such as broader stacking patterns induced by bonded hydroxy groups or deprotonation. However, it could also result from instrumental effects, including differences in the detector sensitivity or sample alignment. The broad nature of both peaks indicates larger crystallites in an amorphous material, while ACN-75 exhibits more defined peaks at 28.1 and 28.5°, leading to the conclusion that we have a smaller and less condensed system, which is explained by the lower synthesis temperature used. The sharp peak at 10° corresponds to a distance of 8.84 Å, correlating well with the calculated pore size of 7.65 Å and 9.35 Å, shown in Figure 4.2.
While all these values deviate by 0.2-0.3 Å from the calculated stacked layer distance of 3.1 Å, it is important to consider the idealized perfectly crystalline nature of the computational model alongside the defect-rich, amorphous structure of the synthesized materials. Under these circumstances, the correlation is more than satisfactory.

To assess the sample stability, TGA measurements were conducted. All samples gradually decompose as temperature rises, but each exhibits unique characteristics. Up to around 200 °C, adsorbed solvents or other residues, primarily water, are evaporated. The materials then undergo decomposition, as between 350 °C and 550 °C, ammonia is detected, likely originating from the terminating groups, along with increasing NO, CO_2 and carbon emissions, the latter likely being fragments of CO_2, suggesting degradation of the triazine backbones. Ultimately, from 600 °C to 750 °C,

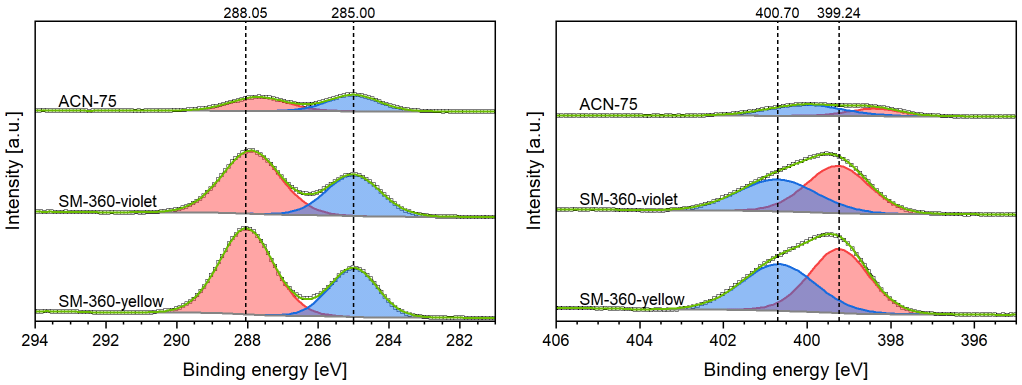

Figure 4.6.: Deconvoluted XPS results, left images shows C 1s peaks assigned to C-C (blue) and N-C=N (red), right one N 1s peaks assigned to C-N=C (red) and N=N (blue); the survey spectra are shown in Figure S9.

the remaining triazine backbones are completely combusted. The main distinction between ACN-75 and SM-360-samples is the lack of the initial decomposition stage between 200 °C and 330 °C for SM-360-samples. In this region, NH_3 and NO are predominantly released, likely from oxidized end groups.

X-ray photoelectron spectroscopy (XPS) gives valuable insights into structural composition with a great level of detail. The experimental measurements have been fitted and the chemical shift was corrected by calibrating the C-C peak (blue) to 285 eV. In an ideally constructed azo-bridged triazine structure, a one to one ratio of pyridinic nitrogen, from the aromatic triazine, and the azo nitrogen should be observable. In fact, the experimental data for N1s can be decomposed into two peaks, as shown in Figure 4.6. For SM-360-yellow, nitrogen peaks at 399.23 eV, corresponding to sp-bonded nitrogen in C–N=C (red), and 400.68 eV for azo -N=N- (or -NH-NH-) (blue) have a ratio of 52.4 % to 47.6 % [153]. For SM-360-violet, the picture is rather similar, with peaks at 399.27 eV and 400.74 eV and a ratio of 54.1 % to 45.9 %, almost matching the ideal 1:1 ratio.

ACN-75 gives different results, with shifted peak positions and ratios. The peaks are located at 398.39 eV and 400.06 eV, with 31.9 % to 68.1 %. This increase in the azo/amine peak indicates a larger fraction of terminal groups, aligned well with the smaller crystallinity observed from XRD and the chemical features observed by FTIR measurements.

The recorded C1s XPS spectra in Figure 4.6 show two distinct peaks. For carbon

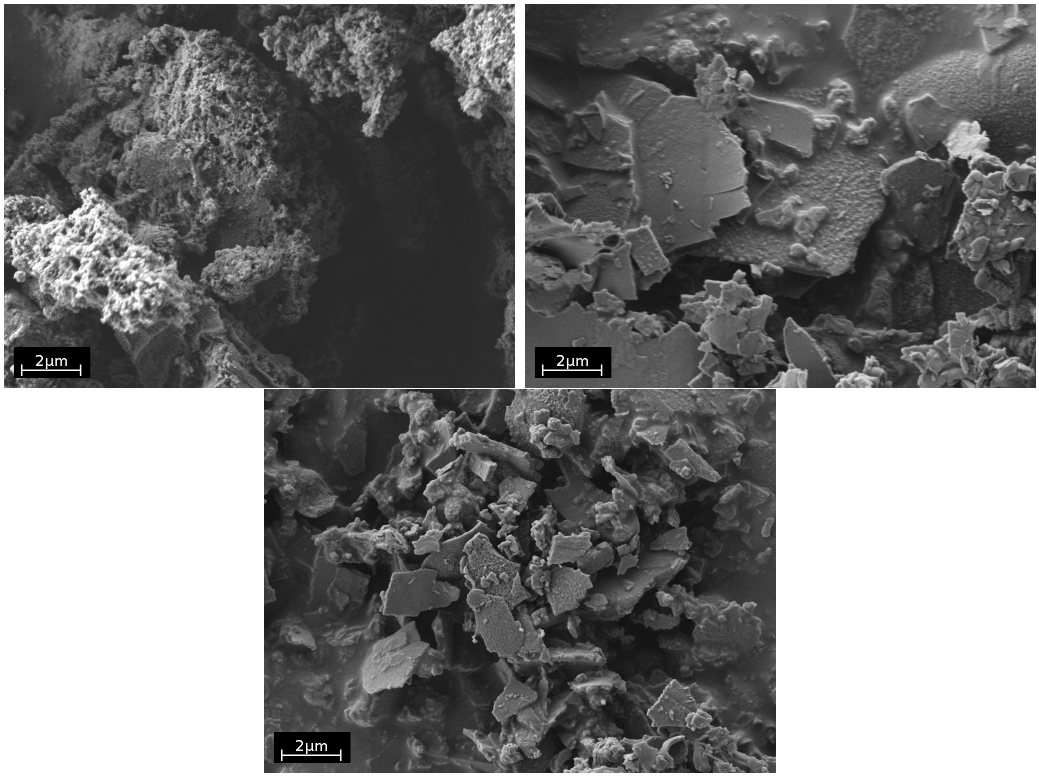

Figure 4.7.: SEM Figure of ACN-75 (top left), SM-360-yellow (top right) and SEM-360-violet (bottom) with 6.83 kx magnification.

nitride materials, a C-C (blue) peak is commonly observed and is referred to as adventitious carbon, which adsorbs on the surface of our material during transport and air contact [154, 155, 156]. The -N-C=N- carbon peak (red) from triazine can be found around 288 eV, exactly at 288.03 eV for SM-360-yellow, at 287.76 eV for SM-360-violet, and at 287.68 eV for ACN-75. The small variations are again caused by a slightly different atomic environment.

SEM images in Figure 4.7 display the surface morphology of ACN-75, SM-360-yellow, and SM-360-violet. The ACN-75 sample exhibits a porous surface with large agglomerates. It appears rough and uneven, indicating a heterogeneous texture with significant void spaces and possible open channels. In contrast, SM-360 materials reveal platelets of different sizes and rather smooth surfaces. This plate-like morphology resembles a two-dimensional material well. The observations of porous and smooth surface agree well with the measured surface area of 38 $\frac{m^2}{g}$ for ACN-75 and 8 $\frac{m^2}{g}$ for SM-360-yellow.

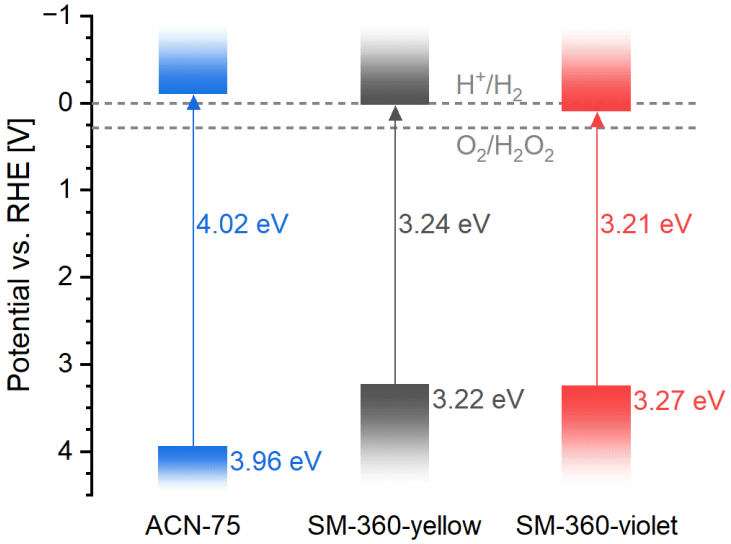

Figure 4.8.: Direct band gap and band-edge potential (vs. RHE) for bulk-CN (g-C_3N_4), ACN-75, and SM-360-yellow.

The suitability of our materials for solar-driven chemical processes was evaluated by measuring their direct optical band gap via UV–Vis spectroscopy, as depicted in Figure 4.8, and determining their conduction-band edges through Mott–Schottky analysis. The direct band gaps range from 3.2 to 4.0 eV, which is considerably larger compared to other carbon nitrides such as K-PHI or g-C_3N_4, which have typical band gaps around 2.7 eV [134]. The obvious reason for the large difference between ACN-75 and SM-360-samples is the aforementioned different particle size, which coincides with large aromatic systems for SM-360-samples and therefore decreases the band gap.

The corresponding indirect band gaps, which are not displayed, are approximately 0.3 to 0.5 eV smaller, indicating more permissible transitions in these layered structures.

Subsequently, we investigated photocatalytic H_2O_2 production under visible, blue light irradiation in an O_2-saturated aqueous suspension. As presented in Figure 4.9, bulk-CN, which is graphitic C_3N_4, achieves a performance three times higher than ACN-75, and SM-360-yellow just barely shows any activity. However, stability of all samples is robust and offers a promising framework for further enhancements, for example, through co-catalyst integration, metal ion doping, or by enlarging the surface area via exfoliation techniques. Enhancements with metal ions can prolong the lifetime of excited states, reduce recombination, and increase product yield. In

addition, enhancing surface area via exfoliating the two-dimensional layers can increase contact area with the reagent and thus reactivity.

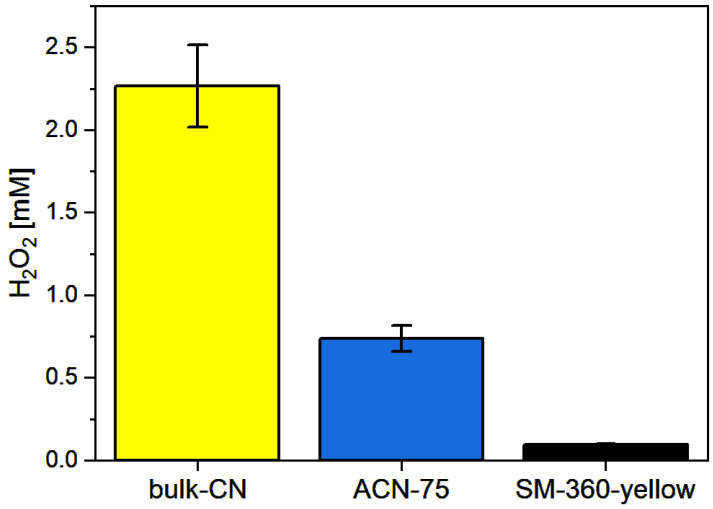

Figure 4.9.: Photocatalytic produced H_2O_2 accumulating in 1 h under blue-light irridiation (460 nm).

Figure S14 in the Supplementary Information presents the cyclic voltammetry (CV) and electrochemical impedance spectroscopy (EIS) plots of the investigated samples, measured in an aqueous Zn^{2+} containing electrolyte within a potential window of 0–2 V vs. Zn/Zn^{2+}. These electrochemical measurements were performed to assess the suitability of the materials for zinc-based energy storage applications, such as batteries or supercapacitors.

All CV profiles exhibit two pronounced redox peaks centered near 0 V and 2 V, which are attributed to the reversible Zn^{2+} ion insertion (reduction) and subsequent extraction (oxidation) at redox-active sites within the material. Specifically, the cathodic peak at 0 V corresponds to Zn^{2+} uptake, while the anodic peak near 2 V is associated with the stripping of Zn. In particular, samples synthesized via the salt-melt route display an additional redox couple with cathodic and anodic features at approximately 1.1 V and 1.2 V, respectively. This secondary process may be linked to alternative Zn^{2+} coordination environments or a reversible transformation of azo (–N=N–) to hydrazo (–NH–NH–) linkages. However, further analysis is needed to elucidate the underlying mechanism.

The CV curves deviate from the ideal rectangular shape characteristic of electric

double-layer capacitors (EDLCs), indicating that the charge storage behavior is predominantly faradaic in nature, with contributions from pseudocapacitive processes. This suggests that Zn^{2+} ions are not stored solely via electrostatic adsorption, but rather through interactions with nitrogen-rich coordination sites embedded in the organic framework. These observations underscore the critical role of nitrogen doping and the structural features of the triazine-based backbone in facilitating reversible redox activity.

Compared to SM samples, ACN-75 exhibits significantly higher overall impedance, indicative of limited ion diffusion and lower electronic conductivity. Combined with the persistence of well-defined redox peaks over multiple cycles, demonstrated up to the fourth cycle, this supports the favorable electrochemical reversibility and structural stability of these materials under operational conditions.

4.4. Conclusion

With the results presented above, we were able to demonstrate that azo-bridged triazine structures with CN_2 / C_3N_6 stoichiometries can be synthesized via two different, yet straightforward and scalable approaches. The resulting materials were thoroughly characterized using sophisticated analytical techniques, confirming the successful incorporation of azo linkages and the formation of extended conjugated frameworks. Although the photocatalytic activity for H_2O_2 production of these bulk samples currently falls short of outperforming well-established benchmark materials, and the electrochemical performance in the presence of Zn^{2+} ions also requires further optimization, the intrinsic activity of this new system is promising. These findings provide a solid foundation for future development and refinement. In particular, metal doping emerges as a highly promising strategy to enhance charge separation, facilitate redox reactions, and strengthen interactions with adsorbed reactants. Tailoring the electronic structure through dopant incorporation may significantly improve photocatalytic and electrochemical efficiency. Beyond these applications, new directions for material utilization, such as in gas separation, selective adsorption, or as membranes in electrochemical devices, can be explored. The porous and chemically versatile nature of the synthesized frameworks makes them attractive candidates for molecular sieving or CO_2 capture. Furthermore, azo-bridged link-

ages may offer unique opportunities for post-synthetic modification, enabling the introduction of functional groups or active sites tailored to specific applications.

5. Adsorption of H^+ and NH_4^+ in Na- and H-PHI

This chapter is based on the collaborative work with the research group of Dr. Oleksandr Savateev, from the Max Planck Institute of Colloids and Interfaces, published in Nature Communications with the title *"Extent of carbon nitride photocharging controls energetics of hydrogen transfer in photochemical cascade processes"* [123]. Although the publication combines experimental and computational approaches, this chapter focuses on the simulations and theoretical calculations conducted, as this reflects my contribution to the publication. However, a brief introduction to the topic and the experimental research conducted will be provided.

5.1. Introduction

Experiments demonstrated that the extent of photocharging in PHI significantly impacts its photocatalytic performance, particularly in the here studied case of the tetramerization of benzylamine. Higher catalyst loadings and elevated temperatures were observed to improve product yields, which suggests a link between electron/proton storage, or photocharge density, and the adsorption/desorption mechanics. But the molecular origin of this behavior remains unclear and can not be explained by experiments alone. In order to address these questions, DFT calculations were performed to obtain periodic model systems of Na-PHI and H-PHI with varying unit cell sizes. These models were then used for simulations to quantify the charge distribution, identify preferred adsorption sites, and evaluate the adsorption energies for H^+ and NH_4^+. Additionally, solvation effects were studied. By connecting all these results with the experimentally observed trends, the simulations help to explain the mechanism of adsorption and the role of photocharge density.

5.2. Computational details

Density functional theory calculations were conducted using the Gaussian and plane wave approach [143] as implemented in the CP2K suite of programs [142]. If not specified otherwise, all simulations used periodic boundary conditions and a plane wave cutoff of 500 Ry to represent the electron density, whereas the Kohn-Sham orbitals were described by a molecularly optimized double-zeta Gaussian basis set [157]. The Becke-based B97-3c exchange and correlation functional was employed in conjunction with an empirical dispersion correction to account for long-range van der Waals interactions [37]. Net atomic charges were quantified by means of the DDEC6 method [45].

5.3. Creating Model Systems

In order to gain a better understanding of the experimental results and extract further details from the simulations, it is necessary to create an accurate model of the system. To estimate differences and the influence of the photocharging/adsorption states, we created different H-PHI and Na-PHI systems, bearing either hydrogen or sodium as counterions, and varying in size of the periodic cell, ranging from two heptazine subunits to four, eight, and twenty. By introducing an equivalent amount of H^+ and NH_4^+ into these systems of different sizes, we model different concentrations of photocharged states. Structures for Na-PHI and H-PHI are derived from those published by Sahoo et al. [158] by geometrical optimization of cell and structure properties without constraints with respect to cell shape or atomic positions. By doing so, the strict AA-stacking pattern, which was observed in the source, breaks, and the sodium counterions move toward their energetical optimum in the pores within the g-CN layer. Given that the behavior of H-PHI in the experiment with benzylamine is similar to that of mpg-CN, and its crystal structure was reported [159], we also modeled this material, and depicted it in Figure 5.1. However, temperature and solvent effects are not included in the models due to the high complexity and computational costs, apart from a study regarding the solvation of Na^+ at the end of this chapter.

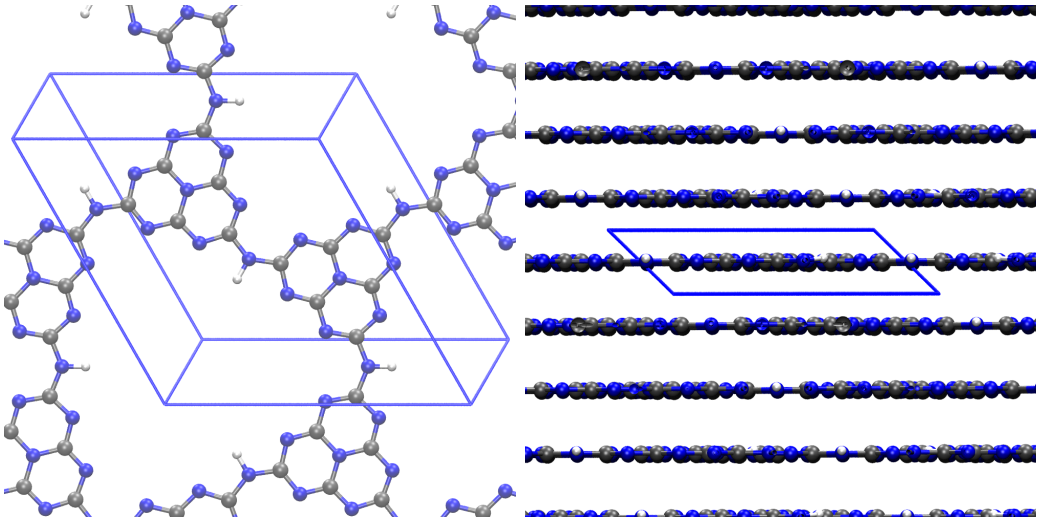

(a) H-PHI view from the top.

(b) H-PHI layers.

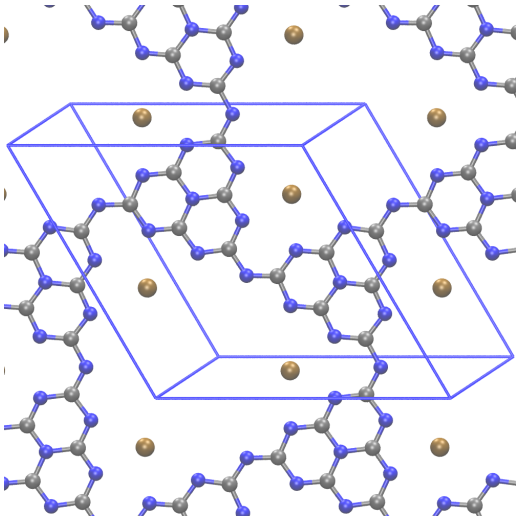

(c) Na-PHI view from the top.

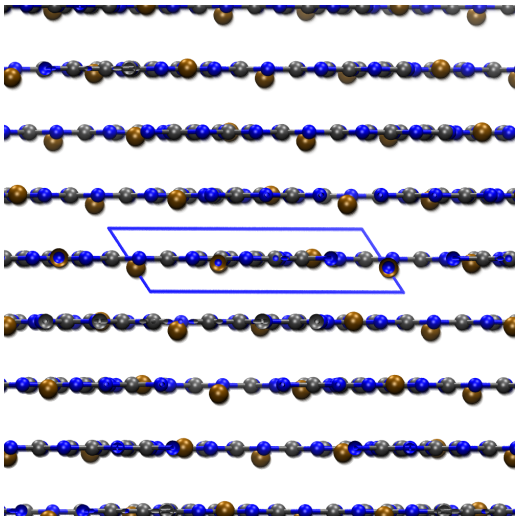

(d) Na-PHI layers.

Figure 5.1.: Depiction of the model structures with the cell borders. Sodium ions are ochre colored and tend to be within the CN-layers.

5.4. Charge distribution

Before investigating the energetical adsorption properties of H^+ and NH_4^+ in the systems, a closer look at the atomic charges gives valuable insights, as their influence on all the adsorption properties studied is crucial. Net atomic charges were obtained using DDEC6 as implemented in Chargemol, with cube files calculated via CP2K as described above, although an increased cutoff of 1000 Ry was used. This is necessary for an appropriate assignment of the electrons. Tables 5.2 and 5.1 give the arithmetic average elementary charge for all atoms of each element in the Na-PHI structures, while hydrogen or ammonia is adsorbed. The standard deviations are also listed there, if applicable. In general, the charges of the elements are around -0.54 e for nitrogen and 0.53 e for carbon, but they only marginally vary with changing system size. There is a slight increase in the positive charge observed by approximately 0.02 e for carbon and 0.01 e for sodium by enlarging the number of heptazine units from two to twenty.

	Nitrogen	Carbon	Sodium	$N_{ads.-site}$	H
2-Na-PHI	-0.54 ±0.13	0.52 ±0.03	0.88 ±0.01	-0.39	0.31
4-Na-PHI	-0.54 ±0.12	0.53 ±0.03	0.88 ±0.01	-0.39	0.32
8-Na-PHI	-0.54 ±0.12	0.53 ±0.03	0.89 ±0.01	-0.39	0.32
20-Na-PHI	-0.54 ±0.12	0.54 ±0.03	0.89 ±0.01	-0.39	0.32

Table 5.1.: Variation of charges while hydrogen is adsorbed on Na-PHI with values in units of elementary charge [e].

	Nitrogen	Carbon	Sodium	$N_{ads.-site}$	$N(NH_4^+)$
2-Na-PHI	-0.54 ±0.13	0.52 ±0.02	0.87 ±0.02	-0.38	-0.90
4-Na-PHI	-0.54 ±0.12	0.53 ±0.03	0.88 ±0.01	-0.38	-0.90
8-Na-PHI	-0.54 ±0.12	0.53 ±0.03	0.89 ±0.01	-0.39	-0.86
20-Na-PHI	-0.54 ±0.12	0.54 ±0.03	0.89 ±0.01	-0.39	-0.88

Table 5.2.: Variation of charges while ammonium is adsorbed on Na-PHI, all values are in units of [e].

Similar trends are also observable for H-PHI, tabulated in 5.3 and 5.4. Changes

of about 0.02 e occur for all listed elements. However, it should be noted that there are differences in electrons accumulated in nitrogen of about 0.1 e between Na-PHI and H-PHI. This number exactly accounts for the variation of the electron-donating abilities of hydrogen and sodium. Since there are three hydrogen/sodium atoms per unit cell, as well as 17 nitrogen atoms, and there is a distinction of approximately 0.56 e between the two electron donors, this yields 0.09 e additional charge per nitrogen atom donated in Na-PHI. As already stated, the charge has a tremendous effect on the material properties, and the behavior of the counterions is one way to influence these.

	Nitrogen	Carbon	Hydrogen
2-H-PHI	-0.45 ±0.08	0.52 ±0.03	0.32 ±0.01
4-H-PHI	-0.44 ±0.08	0.53 ±0.03	0.32 ±0.01
8-H-PHI	-0.44 ±0.08	0.53 ±0.02	0.32 ±0.01
20-H-PHI	-0.44 ±0.08	0.54 ±0.02	0.32 ±0.01

Table 5.3.: Variation of charges while hydrogen is adsorbed on H-PHI, all values in units of elementary charge [e].

	Nitrogen	Carbon	Hydrogen
2-H-PHI	-0.46 ±0.09	0.52 ±0.03	0.31 ±0.02
4-H-PHI	-0.45 ±0.09	0.53 ±0.02	0.31 ±0.02
8-H-PHI	-0.44 ±0.09	0.54 ±0.02	0.32 ±0.01
20-H-PHI	-0.44 ±0.08	0.54 ±0.02	0.32 ±0.01

Table 5.4.: Variation of charges while ammonium is adsorbed on H-PHI, all values in units of elementary charge [e].

However, the tables shown above do not indicate the accumulation of charge on individual atoms of an element, which requires a closer look at the charge distribution, which can be found in Table 5.5. The assignment of labels to specific atoms in PHI is given in Figure 5.2. In general, the nitrogen atoms on the outer part of the heptazine imide, N3 and N2, cumulate most of the negative charge, while N1, which has three atoms to covalently bond with and therefore no lone pair, is less charged. N4, which acts as the bridging atom between heptazine imide units and is

typically the binding partner for any reactive species, accumulates just slightly less electrons than N3 and N2. In the case of solvated Na-PHI, which will be examined in further detail later, the charges are lower because the sodium-nitrogen distances are larger, due to the solvation shell, and therefore charge-transfer between PHI and the ion is inhibited. The overall trends described are identical for Na- and H-PHI, although N4 in H-PHI has slightly less electron density. Implications regarding the reactivity and adsorption properties of the material that result from these charges are presented in the next section.

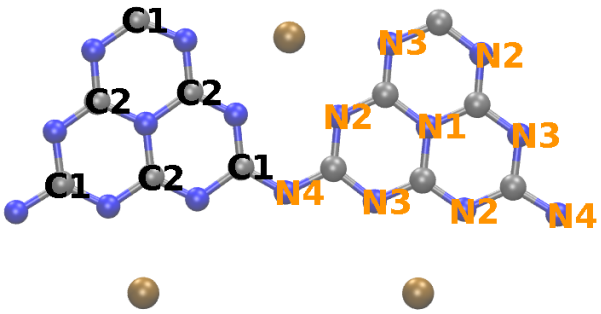

Figure 5.2.: Labeling of individual atoms in the heptazine imide unit to assign the charges in Table 5.5.

	Na-PHI	H-PHI	Na-PHI$_{solvated}$
N1	-0.215 ±0.001	-0.257 ±0.005	-0.231 ±0.014
N2	-0.592 ±0.017	-0.507 ±0.020	-0.526 ±0.044
N3	-0.584 ±0.033	-0.479 ±0.017	-0.519 ±0.023
N4	-0.547 ±0.017	-0.370 ±0.003	-0.485 ±0.056
C1	0.562 ±0.023	0.552 ±0.017	0.568 ±0.036
C2	0.512 ±0.008	0.529 ±0.018	0.539 ±0.016
Na	0.885 ±0.010	-	0.911 ±0.012

Table 5.5.: Mean charges with standard deviation, charges are calculated for PHI systems with 20 subunits. The numbers are mostly identical in smaller systems, with deviations below 0.02 e compared to 2 heptazine PHIs.

5.5. Adsorption energies for H^+ and NH_4^+ in Na- and H-PHI

To model excitation states of the two structures with static DFT, hydrogen and ammonium radicals were introduced, and adsorption energies were calculated. To initially identify preferential facets for adsorption, a case study for hydrogen was conducted. Therefore, the interaction of a hydrogen radical at three different positions, depicted in Figure 5.3, on periodic systems with two subunits was investigated. Table 5.6 lists these adsorption energies. In the case of Na-PHI, positions 2 and 3 are sterically competing with sodium ions, which are preferentially placed in the corners of the pore, leading to very unlikely endothermic adsorption energies. For H-PHI, beneficial interactions with nitrogen from neighboring heptazine, and the proximity of another hydrogen at position 2 can explain the adsorption energies for positions 3 and 2. Additionally, the effect of charge differences between these nitrogen atoms leads to divergent coulombic interactions; compare to Table 5.5.

	Position 1	Position 2	Position 3
H_{ads}(H-PHI)	-	18.95	-15.63
H_{ads}(Na-PHI)	-10.24	87.17	33.58

Table 5.6.: Adsorption energies for Hydrogen in $\frac{kJ}{mol}$.

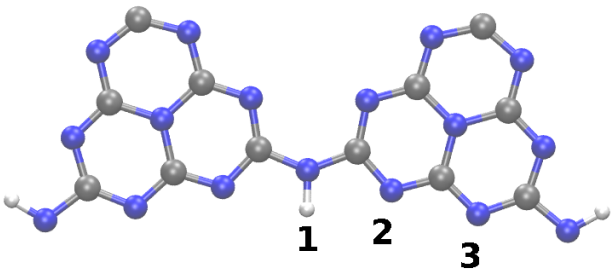

Figure 5.3.: Three in-layer preferential adsorption sites, adsorbates interact with the lone-pair of trigonal-planar nitrogen.

The adsorption energy H_{ads} is calculated by subtracting the total energy of the PHI system and half of the total energy of a gas-phase hydrogen molecule (in vacuum) from the PHI system with adsorbed hydrogen, as described in Equation5.1.

$$H_{ads} = E(PHI + H) - E(PHI) - \frac{1}{2}E(H_2) \tag{5.1}$$

Note that E is a potential energy and therefore has a negative sign, which yields negative adsorption energies for an exothermic process, while positive adsorption energies refer to an endothermic process. The desorption energies are equivalent to these values but with an opposing sign.

Due to the limited pore size, steric effects become more important regarding the adsorption of ammonium, which reduces the amount of potential adsorption sites. These are displayed in Figure 5.4 for H-PHI and Na-PHI. The first and foremost observation from the figure is that Na-PHI breaks NH_4^+ into NH_3 and a covalently bonded hydrogen, while no bond breaking occurs when NH_4^+ is adsorbed on H-PHI. This behavior is identical for all systems studied, regardless of the density of e^- per heptazine. Since H_{ads}, which is calculated for this case by adding a potential energy term for ammonia, –E(NH_3), to Equation5.1, only differs slightly between H- and Na-PHI (Figure 5.4), the divergent adsorbing behavior may, among other explanations, possibly be accountable for the divergent catalytic behavior

observed in the experiments. As mentioned above, adsorption energies of H^+ and

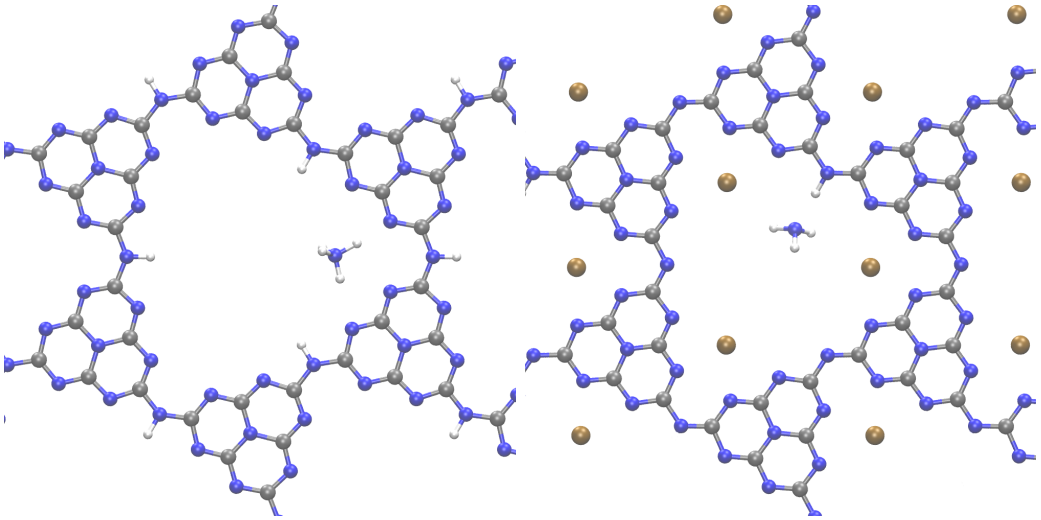

(a) Ammonium adsorbed on H-PHI. (b) Ammonium adsorbed on Na-PHI.

Figure 5.4.: Adsorption of ammonium on H- and Na-PHI. In the latter, it fissures, leading to H^+ bonded to Na-PHI and NH_3 adsorbed.

NH_4^+ were calculated for a varying number of heptazine units to investigate the influence of e^- charge density, which experimentally corresponds to the mass of added g-CNs to the reaction mixture. The results are plotted in Figure 5.5. A clear trend toward decreasing adsorption energy magnitude with increasing system size is observable, and hydrogen adsorption even becomes endothermic in systems containing more than four heptazine units. A possible explanation for this trend is the better delocalization of electrons within structures with enlarged π-systems. As adsorption energies decrease, so do desorption energies increase, which decreases the amount of energy necessary to recover g-CN by desorbing e^-/H^+ (or e^-/NH_4^+). The results of the DFT modeling indicate that the enthalpy of adsorption for both H^+ and NH_4^+ depends on the degree of material charging. In strongly reduced in H-PHI and Na-PHI with up to 1 e^-/1 H^+ (or 1 e^-/1 NH_4^+) per two units of heptazine the adsorption energy is exothermic, $H_{ads} < 0$. In other words, the desorption of e^-/H^+ (or e^-/NH_4^+) from such photocharged PHIs is an endothermic process. On the other hand, mildly-reduced PHIs with only 1 e^-/1 H^+ per 20 heptazine units the desorption of e^-/H^+ is exothermic, as $H_{ads} > 0$. Moreover, regardless of the degree of photocharging, the desorption of e^-/NH_4^+ is always uphill. In the experimental context of the benzylamine tetramerization cascade process, these results agree with

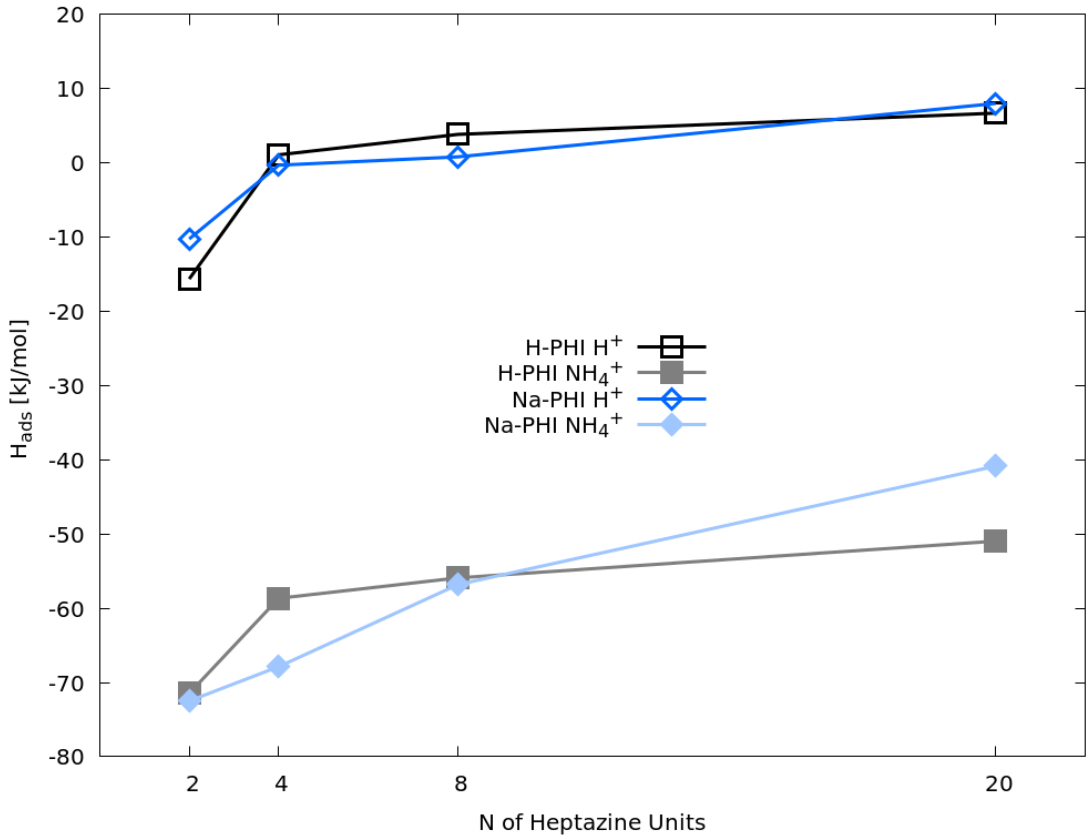

Figure 5.5.: Adsorption energies of hydrogen and ammonium in Na-PHI and H-PHI with respect to the number of heptazine units. H_{ads}<0 means that adsorption is a spontaneous process, while desorption is endothermic.

the experiment in two aspects. First, higher yields are observed when the reaction is conducted at elevated temperatures, compared to room temperature, as heating is required to overcome the energy barrier of proton-coupled electron transfer (PCET), due to the endothermic desorption, from photocharged H-PHI (e^-/H^+).
And secondly, higher yields are obtained when the reaction is conducted using a greater mass of g-CNs. Under such conditions, materials are photocharged to a lesser extent, resulting in $H_{ads} > 0$, and weak binding of e^-/H^+ by g-CN.

5.6. Solvent effects

We solvated every Na^+ with five water molecules [160, 161] and optimized the resulting structure to study the basic effects of solvation. A snapshot of the solvated system can be seen in Figure 5.6. As expected, the average distance between sodium ions and the CN-Backbone increases when water is added, see Table 5.7, since water molecules form a solvation shell around the ion, leading to a shift toward the center of the pore. This shift can be traced best with the Na-N3 distance, however, the actual values are highly dependent on the position and orientation of the explicit solvent, creating a large standard deviation σ.

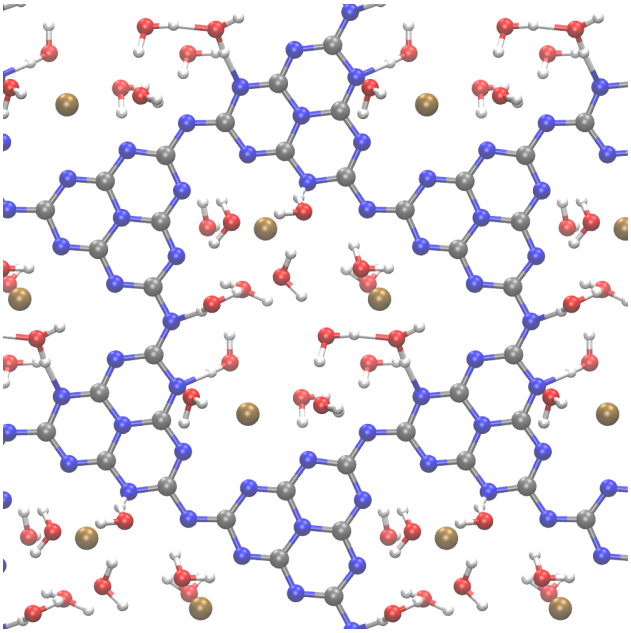

Figure 5.6.: Single layer of Na-PHI solvated by five water molecules per sodium ion. The interlayer distance, compared to non-solvated structure, is increased.

	average distance [Å]	σ
Na-N2	2.64	0.096
Na-N2 (with water)	2.85	0.552
Na-N3	2.41	0.080
Na-N3 (with water)	3.12	0.556

Table 5.7.: Distance Na-Backbone, labels derived from Figure 5.2.

The adsorption energies of H^+/NH_4^+ in the system, which are shown in the Table 5.8, were additionally studied. The effect of the solvent is significant, although there is no noticeable trend with respect to the system size or the concentration of photocharged states. Although the released adsorption energy of the small hydrogen atom increases as a result of the hydrogen bonds formed with the solvent, it decreases in the case of ammonium. Ammonium also benefits energetically from interactions with the solvent, but is sterically hindered. All of these interactions are strongly influenced by small differences in the orientation and position of the molecules, which result from geometric optimization of the system. However, the addition of multiple solvent molecules increases the number of degrees of freedom, making it challenging to find a global minimum. Therefore, there is no guarantee that the adsorption energy listed actually represents an optimal value. As a consequence, these energies resemble a snapshot strongly dependent on the current solvent configuration and less influenced by the e^- density within the PHI material. The solvation of sodium ions in this way disguises their interaction with the PHI material.

	$E_{Ads}(H^+)$ $\frac{kJ}{mol}$	$E_{Ads}(NH_4^+)$ $\frac{kJ}{mol}$
2-Na-PHI	-32.29	117.42
4-Na-PHI	-69.30	63.78
8-Na-PHI	-65.54	-24.40
20-Na-PHI	0.62	117.56

Table 5.8.: Adsorption energies in solvated Na-PHI (five water solvation shell per sodium) in $\frac{kJ}{mol}$.

As mentioned above, the influence of the solvent on the charges should also be considered, as listed in Table 5.5. In general, the effect on the charges is rather small and not of a qualitative nature, but for the outer nitrogen atoms, N2, N3, and N4, the NACs are reduced by 0.06 e. This is due to the higher sodium backbone distance and, therefore, lower charge transfer, which can only be partially compensated by the interaction of these nitrogen atoms with the newly introduced water molecules.

6. Influence of Terminal Groups for Donor-Acceptor Carbonnitrides

The research work presented in the following pages is the result of a cooperation with the experimental group of Dr. Christian Mark Pelicano at MPIKG Potsdam. It is taken from a submitted, but not yet published paper labeled *"Triazole ring functionalized poly(heptazine imide): Leveraging donor-acceptor configuration toward enhanced solar-driven H_2O_2 synthesis"* with Sue-Faye Ng as first author. I allowed myself to merge parts of the paper with those from the supporting information and modify both, but the work presented here is restricted to my theoretical investigations. Further details on the experimental work can be found in the paper.

6.1. Introduction

Photocatalytic hydrogen peroxide production presents a sustainable alternative to conventional methods, which are largely based on the anthraquinone process, require noble metals and are not eco-friendly, as the anthraquinone process produces large amounts of waste [162]. Carbon nitride-based photocatalysts, such as poly(heptazine imide), have emerged as promising candidates due to their stability, versatility, and enhanced light absorption [163, 164, 165].

Recent advances suggest that modification of the terminal functional groups of PHI can influence its electronic properties, prolong the charge carrier lifetimes, and improve oxygen adsorption, ultimately enhancing photocatalytic performance [166, 167]. This study explores PHI functionalized with triazole groups, synthesized through a molten salt-assisted process, which exhibits superior H_2O_2 production efficiency compared to conventional terminated analogs. However, a detailed understanding of the underlying electronic effects remains limited and DFT simulations

are used to investigate the impact of terminal groups on charge distribution and O_2 adsorption. By constructing molecular models with defined terminal functionalities, we quantified net atomic charges and adsorption energies to elucidate the donor-acceptor interactions governing photocatalytic activity. Our findings provide key insights into the role of terminal group modifications in optimizing PHI-based catalysts for solar-driven H_2O_2 production.

6.2. Method and Model

To computationally investigate atomic charges and adsorption behavior at the atomic level, two model systems were constructed. These models consist of six heptazines arranged to form a pore, featuring a higher proportion of terminal groups compared to a more condensed system. Although this approach does not directly account for the effects of enhanced crystallinity observed in the experimental measurements, it allows us to focus on the critical role of terminal groups in shaping the electronic structure of the heptazine units. In a fully or mostly crystalline model, the influence of terminal groups is challenging to isolate and analyze. Using molecular models, we can better understand the localized electronic behavior and the donor-acceptor interactions that are crucial for the catalytic activity. The terminal groups studied here are triazoles, which are compared to simple amines, commonly found as terminal groups in polymeric carbon nitride compounds [122, 168]. The model systems were prepared using Avogadro [169]. To prevent triazole units from rotating around single-bond axes, the conformational space was sampled using semi-empirical methods and the global geometry optimization and ensemble generator (GOAT) based on the self-consistent tight-binding method GFN2-xTB [170], as implemented in ORCA 6.0 [171]. This was followed by a geometry optimization using a higher level of theory using the meta-GGa r2scan-3c functional [172]. The global minimum structures are depicted in Figure 6.1. An overview of all other conformers can be found in the supporting video of the paper, labeled *Conformer-exploration.mpg*.

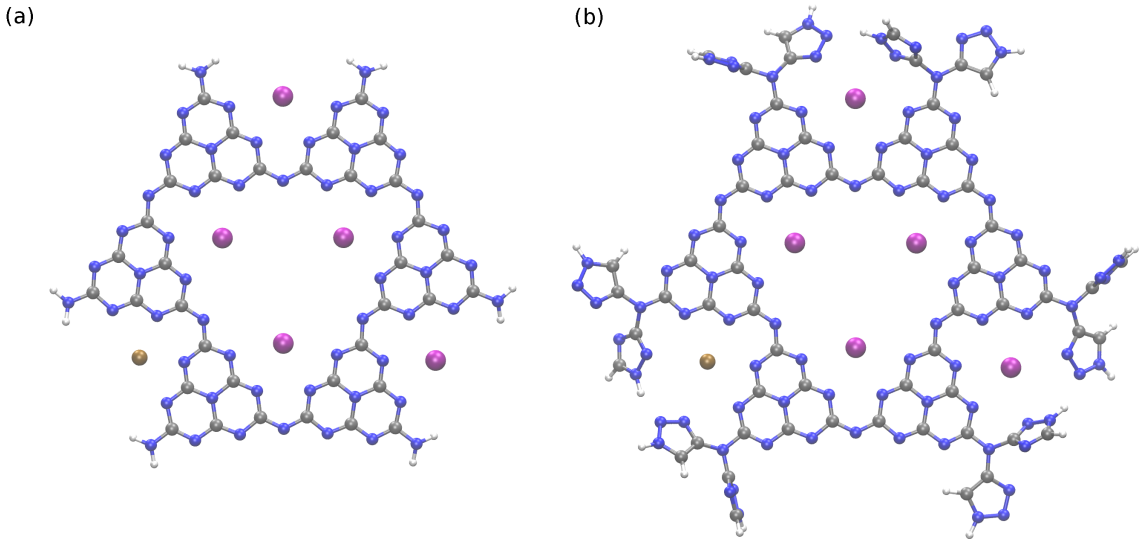

Figure 6.1.: Structures of KNa-PHI systems with terminal (a) amine and (b) triazole units (purple atom: potassium; ochre atom: sodium).

6.3. Net atomic charges

To quantify the donor-acceptor effect of the terminal groups on the heptazine backbone, we compared the net atomic charges between the two structures. NACs were calculated using the DDEC6 method [173], while the electron density was computed using the CP2K suite of programs [142]. Table 6.1 lists the average NACs for several atoms in the heptazine units, separated by their position, if applicable. For KNa-PHI systems terminated with amines, the charges are comparable to those reported for similar compounds [123]. In systems terminated with triazoles, the average charges are slightly reduced by 0.02 e for overall nitrogen (N-heptazine) and 0.01 e for overall carbon (C-heptazine) compared to systems terminated with amines. Although these changes in charge may seem small, they significantly affect the interaction of KNa-PHI with catalytic and adsorptive materials. This shift in electron density reflects the donor-acceptor effect mentioned earlier and contributes to the enhanced photocatalytic performance of these systems.

If we take a more detailed look at the charge distribution between the elements and those elements which differ in position, we have to highlight the decrease of negative charge on the outer nitrogens for the triazole-terminated model compared to the amine-terminated one. Although these nitrogens are numerically more present than others, they, in addition to the bridging nitrogen, also shape the interaction

	KNa-PHI-Amine	σ	KNa-PHI-Triazole	σ
N-bridging	-0.53	0.03	-0.53	0.03
N-core	-0.22	0.01	–0.23	0.00
N-out	-0.58	0.05	-0.56	0.04
N-heptazine	-0.53	0.13	-0.51	0.11
C-heptazine	0.56	0.04	0.55	0.03
C-terminating group	-	-	0.16	0.19
N-terminating group	-0.60	0.16	-0.21	0.11
H-terminating group	0.33	0.01	0.21	0.08
Sodium	0.86	0.00	0.88	0.00
Potassium	0.84	0.01	0.84	0.00

Table 6.1.: Mean net atomic charges (in units of elemental charge [e]) for nitrogen and carbon atoms in heptazine, with standard deviations (σ). The designations for nitrogen atoms are as follows: N-core refers to the central nitrogen of each heptazine unit, N-bridging denotes the nitrogen that connects heptazine units, and N-out refers to the remaining nitrogen atoms in the outer sphere. The averages for N- and C-heptazine encompass all these nitrogen atoms, while N-, H- and C-terminating averages are calculated based on the atoms present in the terminating groups.

with adsorbing atoms or molecules the most. A reduced negative charge of 0.02 e, induced by terminating triazole groups, which withdraw an overall higher portion of electron density compared to simple amines, also affects counterions. In this case, we additionally observe a reduction of electrons around the sodium, summing up to 0.02 e, leading to a higher coulomb attraction. The effects of this will become apparent in the next chapter.

6.4. Adsorption of O_2

The rate-determining step in the hydrogen peroxide synthesis pathway is the initial reduction of O_2 [174, 175]. A critical requirement for this electron transfer is the adsorption of O_2 onto the catalyst's surface. To investigate the adsorption behavior of O_2 and the influence of donor-acceptor groups, DOCKER within the ORCA 6.0 framework was utilized to explore various adsorption sites, which are displayed in Figure 6.2. Although many adsorption sites are shown, each of them was evaluated individually, with only one O_2 molecule adsorbing in KNa-PHI-triazole per calculation.

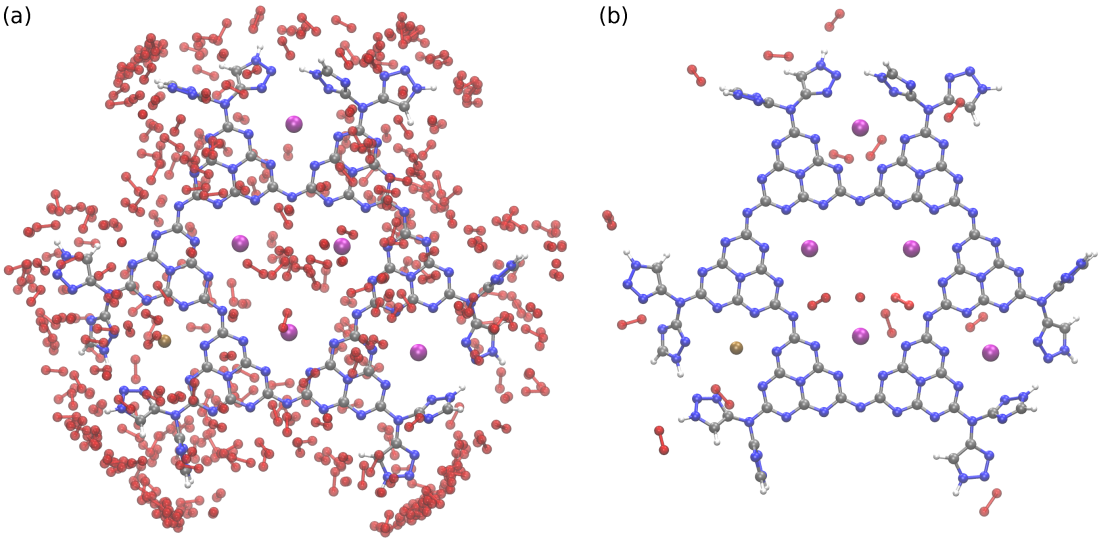

Figure 6.2.: (a) Initial particle swarm of O_2 molecules individually adsorbed onto KNa-PHI-triazole and (b) only those with $\Delta E_{ads} < 0.01$ Ha after optimization, compared to the most exothermic adsorbed molecule.

Figure 6.3 illustrates O_2 at its most energetically favorable adsorption site. The distance between O_2 and the nitrogen bridge is consistent between both systems at

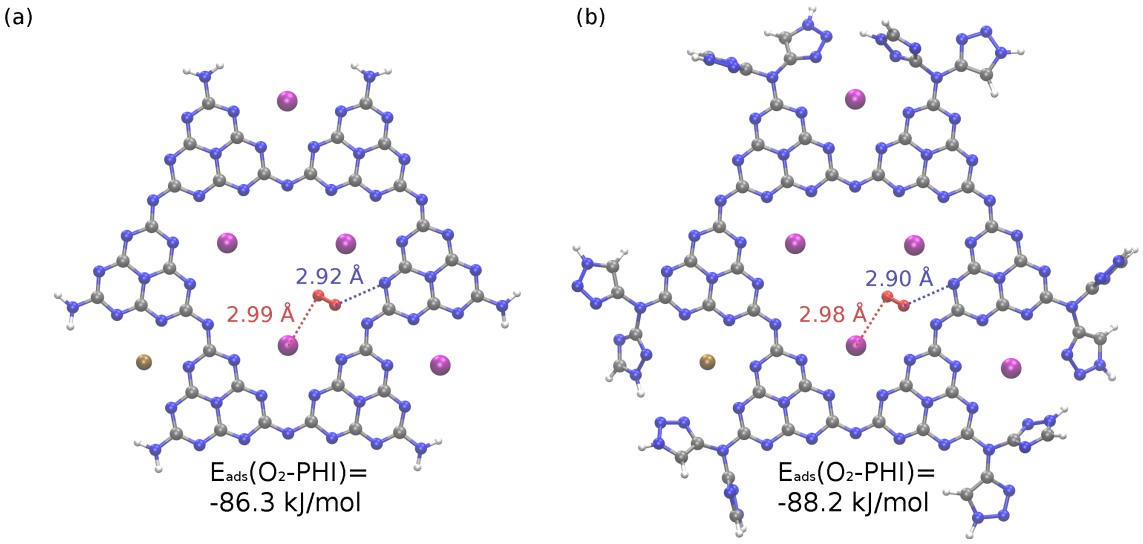

Figure 6.3.: Adsorption of O_2 onto the bridging nitrogen atoms of the model systems with terminal (a) amine and (b) triazole units, showing the differences in the adsorption behavior due to the influence of terminating groups.

2.07 Å, however, in triazole-terminated systems, the distance to the potassium ion and the second nearest nitrogen atom is slightly shorter, enhancing the interaction between the adsorbate and the adsorbent.

As indicated in Table 6.1, exactly the nitrogen atoms located in the outer sphere of the heptazine unit are the most affected by the charge change due to terminating groups, which makes the increased interaction of the gas with the material a result of the charge change induced by terminating groups. As lower adsorption energies indicate better adsorption, our findings reveal that the choice of terminating groups qualitatively accelerates the essential O_2 reduction step. Therefore, terminating groups can be used to tune catalytic performance and overall efficiency in H_2O_2 synthesis in heptazine structures.

7. Water in (Sub)Nanopores: Wettability of C_1N_1

This chapter is based on and partially copied from the collaborative work published in Angewandte Chemie with the title *"Understanding the Wettability of C_1N_1 (Sub)Nanopores: Implications for Porous Carbonaceous Electrodes"* [176]. The following pages will give a brief introduction to the topic and the experimental research conducted, but primarily deal with the accompanying simulations and theoretical calculations, which reflect my expertise and contribution to the publication. The interested reader may find additional information and modifications to the text compared with the passages in the paper, which aim to give further insights into the topic.

7.1. Introduction

Understanding how water interacts with nanopores of carbonaceous electrodes is crucial for energy storage and conversion applications. A high surface area of carbonaceous materials does not necessarily translate to a high electrolyte-solid interface area, which has a dominant influence on the capacitance and electrocatalytic performance of these devices [177]. Highly nitrogen-doped carbons are expected to feature pores with significantly increased hydrophilicity and thus wettability [178], which is crucial for a high solid-electrolyte surface, if the electrolyte is aqueous. However, in the case of (sub)nanometer cavities, the traditional concept of hydrophilic and hydrophobic surfaces can be misleading, as confined water can show different properties than bulk water [179]. In this work, the interaction of water with nanoporous C_1N_1 materials was studied to explain their low specific capacitance in aqueous electrolytes despite their high surface area and nitrogen content. Water

was used to probe chemical environments, provided by pores of different sizes, in ^{1}H MAS NMR experiments. For that purpose, three different materials were utilized. Two of these materials exhibited comparable surface areas, and two exhibited similar levels of nitrogen incorporation. It was observed that, regardless of their high hydrophilicity, only a negligible portion of water can enter the nanopores of C_1N_1, in contrast to a reference pure carbon material with a similar pore structure. The common paradigm that water easily enters hydrophilic pores does not apply to C_1N_1 nanopores below a few nanometers. Electronic structure calculations were used to investigate the different environments of water molecules seen in the NMR measurements of nanoporous C_1N_1 and to study the way water molecules are stabilized inside nanoporous cavities by determining their heat of adsorption.

7.2. Model System Development

All computations were performed using the CP2K Quickstep program package with three-dimensional periodic boundary conditions [142]. The model amorphous C_1N_1 structure employed for the calculation of the water adsorption energies and nucleus-independent chemical shifts was created via dynamical simulated annealing utilizing the second-generation Car-Parrinello method based on the extended tight-binding (xTB) model [180, 181]. For this purpose, a system consisting of 100 carbon and 100 nitrogen atoms was arranged within a cubic box with a volume of 2204 Å^3, corresponding to a density of 1.96 g/cm^3. The amorphous model was subsequently achieved by dynamically annealing the system from the melt at 3000 K to 900 K over 60 ps, using a discretized time step of 2 fs. Subsequently, the resultant structure was geometrically optimized at the DFT level using the Gaussian and plane wave approach [143]. Within this framework, the Kohn-Sham orbitals are characterized by a precisely molecularly optimized double-zeta basis set with an additional set of polarization functions [157], while the charge density is represented by a plane wave grid with a density cutoff of 500 Ry. Separable norm-conserving dual-space pseudopotentials were employed to replicate the interactions between the valence electrons and the nuclear cores [182]. The unknown exchange and correlation energy was approximated using the B97-D functional, supplemented by a damped pairwise London dispersion correction to adequately account for long-range van der

Waals forces [183]. The resulting structural model is an amorphous bulk system with several (sub)nanopores. Inspection of the annealed C_1N_1 structure, depicted in Figure 7.1, reveals a wide variety of rings, chains, and aromatic systems, thus making the structure an appropriate digital representative for different water adsorption sites. Figure 7.1 (b) shows the development of the potential energy with respect to time and is correlated to the according temperature of the system. It is obvious how the temperature is damped with increasing time and that the potential energy slowly converges. With temperature, the kinetic energy decreases, so the motion of the atoms becomes rather slow and structural changes less likely to occur, which is why the annealing is aborted after 60 ps.

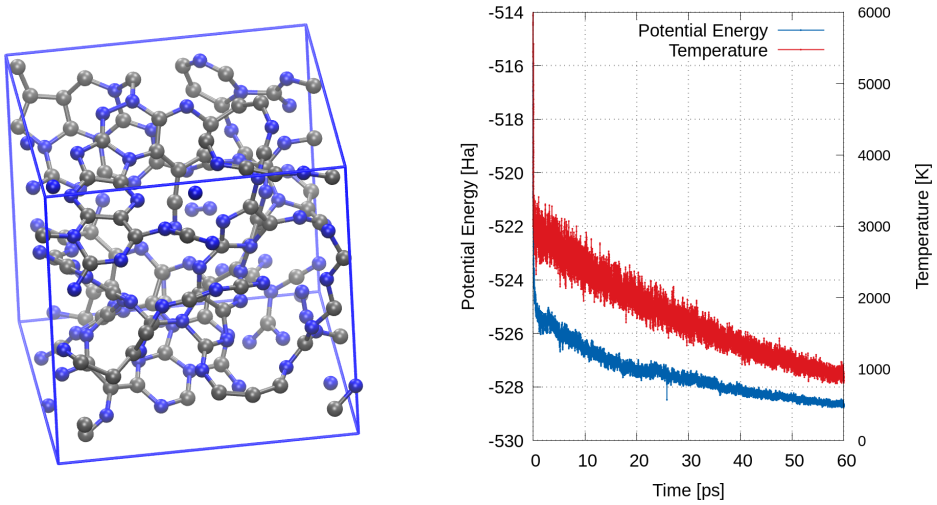

Figure 7.1.: (left image) Finalized model system with cell boundaries and (right image) energy and temperature values during the annealing process.

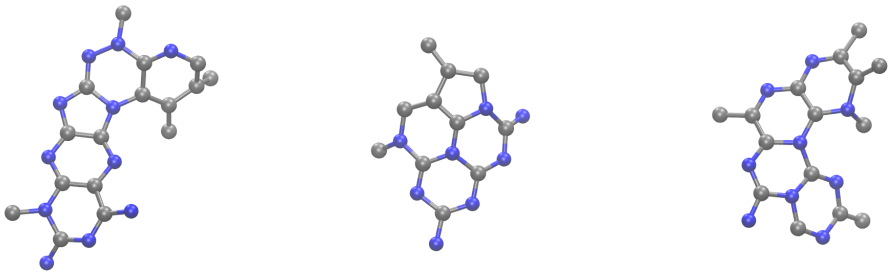

(a) (b) (c)

Figure 7.2.: (a-c) Depicting different structural motives of the system with a variety of ring systems, double bonds and aromatic compounds.

7.3. Results

7.3.1. Water Adsorption

To further study the interaction of the hydrophilic C_1N_1 with an aqueous electrolyte, several explicit water molecules were added to the model system manually inside the pores. In cases where the pore volume permits multiple molecules, they were introduced stepwise. Then, an optimization of their orientation and position followed, while keeping the matrix fixed, to find their energetically most favorable configurations. The adsorption energy was estimated as the difference in total energy between the hydrated system and the isolated components; see Equation 7.1.

$$\Delta E_{ads} = E_{solvated} - (E_{unsolvated} + E_{H_2O,isolated} * n_{H_2O}) \tag{7.1}$$

Table 7.1 lists the adsorption energies for complexes with different states of hydration. The most stable complexes observed release adsorption energies of 26.6 and 21.9 kJ/mol per water molecule, while other complexes show much weaker and even positive adsorption energies. In general, these adsorption energies are rather modest, given that other functionalized carbon matrices exhibit much higher adsorption energies and even non-functionalized carbon yields adsorption energies in the range of -32 kJ/mol [13], while the energy of a hydrogen bond of water is, for comparable computational methods and setup, around -20 kJ/mol [184, 185]. These differences can be explained by the lack of hydrogen bonding between the adsorbate and the adsorbent and steric hindrance due to the small pores in our spatially limited structural model. The highly endothermic adsorption energies are due to cases where the water molecule was placed in a highly unfavorable position, in some cases even leading to its dissociation during the energy minimization process. It is crucial to acknowledge that the system under investigation is composed of only 200 atoms, which hinders the formation of larger cavities that might be observed in experimental systems. Nevertheless, it can be concluded that within our model, only a limited fraction of the pores has the capacity to absorb water, and that the adsorbed water molecules are hydrogen-bonded to the surface. Given sufficient space, these molecules may form an ice-like structure that hampers water diffusion, further restricting the penetration of water into the deeper regions of the structure. This

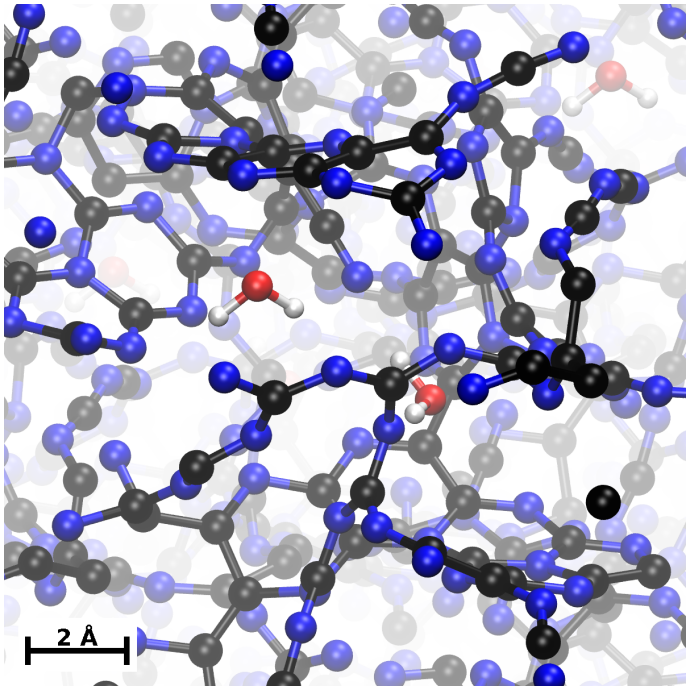

Figure 7.3.: Depiction of the amorphous structural model incorporating two central water molecules: the one on the right is hydrogen-bonded to nitrile and bridging nitrogen, whereas the one on the left mediates interactions with multiple nitrogen atoms. Both molecules are surrounded by ring structures and π-networks.

observation suggests that, contrary to expectations, hydrophilic systems may indeed exhibit hydrophobic behavior when examined at the nanoscale.

n(H2O)	E_{ads} [kJ/mol]	$E_{ads/n(H2O)}$ [kJ/mol]
1	-26.6	-26.6
2	-43.7	-21.9
1	-17.5	-17.5
3	-25.1	-8.4
1	15.7	15.7
2	34.8	17.4
1	33.5	33.5
1	36.0	36.0
1	47.7	47.7
3	164.5	54.8
1	59.6	59.6
1	101.9	101.9
1	119.7	119.7
1	127.8	127.8
1	179.1	179.1
1	277.7	277.7
1	280.5	280.5
1	468.3	468.3
1	577.3	577.3
1	587.7	587.7

Table 7.1.: Adsorption energies of water inside different pores. Where the pore volume permits, multiple water molecules were introduced, as tracked on the left column. The dashed line indicates the change from exothermic to endothermic adsorption.

7.3.2. Magnetic Shielding of Adsorbed Water

The computation of the NICS facilitates the identification of regions that are shielded or deshielded because of ring currents, structural defects, or heteroatoms within the pores. This process allows the assessment of the magnetic shielding experienced by an adsorbed water molecule and enables a comparison with experimentally obtained results, thereby providing insights into the local environment of water molecules within the synthesized material.

All NICS calculations were done using the all-electron Gaussian and augmented plane waves method [186, 187]. The pcSseg-2 basis set was employed in conjunction with a density cutoff of 400 Ry [188]. For the integration, the number of spherical and radial atomic grid points was set to 60 and 100, respectively. Nuclear shielding calculations were performed using the mixed position and step-function gauge (CSGT) [189] for the soft part of the induced current and IGAIM [190] for the local/hard part of the induced current. The center of each maximally localized Wannier center was used as its own orbital center. Magnetic shielding was calculated on a grid with a spacing of 0.5 Å that covers the whole simulation cell, and the shielding values were converted to the conventional $\delta[ppm]$ scale by referencing them to the average shielding of protons in tetramethylsilane; see Equation 7.2.

$$\delta[ppm] = 10^{-6}(Tr(\sigma_{ref,TMS}) - Tr(\sigma_{sample})) \tag{7.2}$$

With ^{1}H NMR several peaks were identified, ranging from 10.2 ppm for structural protons, 4.7 ppm for bulk water, 8.6 to 6.0 ppm for hydrogen bonded water and 1.1 to -1.5 ppm for water confined in nanopores. In order to further examine the proposed assignment of the peaks in the spectrum, two water molecules were introduced manually into the pores of the C_1N_1 matrix, followed by an optimization of their position and orientation. The structure and position of water molecules are depicted in Figure 7.3. The first water molecule (on the right) adjusts in a pore such that both its hydrogen atoms simultaneously form hydrogen bonds to the pore walls. The first hydrogen bond is directed towards a highly electronegative nitrile group, inducing a strong downfield shift of the corresponding water proton to 17.04 ppm. The other water proton forms a hydrogen bond with a nitrogen atom in the middle of an alternating CN aliphatic chain and exhibits a downfield shift of 7.7 ppm. The second water molecule was placed in the vicinity of a pyrazine ring without the

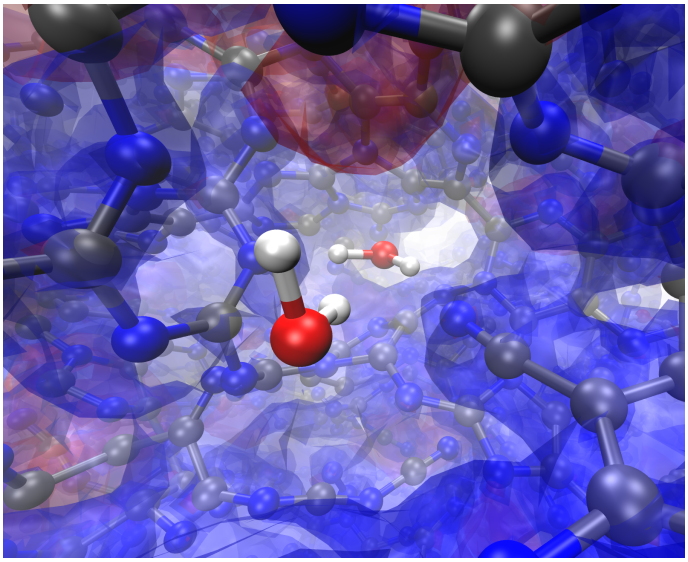

Figure 7.4.: Isosurfaces show shielded (blue) and deshielded (red) regions inside the porous structures.

possibility of forming any hydrogen bonds to the pore walls. Here, the calculated shift values of its two hydrogen atoms are as low as 1.26 and 0.9 ppm.

Although the exact experimental values are not met here, this is to be expected, given the effect of exchange-averaging of the chemical shift and the small cell size, which cannot conceivably capture all the possible microenvironments inside the matrix. However, the structural model provides insights into the observed shielding effects due to aromatic structures forming the pore walls, and deshielding effects due to hydrogen bonding to the matrix. For a water molecule that does not lie in the shielding cone of an aromatic structure, the observed downfield peaks are easily conceivable. The model confirms the assignment of upfield shifted peaks to water inside micropores as well as downfield shifted peaks to hydrogen-bonded water.

8. Conclusions

Carbon nitrides have been shown to be promising materials for many purposes and exist in a variety of different forms, ordered, like g-C_3N_4 or ABT-CN_2, doped with salts such as poly(heptazinimides) or amorphous, such as C_1N_1. This thesis aimed to contribute to their general understanding by studying several of these in detail to gather knowledge about mechanisms, reactivity, and stability.

Starting with the high-throughput search to find kinetically and thermodynamically stable CN_2 structures, multiple refinement steps were carried out, with greater accuracy of the calculations but fewer structures inspected for each step. From more than a million initial structures, less than hundred were retrieved and analyzed with respect to thermodynamic stability via molecular dynamics, using neural networks trained on all the data gathered in the steps before to accelerate it and reduce computational cost. The final structures for their optoelectronic properties were further investigated, and four promising materials were highlighted in the publication, although all were made accessible online. These materials are intriguing candidates for synthesis and usage as photocatalysts, energy storage materials, or for carbon capture.

The subsequent logical task involved the synthesis of these elements. Although there was an initial expectation that researchers would actively engage with them, it became apparent that conducting the synthesis was a task best undertaken independently by ourselves. For this, a material with promising properties and an ordered structure was chosen, and synthesizing approaches were evaluated. After great effort, two synthesis strategies could be successfully deployed, one wet synthesis approach using low temperatures and thus energy, and one oven synthesis approach using molten salt templating, using higher temperatures but almost no solvents. The materials have been carefully studied to verify their structure and composition, and successful synthesis, which has, to the best of my knowledge, been

demonstrated for the first time. Photocatalytic and electrochemical properties were studied, but have to be optimized in future work.

In addition, several different carbon nitrides have been studied in association with other experimentally working research groups, with a focus on investigating the adsorption mechanisms and net atomic charges, whose behavior detrimentally influences the adsorption properties. Different models have been developed, each individually tailored to map given experimental structures in the best possible way, with reasonable accuracy, and being able to answer the research questions.

In the first of these projects, Na- and H-poly(heptazineimides) were investigated with respect to their interaction with H^+ and NH_4^+ ions. These were introduced to simulate different levels of photocharging, modeled by expanding the system size but keeping the amount of adsorbates fixed, thereby lowering their concentration. Systems with 2, 4, 8, and 20 subunits of PHI were investigated. The results not only allow us to explain higher yields, which were observed at elevated temperatures, but also show that a lower degree of photocharging, equivalent to a higher mass loading of the catalyst, leads to weaker adsorbate-adsorbent interactions. The typical strong interaction between these two is a main reason for the low yield obtained in the experiment, as products cannot desorb. Elevated temperatures help overcome the desorption barrier and a decrease in barrier height accelerates desorption as well. This explanation of these mechanisms and connections was only possible due to the simulations conducted.

In a second project, the impact of terminal groups in KNa-PHI materials was investigated, focusing on their electron-donating and electron-accepting properties toward the backbone of the materials, which is detrimental to their adsorption properties. Two models that are identical apart from their terminal groups were developed and compared regarding net atomic charges, adsorption strength, and adsorption position. The key findings here are that the triazole-terminating groups investigated decreased the adsorption energy of O_2, compared to the standard amine-terminating groups, while only slightly shifting the optimal adsorption position. This is explained by redistribution of the electron probability density from KNa-PHI towards the terminating groups, increasing the adsorption strength by $\approx 2\frac{kJ}{mol}$. This may be one reason for the higher photocatalytic activity of the studied material.

The final chapter is a study of the wettability of amorphous C_1N_1 materials used for electrodes. Our collaborating experimentalists observed no correlation between surface area, hydrophilicity of the sample, directed by its nitrogen content, and wettability, although intuitively there should be a proportionality. To create an amorphous model with this stoichiometry, simulated annealing was applied, which formed a chemically accurate, chaotic model of two hundred atoms with multiple different functional groups and aromatic areas. Subsequently, multiple water molecules were introduced to various pores, and the adsorption of the molecules and NMR shifts were studied. This helped to clarify and explain experimentally observed NMR peaks, especially those with upfield shift to -1 ppm, which we could identify as adsorbed molecules within the shielding cone of aromatic rings. For small pores, adsorption energies are positive, as repulsion with pore walls predominates, but in medium sized pores we calculated adsorption energies up to $-26.6\ \frac{kJ}{mol}$. The wettability of nitrogen doped carbon materials can decrease, as strongly adsorbed water molecules block the accessibility of larger pores via interaction with the pore wall. A good pore size control is therefore key for steering electrode development.
I hope that this thesis has helped to shed light on previously unexplored aspects and can contribute, in a humble way, to deepening our understanding of the world that surrounds us.

9. Bibliography

[1] Justus Liebig. “Uber einige Stickstoff-Verbindungen”. In: *Annalen der Pharmacie* 10.1 (1834), pp. 1–47.

[2] Marvin L Cohen. “Calculation of bulk moduli of diamond and zinc-blende solids”. In: *Physical Review B* 32.12 (1985), p. 7988.

[3] Amy Y. Liu and Marvin L. Cohen. “Prediction of New Low Compressibility Solids”. In: *Science* 245.4920 (1989), pp. 841–842. ISSN: 0036-8075.

[4] Xinchen Wang et al. “A metal-free polymeric photocatalyst for hydrogen production from water under visible light”. In: *Nature materials* 8.1 (2009), pp. 76–80.

[5] Wen Zhao, Zhaoqian Yan, and Lei Qian. “Graphitic carbon nitride: preparation, properties and applications in energy storage”. In: *Engineered Science* 10.7 (2020), pp. 24–34.

[6] Tamikuni Komatsu and Miho Samejima. “Preparation of carbon nitride C2N by shock-wave compression of poly (aminomethineimine)”. In: *Journal of Materials Chemistry* 8.1 (1998), pp. 193–196.

[7] Janina Kossmann et al. “Guanine-Derived Porous Carbonaceous Materials: Towards C1N1”. In: *ChemSusChem* 13.24 (2020), p. 6643.

[8] Aleksandr Savateev et al. “Potassium poly (heptazine imides) from aminotetrazoles: shifting band gaps of carbon nitride-like materials for more efficient solar hydrogen and oxygen evolution”. In: *ChemCatChem* 9.1 (2017), pp. 167–174.

[9] Pawan Kumar et al. “C3N5: A low bandgap semiconductor containing an azo-linked carbon nitride framework for photocatalytic, photovoltaic and adsorbent applications”. In: *Journal of the American Chemical Society* 141.13 (2019), pp. 5415–5436.

[10] Bohayra Mortazavi et al. “Nanoporous C3N4, C3N5 and C3N6 nanosheets; novel strong semiconductors with low thermal conductivities and appealing optical/electronic properties”. In: *Carbon* 167 (2020), pp. 40–50.

[11] Qun Wei et al. “A new 2D auxetic CN2 nanostructure with high energy density and mechanical strength”. In: *Physical Chemistry Chemical Physics* (2021).

[12] Quan Li et al. “A novel low compressible and superhard carbon nitride: Body-centered tetragonal CN2”. In: *Physical chemistry chemical physics : PCCP* 14 (Aug. 2012), pp. 13081–7.

[13] Julian Heske et al. “When water becomes an integral part of carbon–combining theory and experiment to understand the zeolite-like water adsorption properties of porous C 2 N materials”. In: *Journal of Materials Chemistry A* 9.39 (2021), pp. 22563–22572.

[14] Ralf Walczak et al. “Controlling the strength of interaction between carbon dioxide and nitrogen-rich carbon materials by molecular design”. In: *Sustainable Energy & Fuels* 3.10 (2019), pp. 2819–2827.

[15] Ivo F Teixeira et al. “Overcoming Electron Transfer Efficiency Bottlenecks for Hydrogen Production in Highly Crystalline Carbon Nitride-Based Materials”. In: *Advanced Sustainable Systems* 6.3 (2022), p. 2100429.

[16] Arne Thomas et al. “Graphitic carbon nitride materials: variation of structure and morphology and their use as metal-free catalysts”. In: *Journal of Materials Chemistry* 18.41 (2008), pp. 4893–4908.

[17] Jian Liu, Hongqiang Wang, and Markus Antonietti. “Graphitic carbon nitride “reloaded”: emerging applications beyond (photo) catalysis”. In: *Chemical Society Reviews* 45.8 (2016), pp. 2308–2326.

[18] Anita Sudhaik et al. “Review on fabrication of graphitic carbon nitride based efficient nanocomposites for photodegradation of aqueous phase organic pollutants”. In: *Journal of Industrial and Engineering Chemistry* 67 (2018), pp. 28–51.

[19] Kezhen Qi, Shu-yuan Liu, and Amir Zada. “Graphitic carbon nitride, a polymer photocatalyst”. In: *Journal of the Taiwan Institute of Chemical Engineers* 109 (2020), pp. 111–123.

[20] In Young Kim et al. “Thermodynamically Stable Mesoporous C3N7 and C3N6 with Ordered Structure and Their Excellent Performance for Oxygen Reduction Reaction”. In: *Small* (Nov. 2019), p. 1903572. ISSN: 1613-6810. DOI: 10.1002/smll.201903572.

[21] Xinghong Cai et al. “Metal-modified s-C3N6 as a potential superior sensing medium for effective capture of toxic waste gases CO, H2S and SO2 in the iron and steel industry based on first-principles investigations”. In: *Applied Surface Science* 606 (2022), p. 154947.

[22] Mengshan Chen et al. “Efficient degradation of formaldehyde based on DFT-screened metal-doped C 3 N 6 monolayer photocatalysts: Performance evaluation and mechanistic insights”. In: *Physical Chemistry Chemical Physics* 25.37 (2023), pp. 25353–25360.

[23] Yaqi She et al. “S-C3N6 monolayer by atomic doping serving as solar cells and photocatalyst”. In: *Colloids and Surfaces A: Physicochemical and Engineering Aspects* 688 (2024), p. 133616.

[24] Klaus Capelle. “A bird’s-eye view of density-functional theory”. In: *Brazilian journal of physics* 36 (2006), pp. 1318–1343.

[25] Wolfram Koch and Max C Holthausen. *A chemist’s guide to density functional theory*. John Wiley & Sons, 2015.

[26] Christopher J Cramer. *Essentials of computational chemistry: theories and models*. John Wiley & Sons, 2013.

[27] Frank Jensen. *Introduction to computational chemistry*. John wiley & sons, 2017.

[28] Erwin Schrödinger. “Quantisierung als eigenwertproblem”. In: *Annalen der physik* 385.13 (1926), pp. 437–490.

[29] M. Born and R. Oppenheimer. “Zur Quantentheorie der Molekeln”. In: *Annalen der Physik* 389.20 (1927), pp. 457–484. DOI: https://doi.org/10.1002/andp.19273892002. eprint: https://onlinelibrary.wiley.com/doi/pdf/10.1002/andp.19273892002. URL: https://onlinelibrary.wiley.com/doi/abs/10.1002/andp.19273892002.

[30] P. Hohenberg and W. Kohn. “Inhomogeneous Electron Gas”. In: *Phys. Rev.* 136 (3B Nov. 1964), B864–B871.

[31] Mel Levy. “Electron densities in search of Hamiltonians”. In: *Physical Review A* 26.3 (1982), p. 1200.

[32] Elliott H Lieb. “Density functionals for Coulomb systems”. In: *International journal of quantum chemistry* 24.3 (1983), pp. 243–277.

[33] Walter Kohn and Lu Jeu Sham. “Self-consistent equations including exchange and correlation effects”. In: *Physical review* 140.4A (1965), A1133.

[34] John P Perdew, Kieron Burke, and Matthias Ernzerhof. “Generalized gradient approximation made simple”. In: *Physical review letters* 77.18 (1996), p. 3865.

[35] Axel D Becke. “Density-functional exchange-energy approximation with correct asymptotic behavior”. In: *Physical review A* 38.6 (1988), p. 3098.

[36] Chengteh Lee, Weitao Yang, and Robert G Parr. “Development of the Colle-Salvetti correlation-energy formula into a functional of the electron density”. In: *Physical review B* 37.2 (1988), p. 785.

[37] Jan Gerit Brandenburg et al. “B97-3c: A revised low-cost variant of the B97-D density functional method”. In: *The Journal of chemical physics* 148.6 (2018).

[38] Jianwei Sun, Adrienn Ruzsinszky, and John P Perdew. “Strongly constrained and appropriately normed semilocal density functional”. In: *Physical review letters* 115.3 (2015), p. 036402.

[39] Soumen Saha, Ram Kinkar Roy, and Paul W Ayers. "Are the Hirshfeld and Mulliken population analysis schemes consistent with chemical intuition?" In: *International journal of quantum chemistry* 109.9 (2009), pp. 1790–1806.

[40] Robert S Mulliken. "Electronic population analysis on LCAO–MO molecular wave functions. I". In: *The Journal of chemical physics* 23.10 (1955), pp. 1833–1840.

[41] Brian Harvey Chirgwin and Charles Alfred Coulson. "The electronic structure of conjugated systems. VI". In: *Proceedings of the Royal Society of London. Series A. Mathematical and Physical Sciences* 201.1065 (1950), pp. 196–209.

[42] Per-Olov Löwdin. "On the non-orthogonality problem connected with the use of atomic wave functions in the theory of molecules and crystals". In: *The Journal of Chemical Physics* 18.3 (1950), pp. 365–375.

[43] Alan E Reed, Robert B Weinstock, and Frank Weinhold. "Natural population analysis". In: *The Journal of chemical physics* 83.2 (1985), pp. 735–746.

[44] Benjamin D Dunnington and JR Schmidt. "Generalization of natural bond orbital analysis to periodic systems: applications to solids and surfaces via plane-wave density functional theory". In: *Journal of Chemical Theory and Computation* 8.6 (2012), pp. 1902–1911.

[45] Thomas A Manz and Nidia Gabaldon Limas. "Introducing DDEC6 atomic population analysis: part 1. Charge partitioning theory and methodology". In: *RSC advances* 6.53 (2016), pp. 47771–47801.

[46] Fred L Hirshfeld. "Bonded-atom fragments for describing molecular charge densities". In: *Theoretica chimica acta* 44 (1977), pp. 129–138.

[47] Aleksandr V Marenich et al. "Charge model 5: An extension of Hirshfeld population analysis for the accurate description of molecular interactions in gaseous and condensed phases". In: *Journal of chemical theory and computation* 8.2 (2012), pp. 527–541.

[48] Patrick Bultinck et al. "Critical analysis and extension of the Hirshfeld atoms in molecules". In: *The Journal of chemical physics* 126.14 (2007).

[49] Ernest R Davidson and Subhas Chakravorty. “A test of the Hirshfeld definition of atomic charges and moments”. In: *Theoretica chimica acta* 83.5 (1992), pp. 319–330.

[50] Karlo Nolkemper et al. “Kinetically Stable and Highly Ordered Two-Dimensional CN2 Crystal Structures”. In: *The Journal of Physical Chemistry C* (2023).

[51] Xinchen Wang et al. “A metal-free polymeric photocatalyst for hydrogen production from water under visible light - Nature Materials”. In: *Nat. Mater.* 8.1 (Jan. 2009), pp. 76–80. ISSN: 1476-4660. DOI: 10.1038/nmat2317.

[52] Justus Liebig. “Ueber einige stickstoffverbindungen”. In: *Annalen der Physik* 110.4 (1835), pp. 570–613.

[53] Arne Thomas et al. “Graphitic carbon nitride materials: variation of structure and morphology and their use as metal-free catalysts”. In: *Journal of Materials Chemistry* 18.41 (2008), pp. 4893–4908.

[54] Xinchen Wang et al. “A metal-free polymeric photocatalyst for hydrogen production from water under visible light”. In: *Nature materials* 8.1 (2009), pp. 76–80.

[55] Bettina V Lotsch and Wolfgang Schnick. “From triazines to heptazines: novel nonmetal tricyanomelaminates as precursors for graphitic carbon nitride materials”. In: *Chemistry of materials* 18.7 (2006), pp. 1891–1900.

[56] Zaiwang Zhao, Yanjuan Sun, and Fan Dong. “Graphitic carbon nitride based nanocomposites: a review”. In: *Nanoscale* 7.1 (2015), pp. 15–37. DOI: 10.1039/C4NR03008G.

[57] Guoping Dong et al. “A fantastic graphitic carbon nitride (g-C3N4) material: Electronic structure, photocatalytic and photoelectronic properties”. In: *J. Photochem. Photobiol., C* 20 (Sept. 2014), pp. 33–50. ISSN: 1389-5567. DOI: 10.1016/j.jphotochemrev.2014.04.002.

[58] Zahra Hajiahmadi et al. “First-Principles Study of 2D Haeckelite C7N as a High-Capacity Anode for Post-Lithium-Ion Batteries”. In: *ACS Appl. Nano Mater.* 6.14 (July 2023), pp. 12862–12870. DOI: 10.1021/acsanm.3c01563.

[59] Javeed Mahmood et al. “Two-dimensional polyaniline (C3N) from carbonized organic single crystals in solid state”. In: *Proc. Natl. Acad. Sci. U.S.A.* 113.27 (July 2016), pp. 7414–7419. ISSN: 0027-8424. DOI: 10.1073/pnas.1605318113.

[60] Javeed Mahmood et al. “Nitrogenated holey two-dimensional structures”. In: *Nat. Commun.* 6.6486 (Mar. 2015), pp. 1–7. ISSN: 2041-1723. DOI: 10.1038/ncomms7486.

[61] Janina Kossmann et al. “Guanine-Derived Porous Carbonaceous Materials: Towards C1N1”. In: *ChemSusChem* 13.24 (2020), pp. 6643–6650. DOI: https://doi.org/10.1002/cssc.202002274.

[62] Gurudas P. Mane et al. “Highly Ordered Nitrogen-Rich Mesoporous Carbon Nitrides and Their Superior Performance for Sensing and Photocatalytic Hydrogen Generation”. In: *Angew. Chem. Int. Ed.* 56.29 (July 2017), pp. 8481–8485. ISSN: 1433-7851. DOI: 10.1002/anie.201702386.

[63] In Young Kim et al. “Ordered Mesoporous C3N5 with a Combined Triazole and Triazine Framework and Its Graphene Hybrids for the Oxygen Reduction Reaction (ORR)”. In: *Angew. Chem.* 130.52 (Dec. 2018), pp. 17381–17386. ISSN: 0044-8249. DOI: 10.1002/ange.201811061.

[64] Derek W. Keefer et al. “Tetracyanomethane under Pressure: Extended CN Polymers from Precursors with Built-in sp3 Centers”. In: *J. Phys. Chem. A* 122.11 (Mar. 2018), pp. 2858–2863. ISSN: 1089-5639. DOI: 10.1021/acs.jpca.7b10729.

[65] Dominique Laniel et al. “High pressure study of a highly energetic nitrogen-rich carbon nitride, cyanuric triazide”. In: *J. Chem. Phys.* 141.23 (Dec. 2014), p. 234506. ISSN: 0021-9606. DOI: 10.1063/1.4902984.

[66] Haiyan Wang et al. “A Mesoporous Rod-like g-C3N5 Synthesized by Salt-Guided Strategy: As a Superior Photocatalyst for Degradation of Organic Pollutant”. In: *ACS Sustainable Chem. Eng.* 7.1 (Jan. 2019), pp. 625–631. DOI: 10.1021/acssuschemeng.8b04182.

[67] Pawan Kumar et al. “C3N5: A Low Bandgap Semiconductor Containing an Azo-Linked Carbon Nitride Framework for Photocatalytic, Photovoltaic and Adsorbent Applications”. In: *J. Am. Chem. Soc.* 141.13 (Apr. 2019), pp. 5415–5436. ISSN: 0002-7863. DOI: 10.1021/jacs.9b00144.

[68] Tianyu Liu et al. “Preparation of C3N5 nanosheets with enhanced performance in photocatalytic methylene blue (MB) degradation and H2-evolution from water splitting”. In: *Environ. Res.* 188 (Sept. 2020), p. 109741. ISSN: 0013-9351. DOI: 10.1016/j.envres.2020.109741.

[69] S. Alireza Ghasemi, Hossein Mirhosseini, and Thomas D. Kühne. “Thermodynamically stable polymorphs of nitrogen-rich carbon nitrides: a C 3 N 5 study”. In: *Phys. Chem. Chem. Phys.* 23.11 (2021), pp. 6422–6432. DOI: 10.1039/D0CP06185A.

[70] Gerardo Algara-Siller et al. “Triazine-Based Graphitic Carbon Nitride: a Two-Dimensional Semiconductor”. In: *Angew. Chem. Int. Ed.* 53.29 (July 2014), pp. 7450–7455. ISSN: 1433-7851. DOI: 10.1002/anie.201402191.

[71] Zhenxing Yang et al. “Tuning the band gap and the nitrogen content in carbon nitride materials by high temperature treatment at high pressure”. In: *Carbon* 130 (Apr. 2018), pp. 170–177. ISSN: 0008-6223. DOI: 10.1016/j.carbon.2017.12.115.

[72] Daria Baranowska et al. “Influence of Hydrogenation on Morphology, Chemical Structure and Photocatalytic Efficiency of Graphitic Carbon Nitride”. In: *International Journal of Molecular Sciences* 22.23 (2021). ISSN: 1422-0067. URL: https://www.mdpi.com/1422-0067/22/23/13096.

[73] Xiaojie She et al. “Oxygenated monolayer carbon nitride for excellent photocatalytic hydrogen evolution and external quantum efficiency”. In: *Nano Energy* 27 (2016), pp. 138–146. ISSN: 2211-2855. DOI: https://doi.org/10.1016/j.nanoen.2016.06.042. URL: https://www.sciencedirect.com/science/article/pii/S2211285516302257.

[74] Sigismund T. A. G. Melissen et al. “DFT Perspective on the Thermochemistry of Carbon Nitride Synthesis”. In: *J. Phys. Chem. C* 120.43 (Nov. 2016), pp. 24542–24550. ISSN: 1932-7447. DOI: 10.1021/acs.jpcc.6b06335.

[75] Tiago Botari et al. “Thermodynamic Equilibria in Carbon Nitride Photocatalyst Materials and Conditions for the Existence of Graphitic Carbon Nitride g-C3N4”. In: *Chem. Mater.* 29.10 (May 2017), pp. 4445–4453. ISSN: 0897-4756. DOI: 10.1021/acs.chemmater.7b00965.

[76] Quan Li et al. “A novel low compressible and superhard carbon nitride: Body-centered tetragonal CN2”. In: *Phys. Chem. Chem. Phys.* 14 (37 2012), pp. 13081–13087. DOI: 10.1039/C2CP41694H. URL: http://dx.doi.org/10.1039/C2CP41694H.

[77] Shunhong Zhang et al. “Beyond Graphitic Carbon Nitride: Nitrogen-Rich Penta-CN2 Sheet”. In: *J. Phys. Chem. C* 120.7 (Feb. 2016), pp. 3993–3998. ISSN: 1932-7447. DOI: 10.1021/acs.jpcc.5b12510.

[78] Zhang Shunhong et al. “Penta-graphene: A new carbon allotrope”. In: *Proc. Natl. Acad. Sci. U.S.A.* 112.8 (Feb. 2015), pp. 2372–2377. ISSN: 0027-8424. DOI: 10.1073/pnas.1416591112.

[79] Bohayra Mortazavi et al. “Nanoporous C3N4, C3N5 and C3N6 nanosheets; novel strong semiconductors with low thermal conductivities and appealing optical/electronic properties”. In: *Carbon* 167 (Oct. 2020), pp. 40–50. ISSN: 0008-6223. DOI: 10.1016/j.carbon.2020.05.105.

[80] Qun Wei et al. “A new 2D auxetic CN 2 nanostructure with high energy density and mechanical strength”. In: *Phys. Chem. Chem. Phys.* 23.7 (2021), pp. 4353–4364. DOI: 10.1039/D0CP06509A.

[81] Stefan Goedecker. “Minima hopping: An efficient search method for the global minimum of the potential energy surface of complex molecular systems”. In: *J. Chem. Phys.* 120.21 (June 2004), pp. 9911–9917. ISSN: 0021-9606. DOI: 10.1063/1.1724816.

[82] Maximilian Amsler and Stefan Goedecker. “Crystal structure prediction using the minima hopping method”. In: *J. Chem. Phys.* 133.22 (Dec. 2010), p. 224104. ISSN: 0021-9606. DOI: 10.1063/1.3512900.

[83] Maximilian Amsler et al. “FLAME: A library of atomistic modeling environments”. In: *Comput. Phys. Commun.* 256 (Nov. 2020), p. 107415. ISSN: 0010-4655. DOI: 10.1016/j.cpc.2020.107415.

[84] M. Elstner et al. “Self-consistent-charge density-functional tight-binding method for simulations of complex materials properties”. In: *Phys. Rev. B* 58.11 (Sept. 1998), pp. 7260–7268. ISSN: 2469-9969. DOI: 10.1103/PhysRevB.58.7260.

[85] B. Aradi, B. Hourahine, and Th. Frauenheim. “DFTB+, a Sparse Matrix-Based Implementation of the DFTB Method”. In: *J. Phys. Chem. A* 111.26 (July 2007), pp. 5678–5684. ISSN: 1089-5639. DOI: 10.1021/jp070186p.

[86] B. Hourahine et al. “DFTB+, a software package for efficient approximate density functional theory based atomistic simulations”. In: *J. Chem. Phys.* 152.12 (Mar. 2020), p. 124101. ISSN: 0021-9606. DOI: 10.1063/1.5143190.

[87] Artem R. Oganov and Mario Valle. “How to quantify energy landscapes of solids”. In: *J. Chem. Phys.* 130.10 (Mar. 2009), p. 104504. ISSN: 0021-9606. DOI: 10.1063/1.3079326.

[88] G. Kresse and J. Hafner. “Ab initio molecular dynamics for liquid metals”. In: *Phys. Rev. B* 47.1 (Jan. 1993), 558–561(R). ISSN: 2469-9969. DOI: 10.1103/PhysRevB.47.558.

[89] G. Kresse and J. Furthmüller. “Efficient iterative schemes for ab initio total-energy calculations using a plane-wave basis set”. In: *Phys. Rev. B* 54.16 (Oct. 1996), pp. 11169–11186. ISSN: 2469-9969. DOI: 10.1103/PhysRevB.54.11169.

[90] Volker Blum et al. “Ab initio molecular simulations with numeric atom-centered orbitals”. In: *Comput. Phys. Commun.* 180.11 (Nov. 2009), pp. 2175–2196. ISSN: 0010-4655. DOI: 10.1016/j.cpc.2009.06.022.

[91] P. E. Blöchl. “Projector augmented-wave method”. In: *Phys. Rev. B* 50.24 (Dec. 1994), pp. 17953–17979. ISSN: 2469-9969. DOI: 10.1103/PhysRevB.50.17953.

[92] John P. Perdew, Kieron Burke, and Matthias Ernzerhof. “Generalized Gradient Approximation Made Simple”. In: *Phys. Rev. Lett.* 77.18 (Oct. 1996), pp. 3865–3868. ISSN: 1079-7114. DOI: 10.1103/PhysRevLett.77.3865.

[93] Aliaksandr V. Krukau et al. “Influence of the exchange screening parameter on the performance of screened hybrid functionals”. In: *J. Chem. Phys.* 125.22 (Dec. 2006), p. 224106. ISSN: 0021-9606. DOI: 10.1063/1.2404663.

[94] Alexandre Tkatchenko and Matthias Scheffler. “Accurate Molecular Van Der Waals Interactions from Ground-State Electron Density and Free-Atom Reference Data”. In: *Phys. Rev. Lett.* 102.7 (Feb. 2009), p. 073005. ISSN: 1079-7114. DOI: 10.1103/PhysRevLett.102.073005.

[95] Atsushi Togo and Isao Tanaka. “First principles phonon calculations in materials science”. In: *Scr. Mater.* 108 (Nov. 2015), p. 1. ISSN: 1359-6462. DOI: 10.1016/j.scriptamat.2015.07.021.

[96] Thomas D. Kühne et al. “Efficient and Accurate Car-Parrinello-like Approach to Born-Oppenheimer Molecular Dynamics”. In: *Phys. Rev. Lett.* 98 (6 Feb. 2007), p. 066401. DOI: 10.1103/PhysRevLett.98.066401. URL: https://link.aps.org/doi/10.1103/PhysRevLett.98.066401.

[97] Jörg Behler and Michele Parrinello. “Generalized Neural-Network Representation of High-Dimensional Potential-Energy Surfaces”. In: *Phys. Rev. Lett.* 98.14 (Apr. 2007), p. 146401. ISSN: 1079-7114. DOI: 10.1103/PhysRevLett.98.146401.

[98] Albert P. Bartók et al. “Gaussian Approximation Potentials: The Accuracy of Quantum Mechanics, without the Electrons”. In: *Phys. Rev. Lett.* 104.13 (Apr. 2010), p. 136403. ISSN: 1079-7114. DOI: 10.1103/PhysRevLett.104.136403.

[99] S. Alireza Ghasemi et al. “Interatomic potentials for ionic systems with density functional accuracy based on charge densities obtained by a neural network”. In: *Phys. Rev. B* 92.4 (July 2015), p. 045131. ISSN: 2469-9969. DOI: 10.1103/PhysRevB.92.045131.

[100] Ehsan Rahmatizad Khajehpasha et al. “CENT2: Improved charge equilibration via neural network technique”. In: *Phys. Rev. B* 105.14 (Apr. 2022), p. 144106. ISSN: 2469-9969. DOI: 10.1103/PhysRevB.105.144106.

[101] Rustam Z. Khaliullin et al. “Graphite-diamond phase coexistence study employing a neural-network mapping of the ab initio potential energy surface”. In: *Phys. Rev. B* 81 (10 Mar. 2010), p. 100103. DOI: 10.1103/PhysRevB.81.100103. URL: https://link.aps.org/doi/10.1103/PhysRevB.81.100103.

[102] Rustam Z. Khaliullin et al. “Nucleation mechanism for the direct graphite-to-diamond phase transition”. In: *Nat. Mater.* 10 (Sept. 2011), pp. 693–697. ISSN: 1476-4660. DOI: 10.1038/nmat3078.

[103] Hagai Eshet et al. “Microscopic Origins of the Anomalous Melting Behavior of Sodium under High Pressure”. In: *Phys. Rev. Lett.* 108 (11 Mar. 2012), p. 115701. DOI: 10.1103/PhysRevLett.108.115701. URL: https://link.aps.org/doi/10.1103/PhysRevLett.108.115701.

[104] Volker L. Deringer and Gábor Csányi. “Machine learning based interatomic potential for amorphous carbon”. In: *Phys. Rev. B* 95.9 (Mar. 2017), p. 094203. ISSN: 2469-9969. DOI: 10.1103/PhysRevB.95.094203.

[105] Hossein Asnaashari Eivari et al. “Two-Dimensional Hexagonal Sheet of TiO2”. In: *Chem. Mater.* 29.20 (Oct. 2017), pp. 8594–8603. ISSN: 0897-4756. DOI: 10.1021/acs.chemmater.7b02031.

[106] Sam Azadi and T. D. Kühne. “Quantum Monte Carlo calculations of van der Waals interactions between aromatic benzene rings”. In: *Phys. Rev. B* 97 (20 May 2018), p. 205428. DOI: 10.1103/PhysRevB.97.205428. URL: https://link.aps.org/doi/10.1103/PhysRevB.97.205428.

[107] Sam Azadi, George H. Booth, and Thomas D. Kühne. “Equation of state of atomic solid hydrogen by stochastic many-body wave function methods”. In: *The Journal of Chemical Physics* 153.20 (2020), p. 204107. DOI: 10.1063/5.0026499.

[108] https://doi.org/10.5281/zenodo.8344887.

[109] A. P. Thompson et al. “LAMMPS - a flexible simulation tool for particle-based materials modeling at the atomic, meso, and continuum scales”. In: *Comp. Phys. Comm.* 271 (2022), p. 108171. DOI: 10.1016/j.cpc.2021.108171.

[110] S. Nosé and M. L. Klein. “Constant pressure molecular-dynamics for molecular-systems”. In: *Mol. Phys.* 50 (1983), pp. 1055–1076.

[111] W. G. Hoover. “Canonical dynamics - Equilibrium phase-space distributions”. In: *Phys. Rev. A* 31 (1985), pp. 1695–1697.

[112] Alex M. Ganose, Adam J. Jackson, and David O. Scanlon. "sumo: Command-line tools for plotting and analysis of periodic ∗ab initio∗ calculations". In: *Journal of Open Source Software* 3.28 (Aug. 2018), p. 717. ISSN: 2475-9066. DOI: 10.21105/joss.00717.

[113] K. Momma and F. Izumi. "VESTA 3 for three-dimensional visualization of crystal, volumetric and morphology data". In: *J. Appl. Crystallogr.* 44.6 (Dec. 2011), pp. 1272–1276. ISSN: 0021-8898. DOI: 10.1107/S0021889811038970.

[114] Swapnil Deshpande et al. "Tuning the electronic, magnetic, and sensing properties of a single atom embedded microporous C 3 N 6 monolayer towards XO 2 (X = C, N, S) gases". In: *New J. Chem.* 46.28 (2022), pp. 13752–13765. DOI: 10.1039/D2NJ01956F.

[115] Yexin Feng et al. "The atomic structures of carbon nitride sheets for cathode oxygen reduction catalysis". In: *J. Chem. Phys.* 138.16 (Apr. 2013), p. 164706. ISSN: 0021-9606. DOI: 10.1063/1.4802188.

[116] Bicheng Zhu et al. "First-principle calculation study of tri-s-triazine-based g-C3N4: A review". In: *Appl. Catal., B* 224 (May 2018), pp. 983–999. ISSN: 0926-3373. DOI: 10.1016/j.apcatb.2017.11.025.

[117] Bicheng Zhu et al. "Review on DFT calculation of s-triazine-based carbon nitride". In: *Carbon Energy* 1.1 (Sept. 2019), pp. 32–56. ISSN: 2637-9368. DOI: 10.1002/cey2.1.

[118] Ping Niu et al. "Distinctive defects engineering in graphitic carbon nitride for greatly extended visible light photocatalytic hydrogen evolution". In: *Nano Energy* 44 (Feb. 2018), pp. 73–81. ISSN: 2211-2855. DOI: 10.1016/j.nanoen.2017.11.059.

[119] Saibo Chen et al. "Graphitic carbon nitride quantum dots in situ coupling to Bi2MoO6 nanohybrids with enhanced charge transfer performance and photoelectrochemical detection of copper ion". In: *J. Electroanal. Chem.* 787 (Feb. 2017), pp. 66–71. ISSN: 1572-6657. DOI: 10.1016/j.jelechem.2017.01.042.

[120] Ying Xu et al. “Adsorption behaviors of HCN, SO2, H2S and NO molecules on graphitic carbon nitride with Mo atom decoration”. In: *Appl. Surf. Sci.* 501 (Jan. 2020), p. 144199. ISSN: 0169-4332. DOI: 10.1016/j.apsusc.2019.144199.

[121] Yaocheng Deng et al. “Insight into highly efficient simultaneous photocatalytic removal of Cr(VI) and 2,4-diclorophenol under visible light irradiation by phosphorus doped porous ultrathin g-C3N4 nanosheets from aqueous media: Performance and reaction mechanism”. In: *Appl. Catal., B* 203 (Apr. 2017), pp. 343–354. ISSN: 0926-3373. DOI: 10.1016/j.apcatb.2016.10.046.

[122] Xinchen Wang, Siegfried Blechert, and Markus Antonietti. “Polymeric graphitic carbon nitride for heterogeneous photocatalysis”. In: *Acs Catalysis* 2.8 (2012), pp. 1596–1606.

[123] Oleksandr Savateev et al. “Extent of carbon nitride photocharging controls energetics of hydrogen transfer in photochemical cascade processes”. In: *Nature Communications* 14.1 (2023), p. 7684.

[124] Kai Xiao et al. “Carbon nitride nanotube for ion transport based photorechargeable electric energy storage”. In: *Nano Energy* 67 (2020), p. 104230.

[125] Yuqing Luo et al. “Graphitic carbon nitride based materials for electrochemical energy storage”. In: *Journal of materials chemistry A* 7.3 (2019), pp. 901–924.

[126] Marilyn Mary Xavier, P Radhakrishnan Nair, and Suresh Mathew. “Emerging trends in sensors based on carbon nitride materials”. In: *Analyst* 144.5 (2019), pp. 1475–1491.

[127] Yongqiang Dong et al. “Graphitic carbon nitride materials: sensing, imaging and therapy”. In: *Small* 12.39 (2016), pp. 5376–5393.

[128] Yang Wang et al. “Graphitic carbon nitride (gC 3 N 4)-based membranes for advanced separation”. In: *Journal of Materials Chemistry A* 8.37 (2020), pp. 19133–19155.

[129] Janina Kossmann et al. “Guanine condensates as covalent materials and the concept of cryptopores”. In: *Carbon* 172 (2021), pp. 497–505.

[130] Sudhir K Sahoo et al. “On the possibility of helium adsorption in nitrogen doped graphitic materials”. In: *Scientific Reports* 10.1 (2020), p. 5832.

[131] Pawan Kumar et al. “C3N5: a low bandgap semiconductor containing an azo-linked carbon nitride framework for photocatalytic, photovoltaic and adsorbent applications”. In: *Journal of the American Chemical Society* 141.13 (2019), pp. 5415–5436.

[132] S Alireza Ghasemi, Hossein Mirhosseini, and Thomas D Kühne. “Thermodynamically stable polymorphs of nitrogen-rich carbon nitrides: a C 3 N 5 study”. In: *Physical Chemistry Chemical Physics* 23.11 (2021), pp. 6422–6432.

[133] Christian Mark Pelicano and Markus Antonietti. “Metal poly (heptazine imides) as multifunctional photocatalysts for solar fuel production”. In: *Angewandte Chemie International Edition* 63.24 (2024), e202406290.

[134] Christian Mark Pelicano et al. “Rational design of a carbon/potassium poly (heptazine imide) heterojunction for enhanced photocatalytic H 2 and H 2 O 2 evolution”. In: *Journal of Materials Chemistry A* 12.1 (2024), pp. 475–482.

[135] In Young Kim et al. “Thermodynamically stable mesoporous C3N7 and C3N6 with ordered structure and their excellent performance for oxygen reduction reaction”. In: *Small* 16.12 (2020), p. 1903572.

[136] Xiaogang Tong, Jizu Li, and Ningning Zhang. “Computational Exploration of Carbon Nitride (S-C3n6) Monolayer as Advanced Energy Storage Materials”. In: *Available at SSRN 5187547* (2025).

[137] Yanxin Yu et al. “Fully extended conjugated azo-bridged covalent triazine framework with maximum dual-redox-active sites for advanced lithium organic batteries”. In: *Nano Energy* 137 (2025), p. 110808.

[138] Michael J Bojdys et al. “Ionothermal synthesis of crystalline, condensed, graphitic carbon nitride”. In: *Chemistry–A European Journal* 14.27 (2008), pp. 8177–8182.

[139] Xiaofeng Liu, Nina Fechler, and Markus Antonietti. “Salt melt synthesis of ceramics, semiconductors and carbon nanostructures”. In: *Chemical Society Reviews* 42.21 (2013), pp. 8237–8265.

[140] Jiaxin Li et al. “When High-Temperature Cesium Chemistry Meets Self-Templating: Metal Acetates as Building Blocks of Unusual Highly Porous Carbons”. In: *Angewandte Chemie* 135.26 (2023), e202217808.

[141] Jürg Hutter et al. “cp2k: atomistic simulations of condensed matter systems”. In: *Wiley Interdisciplinary Reviews: Computational Molecular Science* 4.1 (2014), pp. 15–25.

[142] Thomas D Kühne et al. “CP2K: An electronic structure and molecular dynamics software package-Quickstep: Efficient and accurate electronic structure calculations”. In: *The Journal of Chemical Physics* 152.19 (2020).

[143] By Gerald Lippert, JURG HUTTER PARRINELLO, and MICHELE. “A hybrid Gaussian and plane wave density functional scheme”. In: *Molecular Physics* 92.3 (1997), pp. 477–488.

[144] Richard Car and Mark Parrinello. “Unified approach for molecular dynamics and density-functional theory”. In: *Physical review letters* 55.22 (1985), p. 2471.

[145] Thomas A Manz and Nidia Gabaldon Limas. “DDEC6: A method for computing even-tempered net atomic charges in periodic and nonperiodic materials”. In: *arXiv preprint arXiv:1512.08270* (2015).

[146] Nidia Gabaldon Limas and Thomas A Manz. “Introducing DDEC6 atomic population analysis: part 4. Efficient parallel computation of net atomic charges, atomic spin moments, bond orders, and more”. In: *RSC advances* 8.5 (2018), pp. 2678–2707.

[147] William Humphrey, Andrew Dalke, and Klaus Schulten. “VMD – Visual Molecular Dynamics”. In: *Journal of Molecular Graphics* 14 (1996), pp. 33–38.

[148] Daniela Dirtu et al. “Thermal decomposition of ammonia. N2H4-an intermediate reaction product”. In: *Open Chemistry* 4.4 (2006), pp. 666–673.

[149] Yu-Lin Wang et al. “IR spectroscopy and theoretical vibrational calculation of the melamine molecule”. In: *Journal of the Chemical Society, Faraday Transactions* 93.19 (1997), pp. 3445–3451.

[150] Chaofeng Huang et al. “Unraveling fundamental active units in carbon nitride for photocatalytic oxidation reactions”. In: *Nature Communications* 12.1 (2021), p. 320.

[151] Guigang Zhang et al. “Optimizing optical absorption, exciton dissociation, and charge transfer of a polymeric carbon nitride with ultrahigh solar hydrogen production activity”. In: *Angewandte Chemie* 129.43 (2017), pp. 13630–13634.

[152] Bangwang Li et al. “Exploring n-π^* Electronic Transitions in Graphitic Carbon Nitride: Fundamentals, Strategies, and Photocatalytic Advances”. In: *Chemistry–A European Journal* (2025), e202500297.

[153] Hongqi Zhu et al. “Construction of Azo-Linked Covalent Organic Frameworks via Monomer Exchange for Enhanced Photocatalytic Performance”. In: *ChemPhotoChem* 8.8 (2024), e202400013.

[154] Linghua Tan et al. “Synthesis of g-C3N4/CeO2 nanocomposites with improved catalytic activity on the thermal decomposition of ammonium perchlorate”. In: *Applied Surface Science* 356 (2015), pp. 447–453.

[155] Shaowen Cao et al. “Polymeric photocatalysts based on graphitic carbon nitride”. In: *Advanced Materials* 27.13 (2015), pp. 2150–2176.

[156] AP Dementjev et al. “X-Ray photoelectron spectroscopy reference data for identification of the C3N4 phase in carbon–nitrogen films”. In: *Diamond and related materials* 9.11 (2000), pp. 1904–1907.

[157] Joost VandeVondele and Jürg Hutter. “Gaussian basis sets for accurate calculations on molecular systems in gas and condensed phases”. In: *The Journal of chemical physics* 127.11 (2007).

[158] Sudhir K Sahoo et al. “Photocatalytic water splitting reaction catalyzed by ion-exchanged salts of potassium poly (heptazine imide) 2D materials”. In: *The Journal of Physical Chemistry C* 125.25 (2021), pp. 13749–13758.

[159] Hendrik Schlomberg et al. “Structural insights into poly (heptazine imides): a light-storing carbon nitride material for dark photocatalysis”. In: *Chemistry of Materials* 31.18 (2019), pp. 7478–7486.

[160] Julia Kröger et al. “Conductivity mechanism in ionic 2D carbon nitrides: from hydrated ion motion to enhanced photocatalysis”. In: *Advanced Materials* 34.7 (2022), p. 2107061.

[161] Johan Mahler and Ingmar Persson. “A study of the hydration of the alkali metal ions in aqueous solution”. In: *Inorganic chemistry* 51.1 (2012), pp. 425–438.

[162] Guohua Gao et al. “Advances in the production technology of hydrogen peroxide”. In: *Chinese Journal of Catalysis* 41.7 (2020), pp. 1039–1047.

[163] Xin-Quan Tan et al. “Point-to-face contact heterojunctions: interfacial design of 0D nanomaterials on 2D g-C3N4 towards photocatalytic energy applications”. In: *Carbon Energy* 4.5 (2022), pp. 665–730.

[164] Bradley D Frank et al. “Photocharging of carbon nitride thin films for controllable manipulation of droplet force gradient sensors”. In: *Journal of the American Chemical Society* 145.45 (2023), pp. 24476–24481.

[165] Sue-Faye Ng et al. “2D carbon nitrides: Regulating non-metal boron-doped C3N5 for elucidating the mechanism of wide pH range photocatalytic hydrogen evolution reaction”. In: *Chinese Journal of Catalysis* 47 (2023), pp. 150–160.

[166] Liquan Jing et al. “Engineering polyheptazine and polytriazine imides for photocatalysis”. In: *Angewandte Chemie* 136.49 (2024), e202406398.

[167] Sue-Faye Ng, Joel Jie Foo, and Wee-Jun Ong. “Isotype heterojunction: tuning the heptazine/triazine phase of crystalline nitrogen-rich C 3 N 5 towards multifunctional photocatalytic applications”. In: *Materials Horizons* 11.2 (2024), pp. 408–418.

[168] Junjiang Zhu et al. “Graphitic carbon nitride: synthesis, properties, and applications in catalysis”. In: *ACS applied materials & interfaces* 6.19 (2014), pp. 16449–16465.

[169] Marcus D Hanwell et al. “Avogadro: an advanced semantic chemical editor, visualization, and analysis platform”. In: *Journal of cheminformatics* 4 (2012), pp. 1–17.

[170] Bernardo de Souza. “GOAT: A Global Optimization Algorithm for Molecules and Atomic Clusters”. In: *Angewandte Chemie International Edition* (2025), e202500393.

[171] Frank Neese et al. “The ORCA quantum chemistry program package”. In: *The Journal of chemical physics* 152.22 (2020).

[172] Stefan Grimme et al. “r2SCAN-3c: A “Swiss army knife” composite electronic-structure method”. In: *The Journal of Chemical Physics* 154.6 (2021).

[173] Nidia Gabaldon Limas and Thomas A Manz. “Introducing DDEC6 atomic population analysis: part 2. Computed results for a wide range of periodic and nonperiodic materials”. In: *RSC advances* 6.51 (2016), pp. 45727–45747.

[174] Jun Xu, Wenhua Huang, and Richard L McCreery. “Isotope and surface preparation effects on alkaline dioxygen reduction at carbon electrodes”. In: *Journal of Electroanalytical Chemistry* 410.2 (1996), pp. 235–242.

[175] JR Tobias Johnsson Wass et al. “Quantum chemical modelling of the rate determining step for oxygen reduction on quinones”. In: *Physical Chemistry Chemical Physics* 8.36 (2006), pp. 4189–4199.

[176] Irene Lamata-Bermejo et al. “Understanding the Wettability of C1N1 (Sub) Nanopores: Implications for Porous Carbonaceous Electrodes”. In: *Angewandte Chemie* (2024), e202411493.

[177] Conchi O Ania et al. “Engaging nanoporous carbons in “beyond adsorption” applications: Characterization, challenges and performance”. In: *Carbon* 164 (2020), pp. 69–84.

[178] Markus Antonietti and Martin Oschatz. “The concept of “noble, heteroatom-doped carbons,” their directed synthesis by electronic band control of carbonization, and applications in catalysis and energy materials”. In: *Advanced Materials* 30.21 (2018), p. 1706836.

[179] Christian Weinberger et al. “The structure of water in silica mesopores–Influence of the pore wall polarity”. In: *Advanced Materials Interfaces* 9.20 (2022), p. 2200245.

[180] Thomas D Kühne et al. “Efficient and accurate Car-Parrinello-like approach to Born-Oppenheimer molecular dynamics”. In: *Physical review letters* 98.6 (2007), p. 066401.

[181] Stefan Grimme, Christoph Bannwarth, and Philip Shushkov. “A robust and accurate tight-binding quantum chemical method for structures, vibrational frequencies, and noncovalent interactions of large molecular systems parametrized for all spd-block elements (Z= 1–86)”. In: *Journal of chemical theory and computation* 13.5 (2017), pp. 1989–2009.

[182] Stefan Goedecker, Michael Teter, and Jürg Hutter. “Separable dual-space Gaussian pseudopotentials”. In: *Physical Review B* 54.3 (1996), p. 1703.

[183] Eva Perlt et al. “Finding the best density functional approximation to describe interaction energies and structures of ionic liquids in molecular dynamics studies”. In: *The Journal of Chemical Physics* 148.19 (2018).

[184] Hossam Elgabarty, Rustam Z Khaliullin, and Thomas D Kühne. “Covalency of hydrogen bonds in liquid water can be probed by proton nuclear magnetic resonance experiments”. In: *Nature communications* 6.1 (2015), p. 8318.

[185] Rustam Z Khaliullin and Thomas D Kühne. “Microscopic properties of liquid water from combined ab initio molecular dynamics and energy decomposition studies”. In: *Physical Chemistry Chemical Physics* 15.38 (2013), pp. 15746–15766.

[186] Gerald Lippert, Jürg Hutter, and Michele Parrinello. “The Gaussian and augmented-plane-wave density functional method for ab initio molecular dynamics simulations”. In: *Theoretical Chemistry Accounts* 103 (1999), pp. 124–140.

[187] Valery Weber et al. “Magnetic linear response properties calculations with the Gaussian and augmented-plane-wave method”. In: *The Journal of chemical physics* 131.1 (2009).

[188] Frank Jensen. “Segmented contracted basis sets optimized for nuclear magnetic shielding”. In: *Journal of Chemical Theory and Computation* 11.1 (2015), pp. 132–138.

[189] Todd A Keith and Richard FW Bader. “Calculation of magnetic response properties using a continuous set of gauge transformations”. In: *Chemical physics letters* 210.1-3 (1993), pp. 223–231.

[190] TA Keith and RFW Bader. “Calculation of magnetic response properties using atoms in molecules”. In: *Chemical physics letters* 194.1-2 (1992), pp. 1–8.

[191] Graeme Henkelman, Blas P Uberuaga, and Hannes Jónsson. “A climbing image nudged elastic band method for finding saddle points and minimum energy paths”. In: *The Journal of chemical physics* 113.22 (2000), pp. 9901–9904.

[192] Gion Calzaferri et al. “Multiple equilibria description of type H1 hysteresis in gas sorption isotherms of mesoporous materials”. In: *Materials Chemistry and Physics* 296 (2023), p. 127121.

10. Appendices

A. Supplementary Information for "Kinetically stable and highly ordered two-dimensional CN2 crystal structures"

A.1. Saddle points and barrier heights

Here we present our investigation on transition mechanisms and energies associated to form CN_2 materials using density functional theory as well as machine learning (ML) potential. An extensive search for saddle points of the ML potential energy surface (PES) for all structures included and excluded (kinetically unstable) in our study, in particular, validating them at the level of DFT is beyond the scope of contemporary work. Therefore, we selected the most stable structure, namely S1, and also one among the kinetically unstable structures, in the following referred to as the U structure. To reveal possible mechanisms in which a N_2 molecule is released, we utilized the hopping approach as used in the minima hopping method, i.e. short MD runs followed by local geometry optimizations. For each of the two structures, we performed 1000 hops using the ML potential and starting from the same structure and the same kinetic energy but each with a different set of initial velocities. The ML potential in this study is based on the standard high-dimensional artificial neural network (ANN) method [97]. For the U structure, about 20% of the hops succeeded in escaping the initial minimum. In the case of the S1 structure, only a handful of hops were successful. By doubling the kinetic energy, a sizable fraction of hops, i.e. about 10%, advanced to a different minimum. This preliminary result is a clear indication that the basin of S1 is surrounded by higher barriers within the ML potential, in agreement with our previous MD

simulations. We performed the hopping runs with the supercells used originally for the MD simulations, with S1 and U structures containing 1440 and 1080 atoms, respectively. To reduce the computational burden in the validation step with DFT, we repeated the sampling with smaller supercells where S1 and U structures contain 216 and 240 atoms, respectively. These calculations illustrated similar mechanisms to release N_2 where a ring opening of a pentagon as a whole unit or a segment of a nitrogen rich moiety occurs. Some reversible and insignificant processes, such as flipping five-membered rings or bond switching between two connected moieties unfold as well. However, we focused on the aforementioned ring opening process and calculated the activation energies and minimum energy pathways (MEPs) using the climbing-image nudged-elastic bands method [191]. Figs. 10.1 and 10.2 depict DFT and ANN energies of S1 and U structures along the MEP as a function of the pathway parameter. The DFT barrier heights for S1 and U structures are 1.79 eV and 0.75 eV, respectively. The barrier heights of the ML potential are 1.79 eV and 0.66 eV for S1 and U, respectively, in reasonable agreement with those of DFT. This Situation is probably not the case for every transition state on the PES of the CN_2. It can be deduced from the reverse processes shown in Figs. 10.1 and 10.2, as a consequence of poor agreement in energy differences of the start and end minima between ML and DFT. This is due to the fact that ring opening and/or the formation of the N_2 molecule do not result in exactly the same sort of distortion of atoms, thereby bond length and bond angles of the end structures in DFT and the ML potential differ more than the start counterparts. This fact is not a major concern, whilst different exchange-correlation (XC) functionals in DFT may result disagreeing energy differences of minima and barrier heights to the extent PBE XC and the ML potential differ. Based on the harmonic transition state theory and assuming a typical attempt frequency of 10^{13} Hz, a barrier height of about 0.66 eV can be surmounted approximately in a relaxation time of less than 1 ns at a temperature of 600°C. The remarkable stability of S1 in our MD simulations is also supported by the large barrier height of 1.79 eV that makes it considerably more thermally stable than the U structure. We carried out the DFT calculations using the same code and parameters as described in detail in the manuscript.

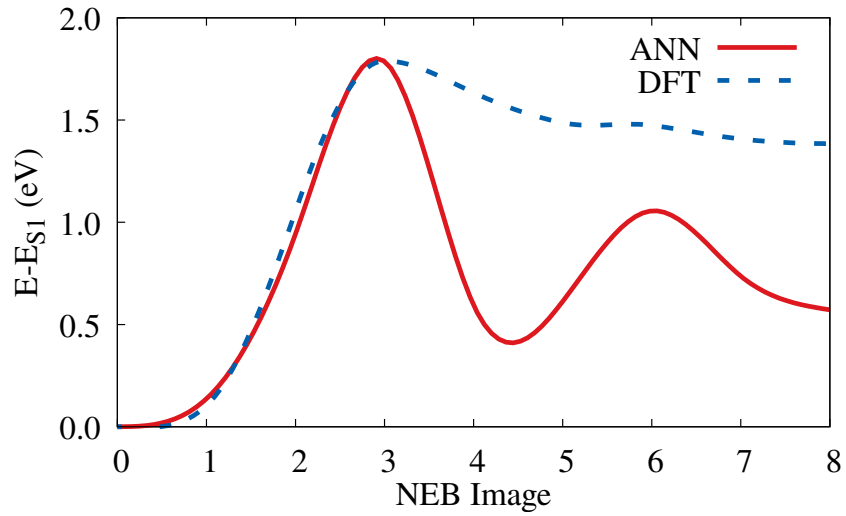

Figure 10.1.: Energy along the minimum energy pathway of ring opening for structure S1.

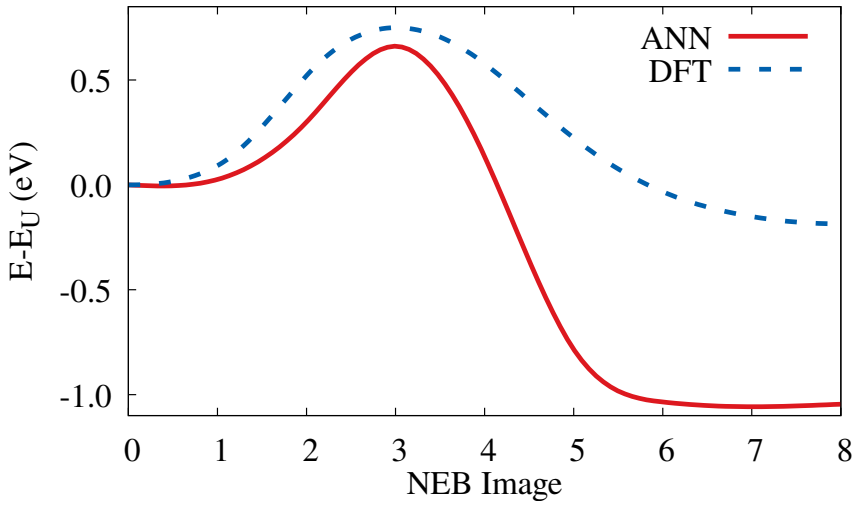

Figure 10.2.: Energy along the minimum energy pathway of ring opening for structure U.

A.2. Illustration of Structure S3

Figure 10.3 shows the structure S3 translated in a direction to have a different vision of the hole.

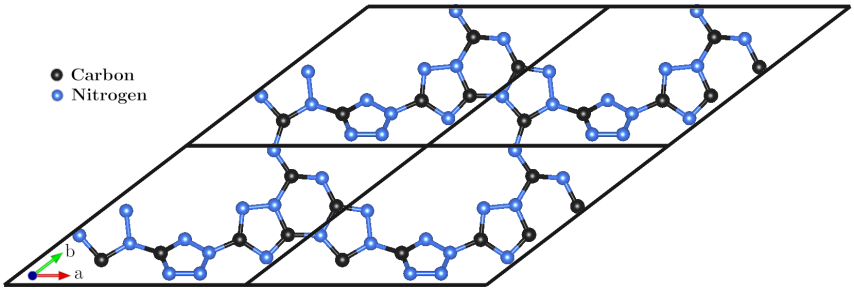

Figure 10.3.: Structure S3, also illustrated in Figure 1c in the paper. In this view it is translated to have the hole at the center.

A.3. Convergence Test

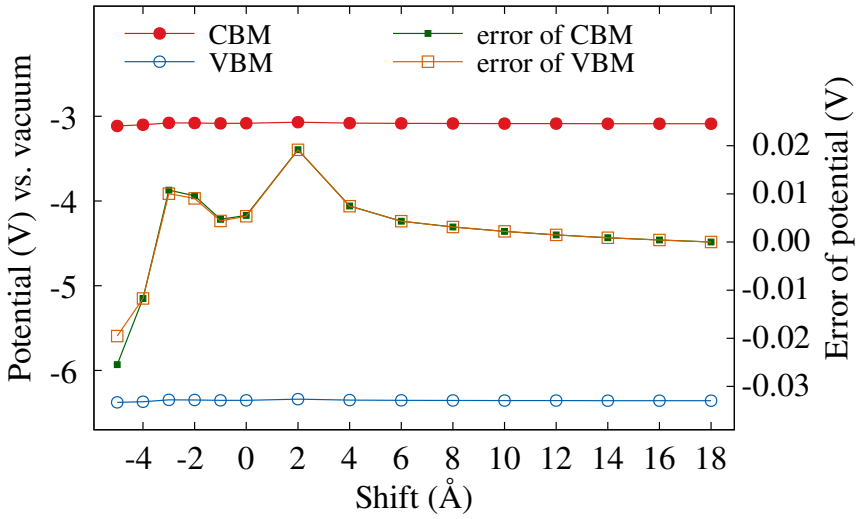

Figure 10.4.: Convergence test for the two distant monolayers, one of which is inverted. The band edges versus the vacuum level as a function of shift which is the change to both the interlayer distance and the vacuum size on each side applied to the value (9 Å) used for the calculations presented in the manuscript. This sums up to a total distance of 27 Å between the two layers and a vacuum size of 54 Å for the largest shift value of 18 Å. The errors of the CBM and VBM potentials are estimated by using the values at the largest distance as the reference values for CBM and VBM, respectively.

A.4. Coordinates in VASP format

S1

```
 C N
   1.00000000000000
     5.4786971044732740   -0.4391941048171640   -0.1643094229339890
     2.2917097016565213    5.0625780050075440   -0.3465421802645595
     1.9677390588847445    0.7312377997295123    6.8527916874296242
   C    N
     6    12
Direct
  0.6657817755064596  0.0639989385977521  0.2370936492221689
  0.0726159169654708  0.7703259354902119  0.1764799766012214
  0.4925501235469778  0.4664659708255902  0.1074710114450599
  0.9642882936339646  0.2207984657387838  0.0008762669706564
  0.0708817598883194  0.4948996185717789  0.8036501651164727
  0.4649719519038787  0.7952935371001126  0.4803150850213164
  0.9251568745241929  0.6577480955406318  0.3102474367544777
  0.8134047484664200  0.6102235271170388  0.8604582715808569
  0.0723284281825698  0.8932270813804387  0.6419936814595041
  0.4611730148898517  0.2698812571754090  0.2317204474143878
  0.6783593580277122  0.8393299925812826  0.3478669079039357
  0.7451969626836389  0.4308286570742620  0.9891480047591831
  0.2343678795914520  0.9908507075655948  0.5194574908323192
  0.9189146229071551  0.0232600692095019  0.1293841363517572
  0.2074849665104674  0.6429839531483820  0.6735460975800628
  0.3225910121622564  0.6924146979162691  0.0818881654785831
  0.1774522616469372  0.2559653237465043  0.8844739127194020
  0.4569100319622931  0.5715641382204375  0.5745693057886907
```

S2

```
 C N
   1.00000000000000
     4.4505156038310751   -0.2279798799585199    0.1027501585463659
     0.1837082391629621    4.7464676919228408    0.0676906844120936
     0.6841608761148262    0.3517439543606521    7.8680780640068120
   C    N
     5    10
Direct
  0.5532982244375404  0.0780122238337313  0.4824898011008827
  0.8086759416757658  0.4980467194877605  0.8558512847501731
  0.1792589668843902  0.3018796962450452  0.6507048590238327
  0.8753952311655624  0.6720405879544842  0.5884709726764825
  0.8520816271341971  0.2263789570480697  0.0655953585850142
  0.7818071873552555  0.1089235437045701  0.2343171496552685
  0.6940799355674656  0.4515873807454014  0.0175502372285479
  0.0311378587794735  0.3018774642355879  0.8162011895958088
  0.3852551633031638  0.1063010740546346  0.6279005822308079
  0.5577754143097522  0.2237175397197930  0.3311782895426347
  0.7278295831407675  0.6910578903745588  0.7403314705601289
  0.0607543370768440  0.1223688935153575  0.9535223269228652
  0.7829956663566122  0.8743974979391638  0.4625372462501716
  0.9244013641856554  0.8999378131810971  0.3043173458550257
  0.0914835356275887  0.4952127309607306  0.5352320060224116
```

S3

```
 C N
   1.00000000000000
     5.2030211749019202    0.0275179860685105   -0.1238217776475818
    -1.7789629651693180    5.3403240961877669    0.2541572969061232
    -1.5933306335158341   -0.5680716768973578    7.4455427324563566
   C    N
     6    12
Direct
  0.0500432850628343  0.5630779287590784  0.2711576543405556
  0.1307394676412557  0.3384929945802568  0.0413170148090742
  0.5938463094175361  0.7099736589526273  0.8144678042030691
  0.8547690461092898  0.6101559033028323  0.4670283422345278
  0.4139313393214934  0.7422498116240135  0.0910541773561491
  0.7575710692811484  0.1349944132830032  0.1599873275822929
  0.9290465354489754  0.1289741141510277  0.0590980097212466
  0.7372799771629062  0.9335789744280163  0.6045367312471228
  0.8236172887509952  0.3548625549068092  0.2689393530884772
  0.0766629295101993  0.7297043988883658  0.3961463764133839
  0.6918983090710071  0.3876686754652710  0.3954554623141107
  0.4513673554231374  0.6189314339777923  0.9496891053165086
  0.5284286833001701  0.9585062145941592  0.1771921556118414
  0.1987415062282025  0.5604816413283871  0.1446995393521675
  0.7883153354918235  0.7104413228266111  0.6103164907317336
  0.6998813516032811  0.5647443011579654  0.7402200947432931
  0.6118444712722209  0.9326902460713526  0.7335329050850348
  0.2836257779035378  0.3711613587024161  0.9221115398493609
```

ABT*

```
 C N
   1.00000000000000
    10.3399337983475199   -0.2058744998882732   -1.8388230416326647
    -5.2977209476750469    9.0368660280528985   -0.9935135308938964
    -0.7013317160506479   -0.9126608967995442    3.9404810955777179
   C    N
     6    12
Direct
  0.7839590381690631  0.0435501233121002  0.0452842163924352
  0.9948554863370591  0.0603668454201485  0.9900058413290731
  0.3760725422964336  0.8581930080826757  0.9512533884961941
  0.1819870694663486  0.6357320214089991  0.9560536303536944
  0.1651753003894666  0.8413770196981701  0.0065288345329100
  0.9780536682318307  0.2660177816215291  0.0405234970404697
  0.0471429660043757  0.4299332359912288  0.0980755306180438
  0.8349272781202585  0.1890956157282659  0.0552649438420533
  0.8602513399475616  0.9738663361400983  0.0292807588640468
  0.0612424284733517  0.2074221660849751  0.9938379726990696
  0.0851273958989400  0.9100964978336701  0.0866649239786089
  0.2997748029447173  0.9278722131256716  0.9672358646950967
  0.1129008688887054  0.4718198442323128  0.8985173102973187
  0.3251120999641679  0.7126540356513515  0.9413089212199302
  0.6434826681366457  0.9570042124852489  0.1021652558702596
  0.5165511612768935  0.9447410334219529  0.8943670785735657
  0.0749010842151774  0.9916462003141656  0.9098635814605853
  0.0987976308267309  0.6943279724206144  0.0027228053914254
```

B. Supplementary Information for "Towards CN_2: Novel Carbon Nitride Materials with Ultra-high Nitrogen Content of ABT-CN2"

B.1. Additional images of ABT and H-ABT crystals

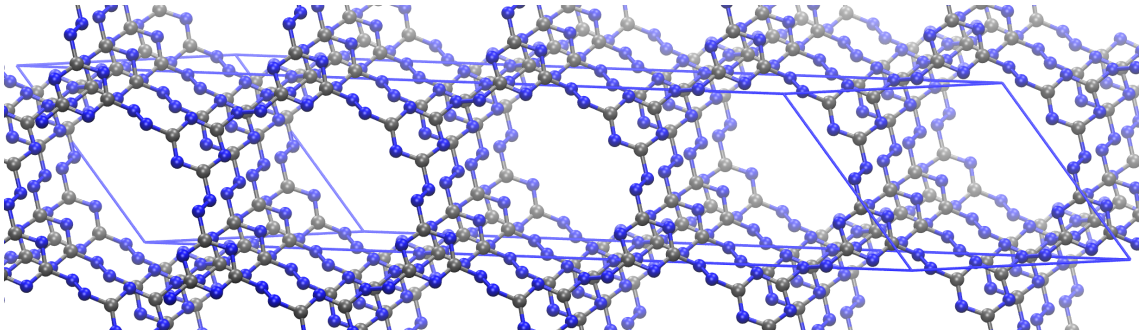

(a) ABT from top view.

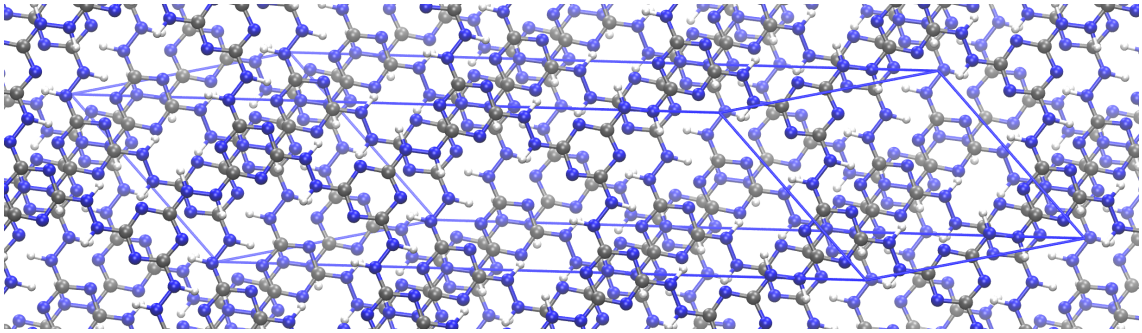

(b) H-ABT from top view.

Figure 10.5.: Top view of ABT and H-ABT with cell boundaries.

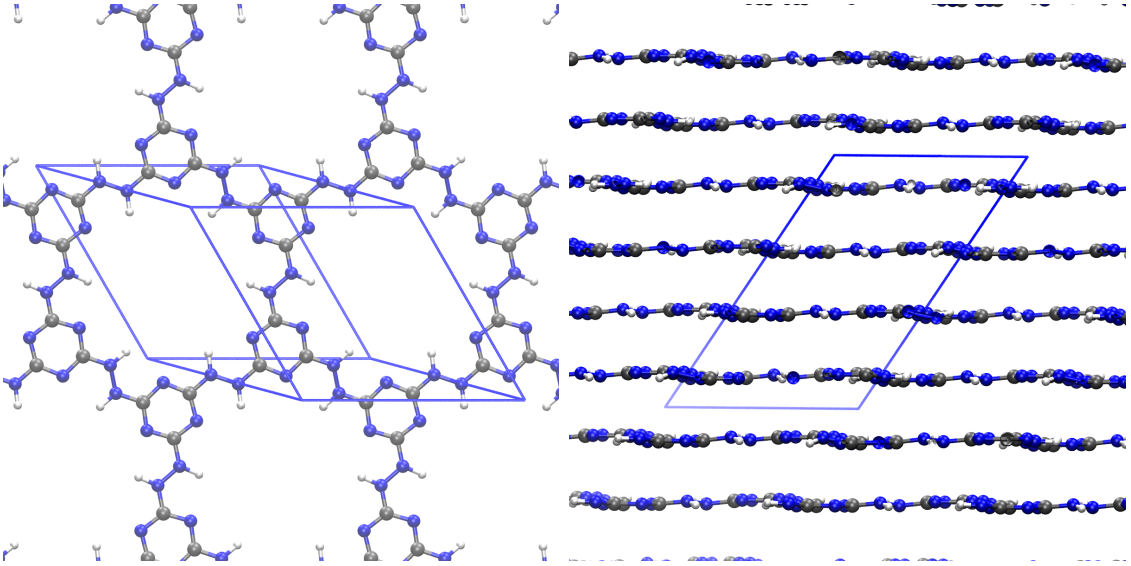

(a) H-ABT singlelayer from top view.

(b) H-ABT from side view.

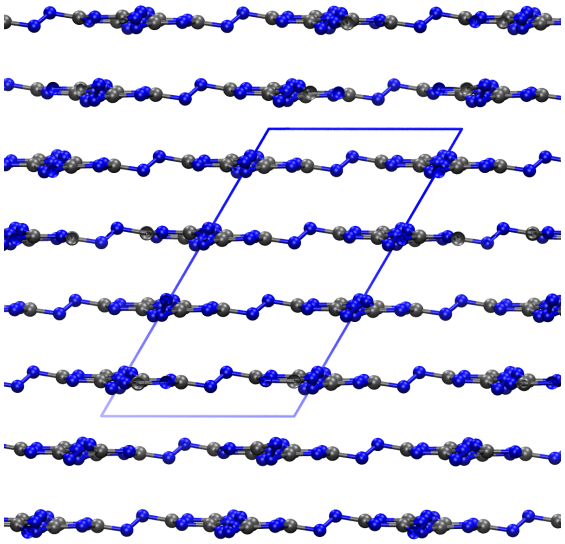

(c) ABT from side view.

Figure 10.6.: Top view of a singlelayer of H-ABT, and side view of both structures. H-ABT is flat, while ABT is buckled.

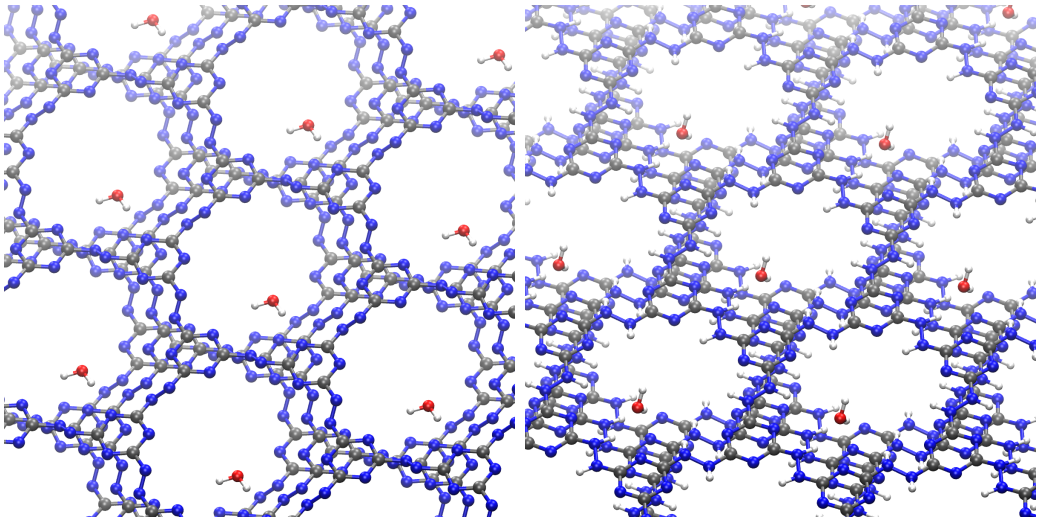

(a) ABT (b) H-ABT

Figure 10.7.: Water molecules adsorbed on the two systems, adsorption orientation is contrary for maximized hydrogen bonds

B.2. Bandgaps

Bandgap estimates were taken from UV-VIS measurements conducted with a Perkin Elmer Lambda 650 spectrometer. Bandgaps were extrapolated from tauc plots as shown below. Here, a direct and indirect bandgap analysis of SM-360-yellow is performed. The bandgaps of other samples were identically recovered.

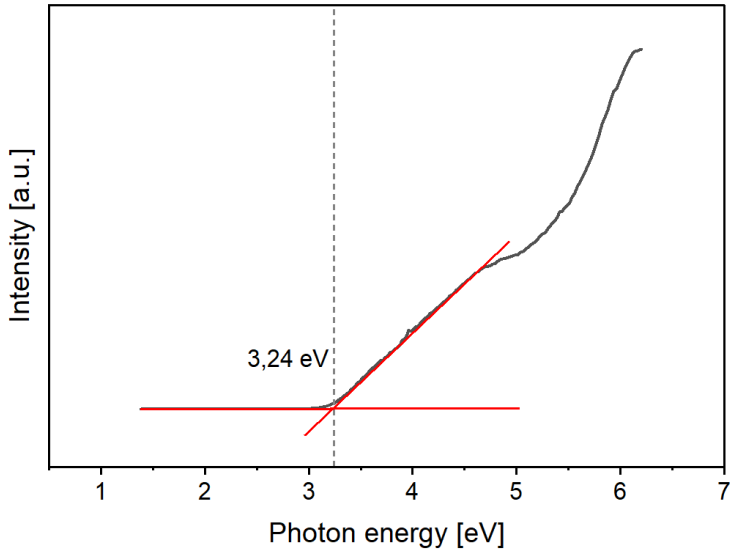

Figure 10.8.: Tauc plot of SM-360-yellow to estimate direct bandgap.

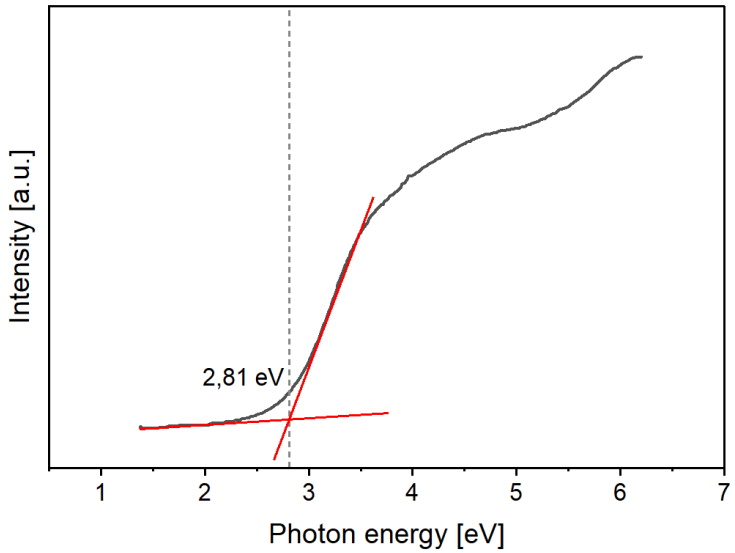

Figure 10.9.: Tauc plot of SM-360-yellow to estimate indirect bandgap.

B.3. Photocatalytic Experiments

B.3.1. Benzylamine oxidation to N-Benzylidenebenzylamine

Benzylamine oxidation is employed as a reaction to benchmark photocatalytic activity, effectively operating without the necessity of water as a solvent. This reaction was conducted to evaluate whether the interaction with water and the generation of hydroxy groups during H_2O_2 photosynthesis are diminishing the reactivity of other photocatalytic materials, which could account for the relatively low activity observed in the experiments. However, with the exception of the reference material bulk-CN, only ACN-75 demonstrated photocatalytic activity, successfully facilitating the oxidation of benzylamine to benzylidenebenzylamine. Consequently, the photocatalytic activity of the SM-360 samples is inherently limited. Based on the primary differences identified in our study, the lower surface area of SM-360 samples, in comparison to ACN-75, likely constitutes the most significant limitation, which could be improved through exfoliation techniques.

Reaction time	Yield [%]	Conversion [%]
12h (bulk-CN)	12	42
24h (bulk-CN)	17	46
48h (bulk-CN)	26	91
12h (ACN-75)	2	6
24h (ACN-75)	2	6
48h (ACN-75)	3	9
12h (SM-360-yellow)	0	0
24h (SM-360-yellow)	0	0
48h (SM-360-yellow)	0	0
12h (SM-360-violet)	0	0
24h (SM-360-violet)	0	0
48h (SM-360-violet)	0	0

Table 10.1.: Yields and conversions after reaction time.

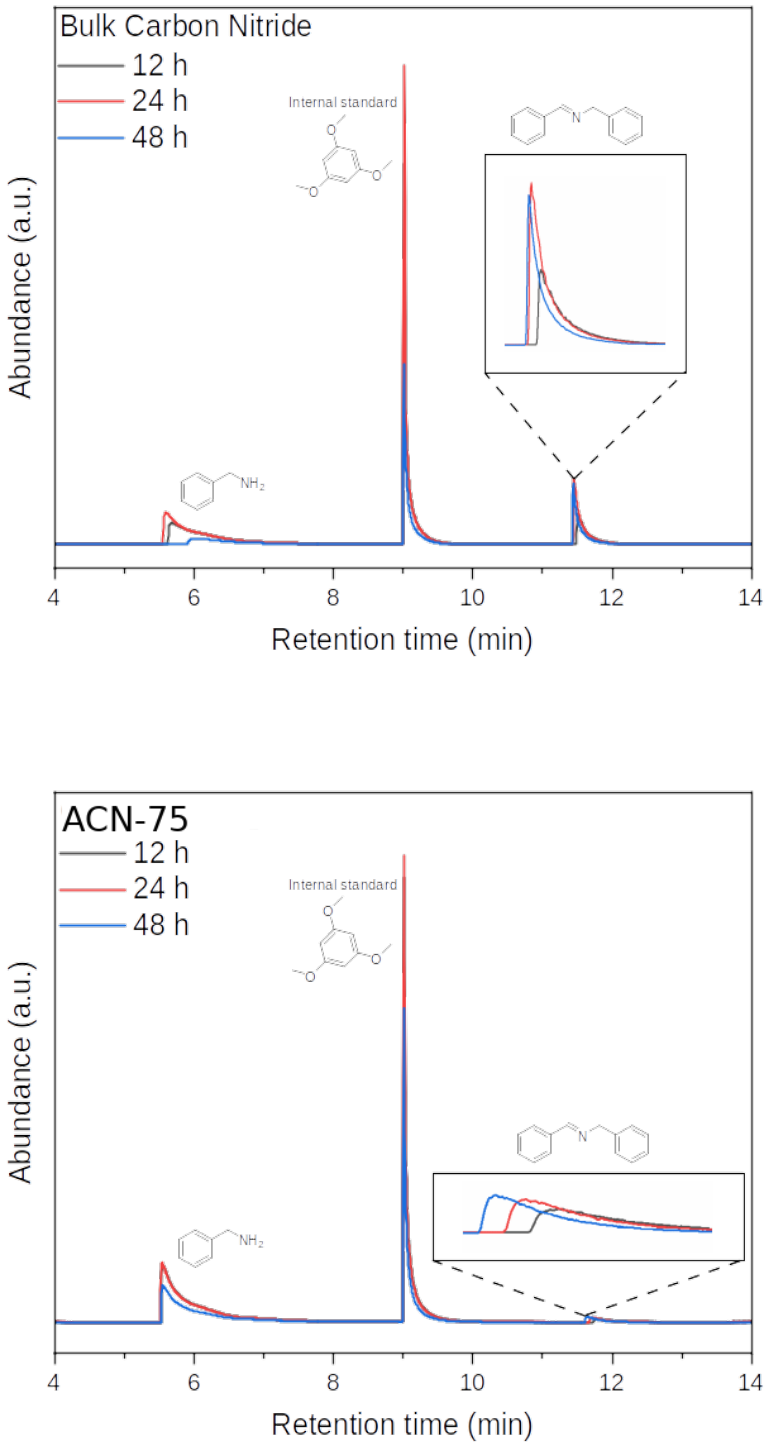

Figure 10.10.: HPLC measurements for bulk-CN and ACN-75.

B.4. XPS & XRD

The surface elemental composition and chemical constitution of the samples were studied using X-ray photoelectron spectroscopy (XPS) with K-α and monochromatic X-ray radiation of -10 to 1350 eV (Thermo Fisher Scientific, USA). The samples were dispersed in ethanol and deposited on a silica wafer by drop casting. Survey scans show dominant nitrogen and carbon peaks around 400 eV and 286 eV. The oxygen 1s signal can be found around 531 eV, scaling with the Si 2s and 2p signals around 150 eV and 99 eV, and is a typical background signal from silica wafers. Minor signals of Cl can be observed at 198 eV (Cl 2p) and 1304 (Cl LMM), being impurities originating from the tri-chloro-triazine used for synthesis. Traces of sodium 1s are around 1071 eV and 496 eV (Na KLL), stemming from sodium hydroxide used with SM-360-violet and are only visible in this material. Furthermore, this sample also has a signal at 305 eV, assigned to Mg KLL, potentially coming from impurities of the sodium hydroxide used.

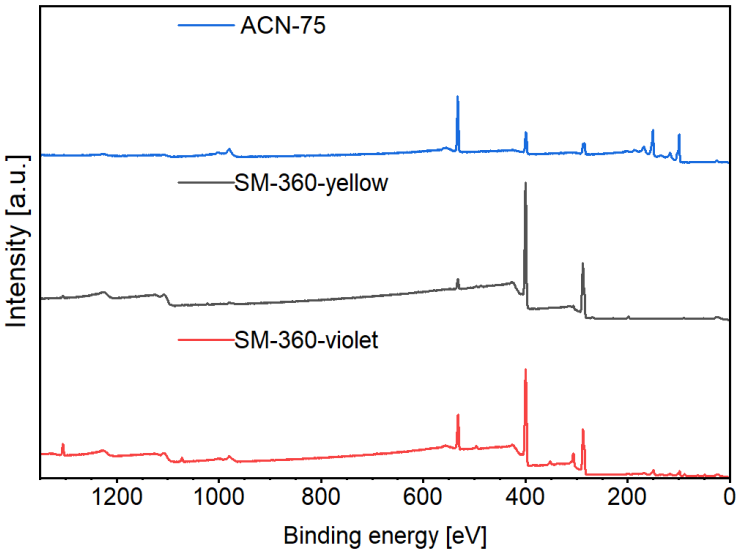

Figure 10.11.: Comparative XPS survey spectra.

Powder X-ray diffraction measurements were conducted on a Bruker D8 Discover instrument, using Cu-K radiation with a wavelength of 1.5418 Å.

B.5. TGA

Thermogravimetric analysis (TGA) was performed using a TGA PT1000 thermobalance from Linseis. The sample was placed in a 0.2 mL corundum crucible. Measurements were performed under a constant Argon gas (purity 5.0 from Wöhning Gas) flow of 150 mL min^{-1} in a temperature range from 30 °C to 800 °C using a heating rate of 10 °C min^{-1}. For mass spectrometry, the instrument was coupled with a Pfeiffer Vacuum Omnistar mass spectrometer. The values given in the plots are in m/z. Intensities are arbitrary; each line is plotted with individual y-axis, which is omitted for better clarity. An analysis of the figures can be found in the main paper.

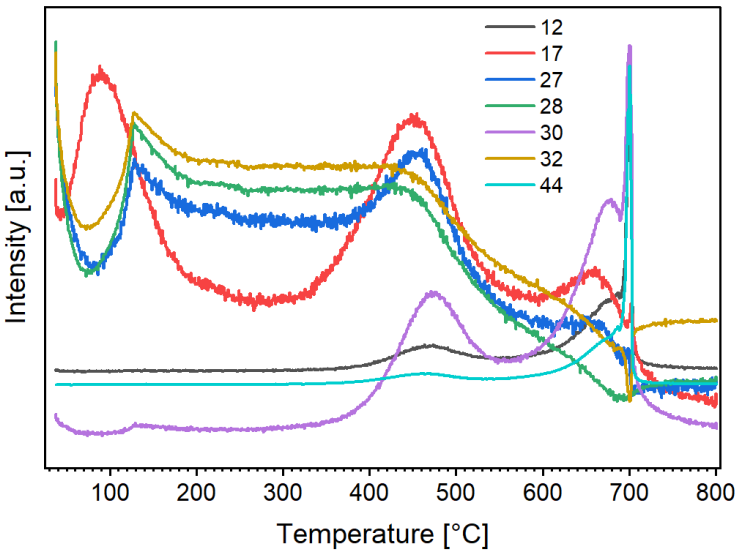

Figure 10.12.: MS analysis of SM-360-yellow.

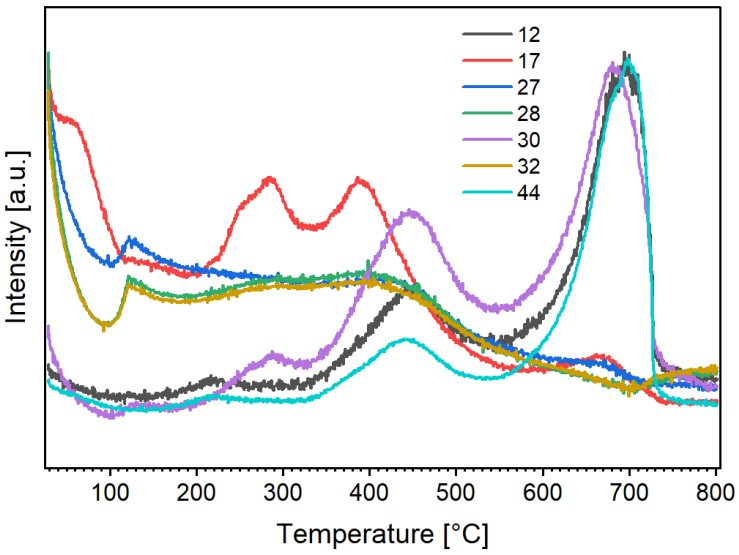

Figure 10.13.: MS analysis of ACN-75.

B.6. Surface area

Prior to all physisorption experiments, samples were degassed under vacuum at 250 °C for 16 h. N_2 (at 77 K) sorption measurements were performed on a Quantachrome Autosorb iQ instrument. The specific surface areas were calculated using the Brunauer–Emmett–Teller (BET) method applied to nitrogen adsorption data ($p/p_0 < 0.3$) with the Rouquerol criteria. Since both samples prepared with salt melts share many characteristics, we expect them to have mostly identical surface areas and measured only SM-360-yellow. The surface areas are $\approx 38 \frac{m^2}{g}$ for ACN-75, and $\approx 8 \frac{m^2}{g}$ for SM-360-yellow. Both are quite low, but are comparable to those of other carbon nitride materials. ACN-75 clearly exhibits an adsorption/desorption hysteresis, indicating mesoporous cavities in the material [192].

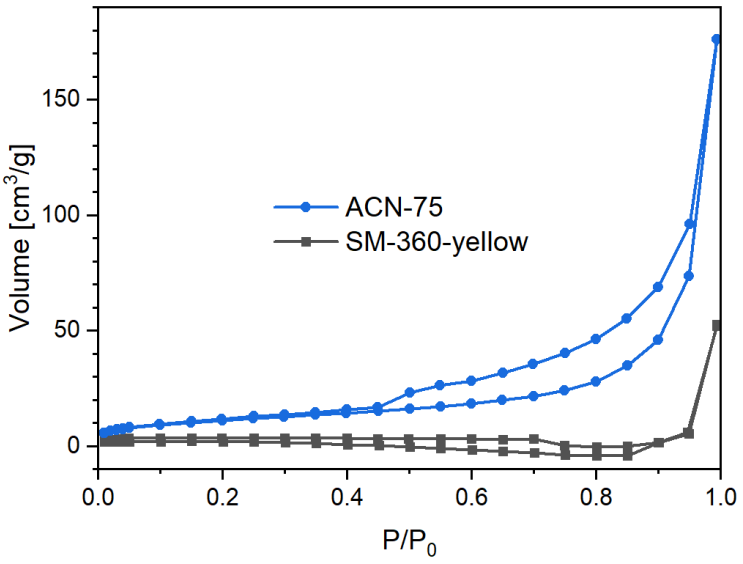

Figure 10.14.: Isotherms fo ACN-75 and SM-360-yellow.

B.7. Electrochemical measurements

B.7.1. Mott-Schottky

Mott-Schottky measurements were used to estimate the conduction band edge from the flat-band potential. For this, each sample was dispersed in solution with ethanol and PVDF as binder, drop casted on an area of 0.5 cm^2 of ITO, and slowly dried on a heating plate. Measurements were conducted in a three-elecrode cell with 0.1 M Na_2SO_4 aqueous electrolyte and Ag/AgCl reference electrode. Measured with an MPG2 multichannel potentiostat from BioLogic at a frequency of 10 kHz, ranging from -1.5V to 1.5V, with data points from 0.5V to 1.5V extrapolated to get the flatband potential. This value was then corrected to RHE. Blank ITO taken as reference.

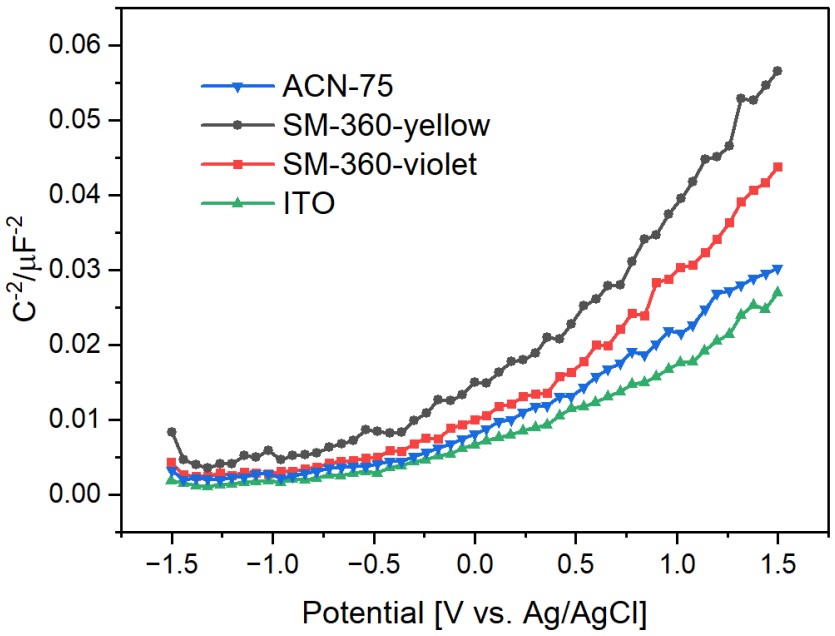

Figure 10.15.: Mott-Schottky plots.

B.7.2. Cyclovoltammetry

Electrochemical measurements were recorded on an MPG2 multichannel potentiostat from BioLogic. All the electrochemical measurements were performed in a Swagelok-type cell with stainless steel bars as current collectors. The cells were assembled by positioning one carbon electrode confronting a Zn-foil, separated by a glass microfiber filter (Whatman GF/B) previously soaked in the electrolyte (1M Zn_2SO_4 solution). Carbon electrodes were prepared with an ink consisting of a 6:2:2 mixture of sample, carbon black, and Aquivion binder. The ink was dropped on a 1 cm^2 area of carbon paper and dried at 60 °C overnight in a vacuum oven. The measurements were repeated five times; each fourth cycle is plotted below. All measurements were performed at room temperature and ambient pressure.

In the Nyquist plots, ACN-75 exhibits a much higher impedance compared to the other samples, as seen from the steeply inclined curve. This indicates a significantly larger charge transfer and diffusion resistance, which can be attributed to its smaller, less-condensed particles and reduced aromatic conjugation, both of which hinder efficient charge transport.

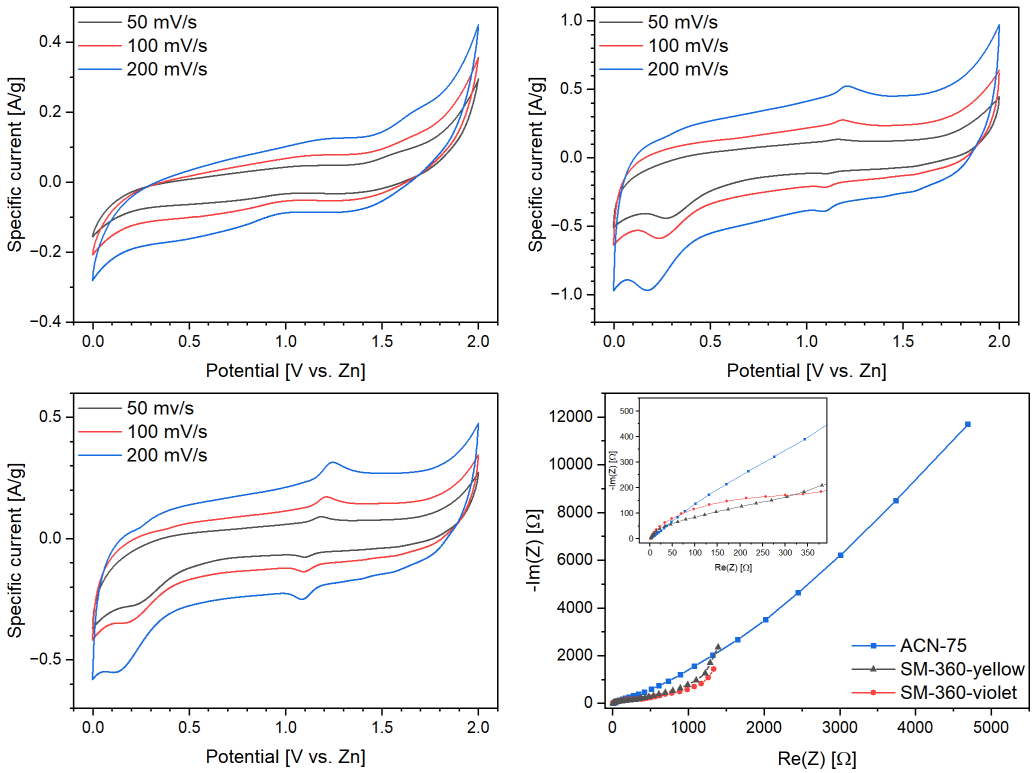

Figure 10.16.: Electrochemical measurements showing CV measurements of ACN-75 (top left), SM-360-violet (top right), SM-360-yellow (bottom left) and a comparison of their nyquist plots (bottom right).

List of Figures

List of Tables